NTNU

Norwegian University of
Science and Technology

Simulation and fabrication of two-dimensional photonic crystal drop filters for biosensing

Ingerid Gjeitnes Hellen

Nanotechnology
Submission date: June 2018
Supervisor: Astrid Aksnes, IES
Co-supervisor: Jens Høvik, IES

Norwegian University of Science and Technology
Department of Electronic Systems

Problem description

Photonic crystals (PhC) are periodic structures of varying dielectric constants capable of manipulating light depending upon its frequency and wave vector. By making the photonic crystal periodic in only one or two dimensions it can easily be incorporated into integrated photonics, which allows for a large amount of optical devices to be fabricated on a single chip.

The goal of this master thesis is to design and fabricate a two-dimensional photonic crystal drop filter for use as an optical biosensor. The sensor will be part of an integrated circuit implemented on a silicon-on-insulator system, which allows for existing CMOS techniques to be harnessed during the fabrication. The thesis is a continuation of both my project thesis and previous work by our research group, and employs both simulations and fabrications to reach the final goal.

The design optimizations will be performed using both eigenmode computations with MIT Photonic Bands (MPB) and finite-difference time-domain simulations with MIT Electromagnetic Equation Propagation (Meep). While 3D simulations give the most accurate results, more time efficient 2D simulations will sometimes be used to observe a trend or to prove a concept. The simulations will also be used to investigate the biosensing capabilities of the drop filter.

The 3D simulation results will be validated by comparing their results with physical filter performance. The drop filter will be fabricated in the NTNU NanoLab cleanroom using a series of nanofabrication instruments such as plasma-enhanced chemical vapor deposition (PECVD), electron-beam lithography (EBL) and inductively coupled plasma reactive ion etching (ICP-RIE). Characterization will be performed both by imaging using scanning electron microscopy (SEM) and by coupling light through the integrated circuit and observing the output signal.

Abstract

The main goal of this master thesis was to design and fabricate a biosensor consisting of a 2D photonic crystal. Its periodicity was made by etching a hexagonal hole pattern in a silicon slab, and a few linear defects were added by removing some of the holes. The result was a drop filter consisting of two waveguides with a resonator between them, all of which were positioned on top of a layer of silicon oxide. The idea was that light would couple, or "drop", from one waveguide to the other if, and only if, it belonged to a resonance frequency, hence the name of the filter. However, the exact resonance frequencies would depend upon the refractive index of the surrounding media, making the filter able to sense its surroundings.

To reach that goal, several issues had to be addressed regarding the fabrication method, including silicon growth and etch times, increases in the hole radius relative to the exposure mask and resist cracking. In addition, an estimate of the refractive index $n_{\mathrm{Si}} \approx 3.37$ for the amorphous silicon slab was found using a combination of simulations and fabrications.

Simulation tools were also used both to optimize the silicon slab thickness, which was the only major parameter that had not been optimized during the project thesis, and to measure the biosensing abilities of the device. In addition, they were used to test the possibility of combining two drop filters along one waveguide, called multiplexing.

The results from the work mentioned above were used to fabricate a set of functioning drop filters. They resonated nicely, creating a high-intensity peak on the transmission graphs for the dropped light. Finally, the biosensing abilities of the drop filters were tested by changing the surrounding medium from air to purified water both inside the photonic crystal holes and above the crystal. It resulted in a resonance shift of approximately 25 nm, which corresponded to a normalized frequency shift of 4.3×10^{-3}. The goal of the project can therefore be considered as reached.

Sammendrag

Det overordnede målet med masteroppgaven var å designe og fabrikere en biosensor bygd opp av en fotonisk krystall. Slike krystaller består av periodisk varierende materialer med forskjellige optiske egenskaper, noe som gir dem en unik evne til å kontrollere lysbølger avhengig av frekvensen og bølgevektoren deres. I dette tilfellet var krystallen todimensjonal, og besto av en silisiumfilm som var plassert oppå et tykkere lag med silisiumoksid. Gjennom førstnevnte var det etset et heksagonalt mønster av sirkulære hull, og tre lineære krystalldefekter var lagd ved å fjerne noen av disse hullene. Resultatet var et fallfilter bestående av to bølgeledere og en resonator midt imellom dem. Filteret fungerte ved at kun lys som tilhørte en resonansfrekvens kunne tunnelere, eller "falle", fra en bølgeleder til den andre via resonatoren. Resonansfrekvensene var avhengig av brytningsindeksen til materialet inni hullene og oppå krystallen, noe som gjorde filteret i stand til å måle sine omgivelser.

For å nå det overordnede målet måtte først flere aspekter ved fabrikasjonsmetoden bli tatt hånd om. Dette inkluderer blant annet vekst- og etsetidene for silisium, forskjellen i hullradius mellom masken og det endelig resultatet, og sprekker i resisten. I tillegg ble en kombinasjon av simuleringer og fabrikasjon brukt til å estimere en brytningsindeks på ca. 3.37 for den amorfe silisiumfilmen.

Simuleringsverktøy ble også brukt til å optimalisere den eneste essensielle parameteren som ikke alt hadde blitt optimalisert i prosjektoppgaven, nemlig tykkelsen på silisiumfilmen. De ble også benyttet til å finne et estimat for filterets sensitivitet mot endringer i brytningsindeksen til omgivelsene. Til slutt ble de brukt til å teste muligheten for multipleksing, dvs. å koble sammen to eller flere filtere langs én og samme bølgeleder.

Resultatene fra arbeidet over ble til slutt brukt til å fabrikere et sett av fallfiltere, og flere av disse resonerte kraftig. Sensitiviteten til filtrene ble deretter testet ved å bytte ut luften inni hullene og oppå krystallene med vann. Dette resulterte i et resonansskift på ca. 25 nm, noe som tilsvarer 4.3×10^{-3} i normaliserte frekvensenheter. Man kan derfor fastslå at målet med oppgaven ble oppnådd.

Preface

This thesis is submitted as part of the requirements for the degree of Master of Science in Nanotechnology at the Department of Electronic Systems at the Norwegian University of Science and Technology (NTNU) in Trondheim.

The work is a continuation of a 15 ECTS specialization project completed in the fall of 2017 [1]. The project focused on optimizing the photonic crystal drop filter design using simulations, and its results will be heavily cited throughout this thesis. Initial aid with the fabrication methods was found in earlier works by our research group [2–5]. However, all results presented in this project are entirely the work of the author.

Acknowledgments

First and foremost I would like to thank my supervisor, Astrid Aksnes, and my co-supervisor, Jens Høvik, for their invaluable help throughout this project. They made the perfect team, he helping me with everything related to lab work and simulation code, and she with planning and scientific writing. I can safely say that without their aid this project would not have been half of what it is today.

I would also like to thank

- The staff at the NanoLab cleanroom for offering me equipment training, and for being available for questions at all times.
- The other master student at our research group, Størk Avelsgaard Lien, for giving me a feeling of teamwork and common goals.
- My fiancé, Lars Olav Skrebergene, for his love and support throughout this emotional roller-coaster.
- The Nanotechnology student association, Timini, and all its members, for welcoming me to Trondheim and making my time as a student a wonderful one.
- My parents, Knut Jacob Windelstad Hellen and Liv Signy Gjeitnes Hellen, for always being there for me.
- A diverse set of characters who have brought me joy and taught me a lot about life.

List of abbreviations

a-Si Amorphous silicon
BAS Bulk and sleeve
BSA Glutaraldehyde-bovine serum albumin
BZ Brillouin zone
c-Si Crystalline silicon
CMOS Complementary metal-oxide-semiconductor
DC Direct current
DI Deionized
DNA Deoxyribonucleic acid
e-beam Electron beam
EBL Electron beam lithography
EDX Energy-dispersive X-ray spectroscopy
FDTD Finite-difference time-domain
FIB Focused ion beam
Harminv Harmonic Inversion of Time Signals by the Filter Diagonalization Method
ICP-RIE Inductively coupled plasma reactive ion etching
IPA Isopropanol
Meep MIT Electromagnetic Equation Propagation
MPB MIT Photonic Bands
PBG Photonic band gap
PEC Proximity effect correction
PECVD Plasma-enhanced chemical vapor deposition
PhC Photonic crystal
PML Perfectly matched layer
RF Radio frequency
SEM Scanning electron microscope
SOI Silicon-on-insulator
TE Transverse-electric
TM Transverse-magnetic

Contents

Chapter 1

Introduction

Every day, hospital laboratories work on analyzing the amount of certain compounds in the patients fluids to help in determining a diagnosis. While this works fairly well, it requires a large amount of infrastructure and well-educated personnel, resources that might be limited in some parts of the world. It is also quite time-consuming, especially if the samples have to be sent to the nearest laboratory. This thesis comprises part of a large research endeavor at NTNU, with the goal of creating a better alternative, called a lab-on-a-chip. The idea is for this small device to consist of many tiny biosensors, which allow it to quickly detect the amounts of many given compounds in our body fluids in parallel, while also being precise and accurate. In addition, it should be cheap enough that it can be thrown away after use.

Many small biosensors are already commercially available, including pregnancy tests and glucose meters. However, these sensors are often target-specific, which means that they can only be used to detect one single substance, and are therefore unsuitable for integration into a lab-on-a-chip. Photonic crystal based sensors are an interesting alternative. Photonic crystals (PhC) are periodic structures of varying dielectric constants, which provides them with a unique band structure, including band gaps, and an ability to control the light flow as a function of frequency and polarization [6, 7]. These properties were first discovered by Yablonovitch and John in 1987, and the discovery has caused photonic crystals to become a subject of intensive study ever since [8–10].

The photonic crystal based biosensors form part of a family of non-destructive, label-free photonic sensors, and work by detecting changes in the refractive indexes of their surroundings [11–17]. They are originally not target-specific, but can be made so by attaching target-specific capture agents to the surface of the sensors. Their other advantages include narrow resonances, simple optical read out techniques and a compatibility with existing CMOS fabrication techniques.

The goal of this project is to design and fabricate a photonic crystal drop filter for use in biosensing. A drop filter consists of a resonator situated between two waveguides, making it possible for a set of discrete resonance frequencies to drop from one waveguide to the other, hence the name. Both the theory of photonic crystals, drop filters and resonators, and how it can be used for biosensing, will be explained more thoroughly in chapter 2. The crystal itself will be made from silicon due to its compatibility with the available fabrication equipment, making the road

from research to application shorter. The project will to some extent build upon previous work by the lab-on-a-chip research group at NTNU [1–5, 18].

The structure is subject to a series of requirements, with the goal of making the detection as accurate and precise as possible. These are listed in chapter 4, along with the procedures performed during the project. This includes both 2D and 3D simulations to help optimize the design before fabrication, as well as performed fabrications and an optimization of certain parts of the fabrication method. The tools used during the procedures and characterizations are explained in chapter 3, along with the fabrication method. All results are presented and discussed in chapter 5. Finally, the most important findings are repeated in chapter 6, along with ideas for future research in the field.

Chapter 2

Theory

2.1 Photonic crystals

Photonic crystals (PhCs) are periodic structures of varying dielectric constants with unique optical properties. In many ways they resemble semiconductors, in that they have energy gaps where, no matter the wave vector, no wave can propagate. Instead, the light is reflected. This property is very useful for many reasons, and in section 2.4 it will be described how it can be utilized in biosensing. First, however, some PhC theory is necessary to understand the workings of such a biosensor. It will be assumed that the reader possesses some very basic knowledge of photonics, quantum physics and solid state physics. The theory will be based on [6], and the interested reader is referred to it, as it is both more detailed than this section and contains several interesting topics that are not considered relevant here. However, while it covers all topics addressed in this section, important concepts have been verified with other sources.

2.1.1 Electromagnetism in a mixed dielectric media

The goal of this section is to present the derivation of some important equations that will prove invaluable in understanding the nature of PhCs. It will start out by considering the Maxwell's equations:

$$\begin{aligned} \boldsymbol{\nabla} \cdot \mathbf{B} &= 0 \\ \boldsymbol{\nabla} \cdot \mathbf{D} &= \rho \\ \boldsymbol{\nabla} \times \mathbf{E} + \frac{\partial \mathbf{B}}{\partial t} &= 0 \\ \boldsymbol{\nabla} \times \mathbf{H} - \frac{\partial \mathbf{D}}{\partial t} &= \mathbf{J}. \end{aligned} \tag{2.1.1}$$

Note that all equations will be given in SI units. $\mathbf{E}$ and $\mathbf{H}$ are the macroscopic electric and magnetic fields, while $\mathbf{D}$ and $\mathbf{B}$ are the displacement and magnetic induction fields, respectively. ρ and $\mathbf{J}$ are the free charge and current densities, and will be assumed to be equal to zero. $\partial/\partial t$ is the partial time derivative. Assuming that the medium is linear, isotropic and non-dispersive, and that the relative permittivity

$\varepsilon(\mathbf{r})$ is real and positive, then

$$\begin{aligned} \mathbf{D}(\mathbf{r}) &= \varepsilon_0 \varepsilon(\mathbf{r}) \mathbf{E}(\mathbf{r}) \\ \mathbf{B}(\mathbf{r}) &= \mu_0 \mu(\mathbf{r}) \mathbf{H}(\mathbf{r}). \end{aligned} \tag{2.1.2}$$

Here, $\varepsilon_0 \approx 8.854 \times 10^{-12}$ F/m is the vacuum permittivity and $\mu_0 = 4\pi \times 10^{-7}$ H/m is the vacuum permeability. $\mu(\mathbf{r})$ is the relative magnetic permeability, and will be assumed equal to 1 for all materials considered here. This gives us a new set of equations:

$$\begin{aligned} \boldsymbol{\nabla} \cdot \mathbf{H}(\mathbf{r}, t) &= 0 \\ \boldsymbol{\nabla} \cdot [\varepsilon(\mathbf{r}) \mathbf{E}(\mathbf{r}, t)] &= 0 \\ \boldsymbol{\nabla} \times \mathbf{E}(\mathbf{r}, t) + \mu_0 \frac{\partial \mathbf{H}(\mathbf{r}, t)}{\partial t} &= 0 \\ \boldsymbol{\nabla} \times \mathbf{H}(\mathbf{r}, t) - \varepsilon_0 \varepsilon(\mathbf{r}) \frac{\partial \mathbf{E}(\mathbf{r}, t)}{\partial t} &= 0. \end{aligned} \tag{2.1.3}$$

Both $\mathbf{E}$ and $\mathbf{H}$ are time-dependent, which complicates things. However, since Maxwell's equations are linear, the time dependence can be separated from the spatial dependence:

$$\begin{aligned} \mathbf{H}(\mathbf{r}, t) &= \mathbf{H}(\mathbf{r}) e^{-i\omega t} \\ \mathbf{E}(\mathbf{r}, t) &= \mathbf{E}(\mathbf{r}) e^{-i\omega t}, \end{aligned} \tag{2.1.4}$$

where ω is the angular frequency. Inserting these equations into the two last equations of 2.1.3 and solving, we get

$$\begin{aligned} \boldsymbol{\nabla} \times \mathbf{E}(\mathbf{r}) - i\omega \mu_0 \mathbf{H}(\mathbf{r}) &= 0 \\ \boldsymbol{\nabla} \times \mathbf{H}(\mathbf{r}) + i\omega \varepsilon_0 \varepsilon(\mathbf{r}) \mathbf{E}(\mathbf{r}) &= 0. \end{aligned} \tag{2.1.5}$$

Combining these we finally reach the Master Equation [6, 7]

$$\boldsymbol{\nabla} \times \left(\frac{1}{\varepsilon(\mathbf{r})} \boldsymbol{\nabla} \times \mathbf{H}(\mathbf{r}) \right) = \left(\frac{\omega}{c} \right)^2 \mathbf{H}(\mathbf{r}). \tag{2.1.6}$$

Here, $c = 1/\sqrt{\varepsilon_0 \mu_0}$ is the speed of light in vacuum. A very interesting quality of the Master Equation is that it has no fundamental length scale. If one were to replace $\varepsilon(\mathbf{r})$ with $\varepsilon(\mathbf{r}/s)$ in the Master Equation, where s is a random scalar, then the result would simply be a new Master Equation, with re-scaled mode profiles and frequencies. Similarly, there is no fundamental value for the dielectric constant, meaning that dividing the constant for all $\mathbf{r}$ by s^2, would give a new Master Equation, but with ω doubled by s. A similar equation can be calculated for $\mathbf{E}$, but for practical reasons it is much easier to just use Equation 2.1.6.

The equation above is merely an eigenvalue problem, similar to the Schrödinger equation, and it can be simplified by defining an operator $\widehat{\boldsymbol{\Theta}}$ as

$$\widehat{\boldsymbol{\Theta}} \mathbf{H}(\mathbf{r}) \equiv \boldsymbol{\nabla} \times \left(\frac{1}{\varepsilon(\mathbf{r})} \boldsymbol{\nabla} \times \mathbf{H}(\mathbf{r}) \right). \tag{2.1.7}$$

Note that $\widehat{\mathbf{\Theta}}$ is a linear operator, which means that any solution of $\widehat{\mathbf{\Theta}}$ times a constant is also a solution of $\widehat{\mathbf{\Theta}}$. As with the Hamiltonian, $\widehat{\mathbf{\Theta}}$ is also a Hermitian operator, shown by the fact that

$$(\mathbf{F}, \widehat{\mathbf{\Theta}}\mathbf{G}) = (\widehat{\mathbf{\Theta}}\mathbf{F}, \mathbf{G}), \tag{2.1.8}$$

where the inner product of two vectors is defined as

$$(\mathbf{F}, \mathbf{G}) \equiv \int \mathrm{d}^3\mathbf{r}\mathbf{F}^*(\mathbf{r}) \cdot \mathbf{G}(\mathbf{r}). \tag{2.1.9}$$

In fact, there are many similarities between the Hamiltonian and $\widehat{\mathbf{\Theta}}$, relying on the fact that they are both Hermitian. Their eigenfunctions possess some of the same key qualities, namely that they have real eigenvalues, they are orthogonal ($(\mathbf{H}_1, \mathbf{H}_2) = 0$), they can be obtained by a variational principle and they can be sorted by their symmetry properties. A justification for these statements is given in chapter 2 of [6], but this text will limit itself to simply stating the variational theorem:

$$U_f(\mathbf{H}) \equiv \frac{(\mathbf{H}, \widehat{\mathbf{\Theta}}\mathbf{H})}{(\mathbf{H}, \mathbf{H})} = \frac{\int \mathrm{d}^3\mathbf{r}|\boldsymbol{\nabla} \times \mathbf{E}(\mathbf{r})|^2}{\int \mathrm{d}^3\mathbf{r}\varepsilon(\mathbf{r})|\mathbf{E}(\mathbf{r})|^2}. \tag{2.1.10}$$

U_f is called the Rayleigh quotient or the electromagnetic "energy" functional, and can be minimized by the lowest-ω $\mathbf{H}_0$. The next electromagnetic eigenmode, $\mathbf{H}_1$, must minimize U_f while also being orthogonal to $\mathbf{H}_0$, and so on. Considering Equation 2.1.10, it can be seen that a way of minimizing U_f is to either minimize the spatial oscillations of $\mathbf{E}$, thus minimizing the numerator, or concentrate $\mathbf{E}$ in the regions of highest ε, thus maximizing the denominator [6, 7]. Since U_f has magnetic fields both above and below the fraction line, it is independent of the field strength.

2.1.2 Symmetry

A photonic crystal has a discrete translational symmetry in at least one direction. Imagine a structure of two periodically alternating layers with different permittivity, where each layer is parallel to the xy-plane and the lattice constant is a. Such a structure will have $\varepsilon(\mathbf{r}) = \varepsilon(\mathbf{R} + \mathbf{r})$, where $\mathbf{R} = l\mathbf{a} = la\widehat{\mathbf{z}}$ and l is an integer. We can also imagine that the layers are infinitely large in the x direction, causing it to have continuous translational symmetry in this direction, while being limited in the y direction.

Due to the translational symmetry, $\widehat{\mathbf{\Theta}}$ must commute both with all of the translation operators in the x direction, and with the translation operator for lattice vectors $\mathbf{R}$. These translational operators are given as

$$\begin{aligned} \widehat{\mathbf{T}}_{d\mathbf{x}} e^{ik_x x} &= e^{ik_x(x-d)} = e^{-ik_x d} e^{ik_x x} \\ \widehat{\mathbf{T}}_{\mathbf{R}} e^{ik_z z} &= e^{ik_z(z-la)} = e^{-ik_z la} e^{ik_z z}, \end{aligned} \tag{2.1.11}$$

where $e^{ik_x x}$ and $e^{ik_z z}$ are the eigenfunctions. An interesting thing to notice about the last formula above, is that insertion of $k_z + m(2\pi/a)$, where m is an integer, gives the exact same eigenvalue as simply inserting k_z. We therefore call $\mathbf{b} = b\widehat{\mathbf{z}}$, where $b = 2\pi/a$, the reciprocal lattice vector.

By remembering that any linear combination of the eigenfunctions is itself an eigenfunction, it can be deduced for our 3D structure that

$$\begin{aligned}\mathbf{H}_{k_x,k_z}(\mathbf{r}) &= e^{ik_x x}\sum_m \mathbf{c}_{k_z,m}(y)e^{i(k_z+mb)z} \\ &= e^{ik_x x}e^{ik_z z}\sum_m \mathbf{c}_{k_z,m}(y)e^{imbz} \\ &= e^{ik_x x}e^{ik_z z}\mathbf{u}_{k_z}(y,z).\end{aligned} \tag{2.1.12}$$

This means that $\mathbf{H}$ is simply a product of a plane wave and a z-periodic function $\mathbf{u}$. The formula above can further be generalized for a 3D periodic system as

$$\mathbf{H}_\mathbf{k}(\mathbf{r}) = e^{i\mathbf{k}\cdot\mathbf{r}}\mathbf{u}_\mathbf{k}(\mathbf{r}), \tag{2.1.13}$$

where the Bloch wave vector $\mathbf{k} = k_1\mathbf{b}_1 + k_2\mathbf{b}_2 + k_3\mathbf{b}_3$ lies in the Brillouin zone (BZ), and $\mathbf{u}_\mathbf{k}(\mathbf{r})$ is subject to the transversality constraint

$$(i\mathbf{k} + \boldsymbol{\nabla})\mathbf{u}_\mathbf{k} = 0. \tag{2.1.14}$$

It is important to note that the electric and magnetic fields, $\mathbf{E}$ and $\mathbf{H}$, can become spatially bound if they are either localized around a certain point, for instance a defect in an otherwise periodic structure, or because they are periodic in all three dimensions. For such a spatially bounded field, the frequencies ω form a discrete set, while in all other cases they will at least be partially continuous. However, since $\mathbf{k}$ is a continuous parameter, the frequencies in this set are themselves a continuous function of $\mathbf{k}$. The sum of all these continuous lines are called the band structure of the crystal, and can be described mathematically by $\omega_j(\mathbf{k})$, where j indexes the bands in order of increasing frequency. It is very complicated to calculate the band structure, but it can be done numerically by solving the equation that arises when Equation 2.1.13 is inserted into the Master Equation 2.1.6:

$$\left[(i\mathbf{k} + \boldsymbol{\nabla}) \times \frac{1}{\varepsilon(\mathbf{r})}(i\mathbf{k} + \boldsymbol{\nabla})\times\right]\mathbf{u}_\mathbf{k}(\mathbf{r}) \equiv \widehat{\boldsymbol{\Theta}}_\mathbf{k}\mathbf{u}_\mathbf{k}(\mathbf{r}) = \frac{\omega(\mathbf{k}^2)}{c^2}\mathbf{u}_\mathbf{k}(\mathbf{r}). \tag{2.1.15}$$

It can be worth noting that not all values of $\mathbf{k}$, as limited by the BZ, have to be calculated. In fact, since a perfect photonic crystal always has some sort of rotational and mirror symmetry in real space, so does the BZ. For instance, a 2D square lattice has a 2D square BZ, where both real and reciprocal space have a 90 degree rotational symmetry and a mirror symmetry, causing only 1/8 of the BZ to be unique [6, 7]. This unique part is called the irreducible BZ, and all other parts of the BZ are simply a copy of it.

2.1.3 1D PhCs and the appearance of the band gap

To understand the more complicated case of the two-dimensional photonic crystal slab that will be the center of this project, it can be nice to first understand some basic principles by focusing on the 1D case. Here, we will work with a stack of 2

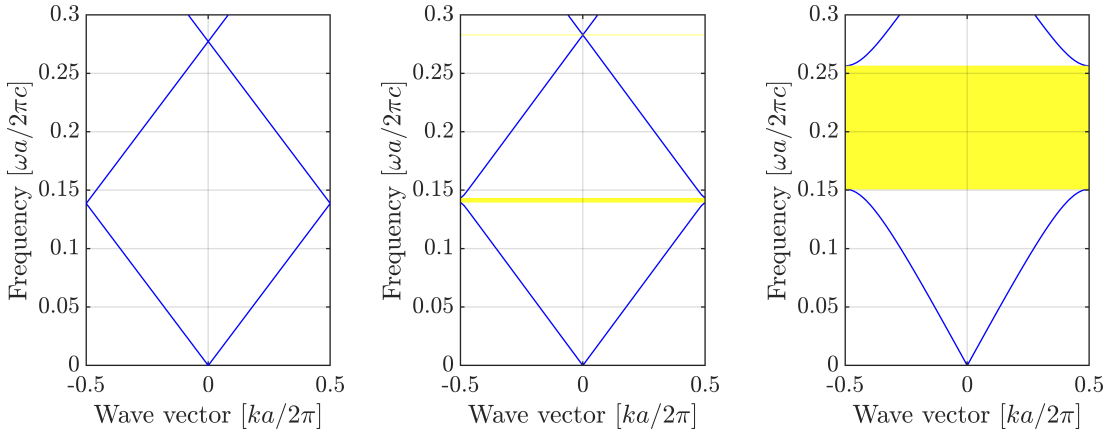

(a) $\varepsilon_{\text{var}} = 13$ (b) $\varepsilon_{\text{var}} = 12$ (c) $\varepsilon_{\text{var}} = 1$

Figure 2.1: The above figure shows the band structure for three different multilayer films, all of them consisting of two alternating layers with a thickness of $0.5a$ each. For one of the layers the permittivity is constant at $\varepsilon_{\text{const}} = 13$, while the other layer has a varying permittivity ε_{var}, where each figure shows a different choice of this variable. The band gaps are shown as bulks of yellow.

periodically alternating layers with different permittivity, where each layer is $0.5a$ thick and parallel to the xy-plane. This becomes even simpler by assuming that the layers extend infinitely in both the x and y directions.

As can be seen by Figure 2.1, a photonic band gap (PBG) appears and increases in size for an increasing $\Delta\varepsilon = \varepsilon_{\text{const}} - \varepsilon_{\text{var}}$ [6, 7]. The gap is considered complete, meaning that for a given range of frequencies, no valid wave vector $\mathbf{k}$ exists. This implies that certain frequencies are banned from the crystal, and the photonic crystal can therefore be considered a frequency selective mirror. Inside the crystal, the wave amplitude of such a frequency will decay exponentially:

$$\mathbf{H}(\mathbf{r}) = e^{ikz}\mathbf{u}(z)e^{-\kappa z}, \tag{2.1.16}$$

where κ can be interpreted as the decay rate, and $k + i\kappa$ is the complex wave vector. Such modes are called evanescent, in contrast to the extended modes described earlier. The larger the distance $\Delta\omega$ from the closest band edge, the larger is κ, and the smaller is the penetration of light into the crystal. For that reason, it is possible to localize a mode near the center of the band gap much more effectively than near the edge of the band gap.

Notice the scaling of the axes in Figure 2.1. As mentioned earlier, the Master Equation has no fundamental length scale. This means that a rescaling of the lattice constant a would simply cause a rescaling of ω and $\mathbf{k}$ as well, making it meaningless to name the axes as ω and k. Instead, we use dimensionless units, both in representation of data and in simulation tools:

$$\omega_n = \frac{\omega a}{2\pi c} \quad \text{and} \quad k_n = \frac{ka}{2\pi}. \tag{2.1.17}$$

To understand why the PBG appears, it is important to remember the variational theorem, which states that to minimize the electromagnetic energy, the spatial oscillations should be kept to a minimum, while the electric field should be concentrated

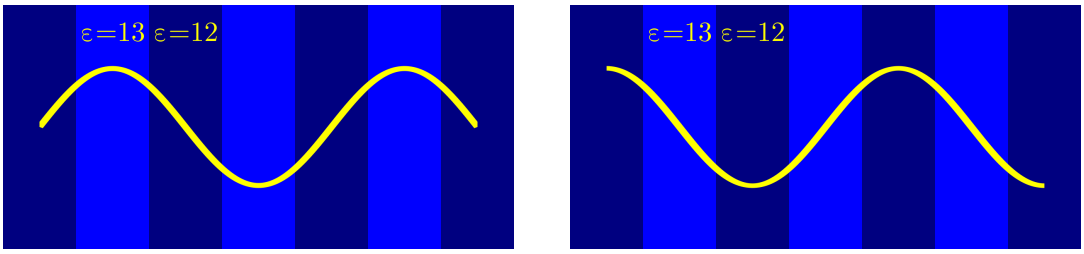

(a) First band (b) Second band

Figure 2.2: The electric fields for the bands belonging to 2.1(b) at $k = \pi/a$ are shown. The light blue areas represent a material with $\varepsilon = 13$, while the dark blue areas has a $\varepsilon = 12$.

in the regions of highest ε. Now, considering Figure 2.1(b) for $k = \pi/a$, i.e. at the band edge, and remembering to keep the discrete translational symmetry, one might guess the structure of the electric field for the two photonic bands: For the lowest band, the electric field forms a wave with wavelength $\lambda = 2\pi/k = 2a$, and extremes in the regions of highest ε. For the highest band, the wavelength is identical to the lower band, but the nodes are in the regions of highest ε, causing it to have a significantly higher energy, as explained by the variational theorem and shown in Figure 2.1 and Figure 2.2. For Figure 2.1(c), the electric field will look a little different. Due to the large $\Delta\varepsilon$, it becomes relatively more important to concentrate the electric field in the high-ε regions, than to limit spatial oscillations. Therefore, while the upper band is still forced to have its nodes in the high ε layer, it has a very high derivative there, causing a fairly large part of the field to be concentrated in the high ε layer.

Due to the scalability of our result, the band gap cannot simply be characterized by $\Delta\omega$, as this value depends on the size of the lattice constant. Instead, we describe the band gap by using the unitless gap-midgap ratio $\Delta\omega/\omega_m$, where ω_m is the frequency in the middle of the PBG.

The band gap is only complete if the crystal is perfect. If the crystal instead contains a defect, for instance a layer of different thickness or permittivity than the others, this defect can become home to a mode with frequency inside the band gap. In fact, if you imagine light being able to somehow reach this defect, then it would have trouble escaping, since the crystal surrounding it would act as mirrors. This resembles the effect seen in a Fabry-Pérot resonators, as will be explained in section 2.2. The confinement increases in strength if the mode has a frequency close to the center of the band gap. This type of mode confinement can also occur on the surface of the layered stack. In that case, the mode is localized by the crystal on one side and, if its frequency is below the light line $\omega = kc$, by air on the other side.

2.1.4 2D photonic crystals

A two-dimensional photonic crystal has a certain periodicity in two directions, and is homogeneous in the third direction. This is actually quite similar to the photonic-crystal slab that is the focus of this project thesis, except that instead of being homogeneous in the third direction, it has a finite thickness h.

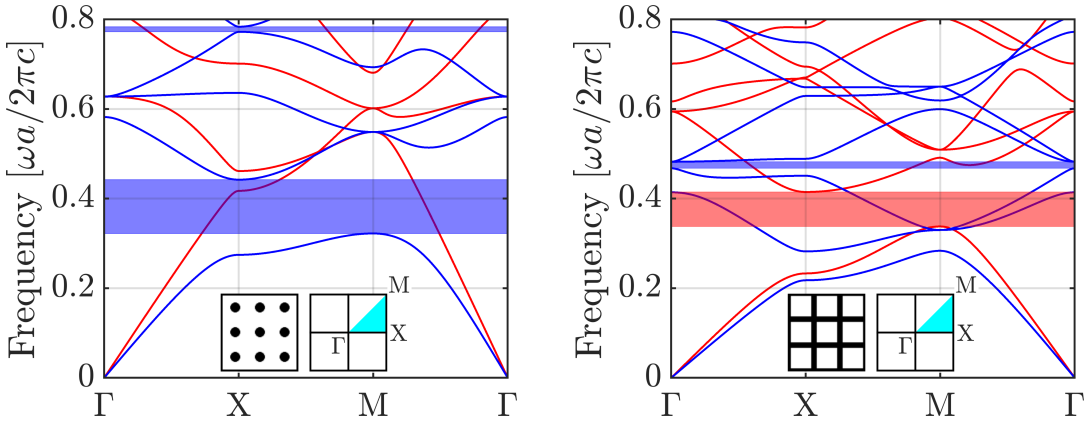

(a) Rods (b) Grid

Figure 2.3: The photonic band structure of two types of 2D crystals. The blue lines represent the TM modes, while the red lines represent the TE modes. A similar choice of color has been used for the photonic band gaps, which are seen as bulks of either red or blue. In each figure the left inset shows the cross-section of the crystal, where the black areas represent a dielectric with $\varepsilon = 8.9$, and the white areas are air with $\varepsilon = 1$. The rods have a radius of $0.2a$, while the veins in the grid have a thickness of $0.2a$. The right inset shows the BZ, where the light blue areas are the irreducible BZ.

Before continuing the discussion, it might be useful to introduce some nomenclature. All two-dimensional photonic crystals have a mirror symmetry around its homogeneous direction, here being the z-axis. This is true both in real space and in reciprocal space, causing $\widehat{\mathbf{z}} \to -\widehat{\mathbf{z}}$ and $M_z\mathbf{k}_\parallel = \mathbf{k}_\parallel$, where M_z is a reflection operator and $\mathbf{k}_\parallel$ is a wave vector parallel to the xy plane. For this reason, it is possible to classify all modes of such a crystal into two distinct polarizations: the transverse-electric (TE) mode where the electric field is confined to the xy plane, meaning that only the set (E_x, E_y, H_z) is unlike zero; and the transverse-magnetic (TM) mode where the magnetic field is confined to the xy plane, causing only (H_x, H_y, E_z) to be unlike zero.

With that in mind we can consider Figure 2.3. Figure 2.3(a) shows the band structure of a lattice of infinitely long alumina rods in air, while Figure 2.3(b) considers a square array of alumina veins. As can be seen in Figure 2.3(a), there is a significant gap between the maxima of the lowest blue line and the minima of the second lowest blue line, while there is no such gap for the red lines. This means that the photonic crystal has a band gap, but only for the TM polarized light. On the other hand, we can see that in Figure 2.3(b) there are two band gaps, one for TE only and one for TM only, but the band gap for the TE polarized light is by far the largest. To generalize this, we notice that the main difference between these two crystals is that in the left one, the high-ε areas are isolated, while in the right one they are connected. As a rule of thumb we can therefore say that TM band gaps are favored when the high-ε regions are isolated, while the TE band gaps are favored when they are connected. In many applications where a band gap is required, it might not be a problem that the band gap is polarization specific, as you can polarize the light before it enters the crystal. However, it is nice to have a band gap for all polarizations if possible, especially since coupling can occur between the TE and

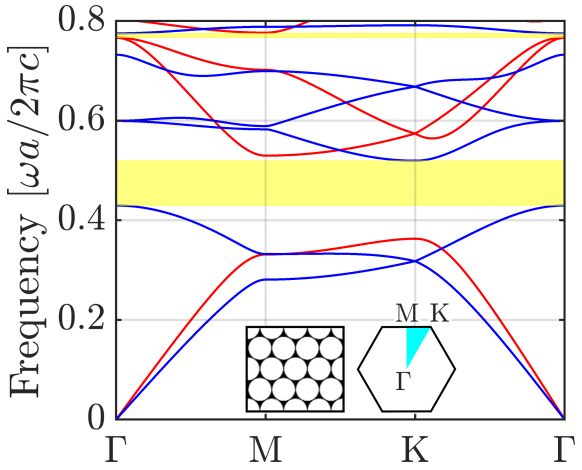

Figure 2.4: The band structure of the preferred arrangement for a 2D photonic crystal, where infinitely long rods are arranged in a hexagonal pattern. The blue lines represent the TM modes, while the red lines represent the TE modes. In contrast to Figure 2.3, this structure has several band gaps for both polarizations at the same time, shown in yellow. In addition, there are several polarization specific band gaps. The right inset shows the BZ of the crystal, while the left inset shows its cross-section. The rods are made of air ($\varepsilon = 1$), while the surrounding are made of a dielectric substrate with $\varepsilon = 13$.

TM modes for some PhCs. This will be discussed in more detail in subsection 2.1.5.

A band gap for both polarizations can be made by making a compromise between the two structures, where the high-ε regions are only barely connected. Such a structure is shown in the left inset of Figure 2.4. By adjusting the radius of the air rods relative to the lattice constant, which is here defined as the distance between the center of two neighboring rods, it is possible to make a band gap for both the TM and the TE modes and have them overlap. The band gap can therefore be considered complete.

While semiconductors are often doped to enhance their properties, photonic crystals are given defects. In a 2D photonic crystal, three types of defects can arise: line defects, point defects and surface defects. All of these defects can be made artificially by changing the dielectric constant of a column or a set of columns, or by changing their radius. In general, by decreasing ε of a rod relative to the rest of the rods, a positive frequency shift occurs, and a discrete mode arises from the band below the band gap, called the dielectric band. Equivalently, by increasing ε relative to the rest of the rods, a discrete mode will lower itself down from the air band (which is the band just above the band gap) into the band gap.

Since no real crystal can consist of an infinite number of rods, even the defect modes inside the PBG are not truly localized. Instead, they are resonances, having a nonzero leakage rate γ into the surrounding crystal, and a complex frequency $\omega_c = \omega_0 - i\gamma/2$. However, since defect modes decay exponentially inside the crystal, γ decreases exponentially with the number of crystal periods surrounding it. The loss rate can therefore become very small in a large crystal.

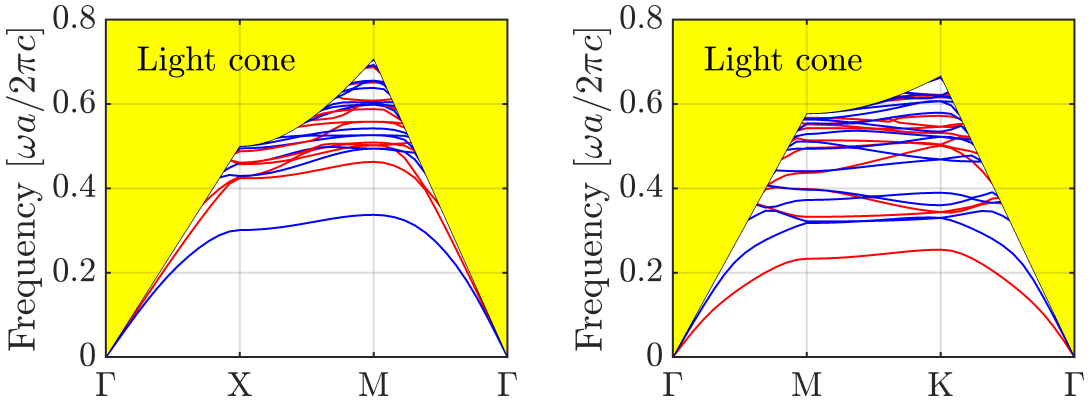

(a) Rod slab (b) Hole slab

Figure 2.5: Band diagram for two different photonic crystal slabs with $\varepsilon = 12$ suspended in air. The rods have a radius $r = 0.2a$ and the rod slab has a thickness $h = 2a$, while the hole slab uses a radius $r = 0.3a$ and a thickness $h = 0.6a$. The rods are ordered in a square grid, while the holes form a hexagonal pattern. The light cone is a set of extended modes in the surrounding air and is limited by the light line $\omega = kc$. The blue and red lines are the guided TM- and TE-like modes, respectively. Several incomplete, polarization specific band gaps can be seen in the structure.

2.1.5 Photonic-crystal slabs

This chapter will deal with structures similar to those mentioned in the previous section, except that we now will leave the ideal case of infinitely wide slabs and long rods, and instead look at structures with a finite extent in the z-direction. Such crystals are called photonic-crystal slabs.

As mentioned in the previous section, for a 2D photonic crystal with infinite width all modes can be classified as either TM or TE modes due to mirror symmetry about the xy plane. However, for a photonic-crystal slab of finite width, this mirror symmetry is only valid in the middle of the slab, by definition at $z = 0$. By continuity, the fields can only change gradually, causing the fields to be mostly TE- and TM-like for a slab thickness that is smaller than the wavelength. Of course, this argument is only valid if the slab is surrounded by the same medium on both sides, as anything else will break the mirror symmetry.

Figure 2.5 shows an example of band structures for two photonic-crystal slabs surrounded by air. The main difference relative to Figure 2.4 is the appearance of the light cone, here marked in yellow. This cone is limited by the light line $\omega = kc$, shown in black, and all modes with frequencies above the light line will to some extent radiate into the surrounding air. The light cone is present for all frequencies, causing the band gaps to be limited to some values of k below the light cone. The band gaps are therefore considered incomplete.

When making a photonic-crystal slab, there is an ideal slab thickness that optimizes the gap-midgap ratio of the PBG. If the slab is very thin the modes become only weakly guided. If, on the other hand, the slab is very thick, higher order modes can be pulled down into the gap, causing it to decrease. According to Joannopoulos et al., the ideal thickness has been found to be approximately half an effective wavelength. Remember that the wavelength in a medium of refractive index $n = \sqrt{\varepsilon\mu}$ is

given as $\lambda = \lambda_0/n$ [7]. For the TE-like modes, and therefore the TE-like band gap for the hole slab, the effective vertical wavelength is mostly determined by the material with the largest refractive index, i.e. the silicon, while for the TM-like modes it is determined mostly by the material with the smallest refractive index, i.e. the air. The ideal rod slab thickness is therefore significantly larger than the ideal hole slab thickness, which explains the choice of thickness done in Figure 2.5.

As mentioned before, every real crystal containing a defect, for instance a cavity, has a nonzero leakage rate γ. However, due to the scale invariance of photonic crystals, it is more convenient to characterize the loss by using the dimensionless quantity

$$Q \equiv \frac{\omega_0}{\gamma} = \frac{\omega_0 U}{P}. \tag{2.1.18}$$

Here, P is the outgoing power and U is the electromagnetic energy localized in the cavity. The quantity Q is called the quality factor, and can be understood as the number of optical periods that elapse before the energy of a defect mode has decayed by $\exp(-2\pi)$. If a graph of the outgoing power as a function of frequency is made for the mode, then $1/Q$ can also be understood as the fractional width at half maximum of the defect peak that occurs. In other words,

$$Q = \frac{\omega_0}{\Delta\omega}, \tag{2.1.19}$$

where $\Delta\omega$ is the full width at half maximum of the resonance peak. Since we often want such a peak to be as thin as possible so as to more easily be able to find its maximum and separate it from other peaks, it becomes a goal to reach a large quality factor. For a defect, for instance a missing hole, in a structure similar to the inset of Figure 2.4, there are two decay mechanisms. Firstly, the light can leak into the surrounding crystal. Secondly, it can leak into the surrounding air and, if present, the substrate. This gives a total decay rate

$$1/Q = 1/Q_{\text{crystal}} + 1/Q_{\text{z}}. \tag{2.1.20}$$

Therefore, even if the crystal extends over a large area in the xy plane, and the leakage rate into the surrounding crystal becomes very small ($1/Q_{\text{crystal}} \to 0$), the total leakage rate does not reach zero. Instead, $Q \to Q_{\text{z}} \neq 0$ for all crystals of finite width.

It is now fairly obvious that the choice of substrate, if any, greatly affects the quality factor. In general, most substrates tend to lower Q_{z} due to their large refractive indexes. This can be understood by realizing that the Fourier transform of a defect mode, which basically is a decaying exponential, becomes a Lorentzian-like peak centered at $k = \pi/a$. Since the radiation losses arise from the overlap between the peak and the light cone, and an increasing ε causes the light cone to lower itself in frequency, it is clear that an increase in ε causes Q_{z} to decrease. A way of limiting this is to use a substrate which has the same cross-section as the crystal along the xy plane, simply because it contains more air.

Another effect of adding a substrate is the loss of an $z = 0$ reflection symmetry. If the slab is unsymmetrical in the x and y directions as well, the TM- and TE-like modes will start coupling with each other. Considering Figure 2.5, we see that the

band gaps are only valid for either TM- or TE-like modes. Thus, any mode that was earlier confined by the gap, for instance a TE-like mode in a TE-like gap, can now couple to the other mode, i.e. the TM-like mode, causing the gap to become leaky. To limit this leakiness, one can use a substrate with low ε and/or restore the z-symmetry by depositing a "superstrate" similar to the substrate on top of the crystal. It is also an option to etch the periodicity of the crystal into the substrate.

A general principle in the making of electromagnetic resonators is that you can trade off localization for loss. Consider a ring resonator, which basically consists of a waveguide that is bent to form a circle, positioned in between two linear waveguides. By increasing the radius, the curvature decreases, causing the bend losses to decrease as well. In fact, Q_{z} grows exponentially with the ring radius. However, the cost is that the ring starts to support more modes and becomes larger. The same correlation between a delocalization and an increase in Q_{z} and modal density exists for photonic crystals. This delocalization can be done in several ways. For instance, if we have a defect rod with $\Delta\varepsilon$ relative to the rest of the rods, we can decrease $\Delta\varepsilon$ to achieve a small $\Delta\omega$ between the band gap edge and the defect mode. Since a small $\Delta\omega$ causes the mode to be only weakly localized, we can achieve a very large Q_{z}. Another way of making the point-defect mode larger is to make the defect itself larger, for instance by removing more than one rod from the rod slab [6, 19]. To understand why delocalization increases the radiative quality factor, remember that the more delocalized a mode is in real space, the more localized it is in reciprocal space. Thus, less of the already mentioned Lorentzian-like peak will overlap with the light cone, and the radiation losses will decrease.

2.2 Resonators

To understand the biosensing device that is the center of this project, a few basics regarding optical resonators must first be addressed. An optical resonator is a component which confines light with a certain frequency by reflecting it back and forth between two mirror-like structures [7]. The simplest and most famous example is the Fabry-Pérot resonator, which simply consists of two planar mirrors that face each other. However, a resonator can also be made using photonic crystals, for instance by removing one hole or a series of holes from a photonic-crystal slab, as demonstrated in Figure 2.6. The cavity will in this case consist of silicon instead of air, and the planar mirrors is replaced by a photonic crystal, which reflects all light for a given range of wavelengths.

To understand the workings of a photonic crystal resonator, it is essential to understand the simpler Fabry-Pérot resonator. Imagine a single beam of light going back and forth inside a resonator of length L. Since light in many ways behaves as a wave, this ray will start interfering with itself. For most frequencies, this will result in destructive interference, and the mode will die out. However, if the wavelength λ of the mode is such that

$$2L = q\lambda_q, \tag{2.2.1}$$

where q is an integer, then the light that has gone a round trip is in phase with the light that has not, and constructive interference will occur. Such a wavelength

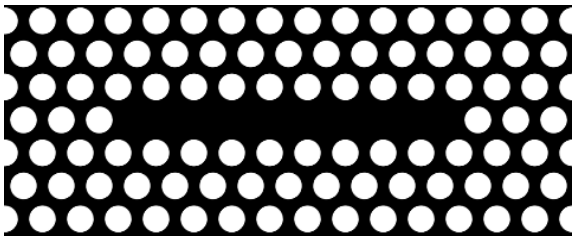

Figure 2.6: An optical resonator made by removing a series of holes from a photonic-crystal slab. The black area represent silicon, while the white areas represent air.

can therefore be sustained and confined in the resonator, and is called a resonance. Remember that $\lambda_q = \lambda_{q,0}/n$, where n is the refractive index of the resonator. Since light can be considered a Gaussian beam, it is not always completely confined to the resonator. In fact, a portion of the light will spread out into the vicinity of the resonator, and the refractive index of this vicinity will therefore affect the resonance wavelength slightly. For photonic-crystal hole slabs this vicinity consists of the area just above and below the slab, as well as the insides of the holes.

Equation 2.2.1 can also be given for frequencies, as

$$\nu_q = \frac{c}{\lambda_q} = \frac{cq}{2L}. \tag{2.2.2}$$

The frequency spacing between each resonance, called the free spectral range, can therefore be calculated as

$$\nu_F = \nu_{q+1} - \nu_q = \frac{c}{2L}. \tag{2.2.3}$$

This means that a longer resonator has a smaller distance between each mode and therefore has a larger mode density than a shorter resonator.

The spectral width of the resonator modes can be calculated as

$$\delta\nu \approx \frac{\nu_F}{\mathcal{F}} = \frac{c}{2L\mathcal{F}}, \tag{2.2.4}$$

for $\mathcal{F} \gg 1$, where

$$\mathcal{F} = \frac{\pi\sqrt{|\alpha|}}{1 - |\alpha|} \tag{2.2.5}$$

is the finesse of the resonator and $|\alpha|$ is the round-trip attenuation factor [7]. The latter can be understood as the loss of intensity due to medium absorption and the two reflections, and is always less than or equal to 1. A high reflectivity and low absorption will therefore result in a large value of $|\alpha|$ and $\mathcal{F}$, and a subsequent small value of $\delta\nu$. Since $1/Q$ can be understood as the fractional width at half-maximum of the resonance peak, as mentioned in subsection 2.1.5, this gives a large value of Q. The quality factor can also be increased by having a high value of L, as this would decrease $\delta\nu$.

2.3 Drop filter

The center of focus for this project thesis is an L_n drop filter, as shown in Figure 2.7. The figure is generated using MIT Electromagnetic Equation Propagation (Meep),

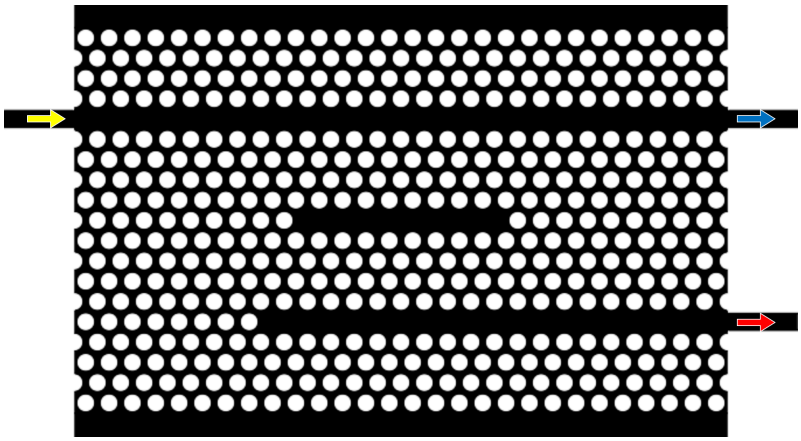

Figure 2.7: A typical photonic crystal drop filter. The black area represents silicon, while the white areas represent air. There are three linear defects. The upper and the lower defects both extend to the end of the crystal on at least one side, and will be referred to as waveguides. More specifically, the lower waveguide is referred to as the drop waveguide. The central defect has a shorter length, and is named the cavity. Such a linear cavity is called an L_n cavity, where n is the number of missing holes. The three arrows illustrates the light flow: the yellow arrow is the incoming light, the blue arrow is the transmitted light, and the red arrow is the dropped light. The x and y axes are defined to be in-plane, with the x axis parallel to the waveguides.

which is used for finite-difference time-domain (FDTD) simulations, tools which will be further explained in section 3.1 and Appendix A. The filter consists of a photonic-crystal slab with two waveguides and a resonant cavity. Light enters the crystal from the left strip waveguide, as illustrated by the yellow arrow. If we imagine that there was only one waveguide and no cavity, and that the frequencies that entered the crystal would lie in the band gap, then the light would simply follow the waveguide and exit on the opposite side, i.e. through the upper right strip waveguide. This light will be referred to as transmitted light, and is illustrated by a blue arrow. By adding the cavity and the second waveguide, an alternative route for the light opens up. Since the distances between the cavity and the waveguides are so short, the cavity is only able to confine light in the x-direction, allowing light to couple between the waveguides and the cavity. This makes it possible for a portion of the light to couple from the upper waveguide, through the cavity and out of the lower exit, as shown by the red arrow [20–22]. The structure can therefore be considered as a drop filter, since a certain set of frequencies, i.e. the resonances, are dropped to the lower waveguide.

2.4 Biosensing

The word biosensing refers to the process of transforming a physical quantity of a biological substance into a measurable signal. There are several methods for achieving this. One of them is frequently used by diabetics to measure the glucose level in blood, by transforming the concentration into an electrical signal [23]. This method is a label-free detection method, meaning that the target molecules do not

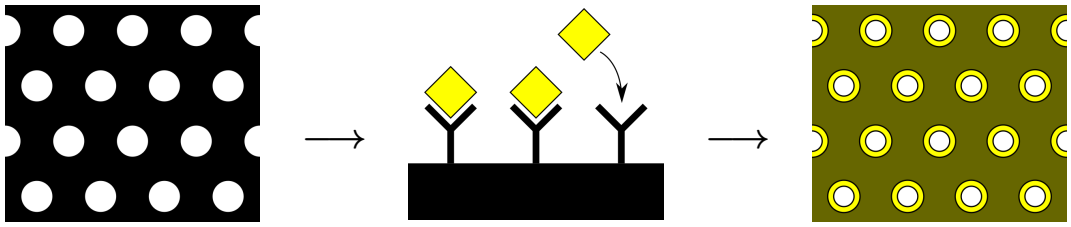

(a) (b) (c)

Figure 2.8: Binding of bio-molecules to a photonic crystal. (a) A photonic crystal slab as seen from above. The black area represent silicon and the white areas represent water. (b) The yellow squares are the target molecules that we want to detect. The black capture agents can be a strand of DNA, an antibody or any other target-specific molecule, and are fastened to the crystal before use. (c) The targets and capture agents creates a thick layer with a given refractive index, here shown in yellow, both inside the holes and on top of the slab. The layer may also form underneath the slab if no substrate is used.

have to be altered before detection [11]. This is also the case for the optical detection method described in this project.

Figure 2.8 shows the binding of target molecules to the surface of a photonic crystal, as explained in [14]. The black Y-shaped structures shown in 2.8(b) represent highly selective capture agents, for instance DNA or antibodies, which are attached to the surface of the holes in the crystal. In article [14], they are glutaraldehyde, and the yellow target molecules are glutaraldehyde-bovine serum albumin (BSA). Simply adding the capture agents causes a small redshift to the resonance peaks. By adding the target molecule as well, the redshift increases as a function of the target and capture agent coating thickness. This is in agreement with the theory described in section 2.2. Thus, it becomes possible to measure the concentration of targets in a solution by measuring the redshift of the resonance peak. In article [14], they were able to measure a monolayer with a total mass of only 2.5 fg. This indicates that a biosensor using photonic crystals to measure concentrations can achieve a quite high sensitivity. Other articles have achieved similarly promising results using various types of photonic crystal defects [12, 13, 15–17, 24].

Chapter 3

Methods and tools

Both when fabricating, characterizing and simulating a structure, the tools and methods of choice put some limitations on the accuracy of the result. It might be a fabrication tool that creates a small imperfection in the result, such as a small change of size for the fabricated object relative to the design, or a choice of simulation parameters that end up increasing the noise in the calculations. If these errors are to be handled and limited in the best possible way, it is necessary to have some information about their source. The goal of this chapter is therefore to give some basic information about the tools and methods used throughout the project, with an extra focus on their flaws.

3.1 Simulation

In theory every photonic crystal design suggestion could have been tested in the lab. However, this would take up enormous amounts of time and resources. Instead, simulation tools have been chosen to do the work. It is both faster and cheaper, and while it is not always exact, the most interesting results can simply be verified in the lab. The theory behind computational photonics is given below to enable the reader to better understand the advantages of the different simulation tools available. It is based on [6], and the reader is referred to it for a more thorough explanation of the methods.

All computational photonic problems can roughly be divided into three categories:

- Frequency-domain eigenproblems,
- Frequency-domain responses,
- Time-domain simulations.

A frequency-domain eigensolver solves the eigenequation 2.1.15 for the frequencies of a periodic system, where $\mathbf{u_k}(\mathbf{r})$ must satisfy the transversality constraint of Equation 2.1.14. To do this, the eigenequation is discretized into N degrees of freedom, yielding a finite, generalized eigenproblem $Ax = \omega^2 Bx$. Here, x is the eigenvector and A and B are $N \times N$ matrices. This gives the band structure of the

system. Since $\mathbf{u_k}(\mathbf{r})$ is periodic, the computation only needs to solve for the unit cell of the crystal, making it a fast and fairly simple method for small unit cells. The method is for instance used by a simulation tool named MIT Photonic Bands (MPB).

An example of a frequency-domain response solver is COMSOL Multiphysics. In such a simulation tool, the goal is to determine $\mathbf{E}(\mathbf{r})\exp(-i\omega t)$ and $\mathbf{H} = -\frac{i}{\omega\mu_0}\boldsymbol{\nabla}\times\mathbf{E}$ generated by a constant-frequency current source $\mathbf{J}(\mathbf{r})\exp(-i\omega t)$ in a linear media. This can be done by solving the following linear equation

$$\left[(\boldsymbol{\nabla}\times\boldsymbol{\nabla}\times) - \frac{\omega^2}{c^2}\varepsilon(\mathbf{r})\right]\mathbf{E}(\mathbf{r}) = i\omega\mu_0\mathbf{J_0}(\mathbf{r}), \tag{3.1.1}$$

which was obtained by solving the Maxwell equation 2.1.1 for $\mathbf{E}$ and $\mathbf{J}$. To do the numerical calculations, an infinite number of unknowns must be discretized into only N unknowns, and an $N \times N$ matrix equation of the form $Ax = b$ is obtained. Here x is the unknown electrical field and b is the known current. Intuitively, one would think that this would require $\mathcal{O}(N^2)$ memory and $\mathcal{O}(N^3)$ time. However, by using some iterative methods, only $\mathcal{O}(N)$ memory and time is required.

Finally, the time-domain simulation method is arguably the most general method of the three. The time-dependent Maxwell equations are solved for both time and space. Since the method does not rely on the frequency being conserved, it can easily handle strongly nonlinear or active media. The most common time-domain technique is the finite-difference time-domain (FDTD) method, as used by MIT Electromagnetic Equation Propagation (Meep). This method divides both time and space into a grid and, using finite difference, approximates the derivatives $\boldsymbol{\nabla}\times$ and $\frac{\partial}{\partial t}$ of the Maxwell equations. More specifically, the propagation in time uses a scheme where the $\mathbf{E}$ fields at a time t are calculated using the $\mathbf{E}$ fields at time $t-\Delta t$ and the $\mathbf{H}$ fields at time $t-\Delta t/2$. The $\mathbf{H}$ fields are calculated in a similar fashion.

Both the FDTD method and frequency-domain responses are used to calculate transmission spectra. When doing so, it is important that light exiting the simulation area disappears, instead of simply being reflected back into the crystal. This is solved by using a perfectly matched layer (PML) that creates a frame around the simulation area, absorbing all light that hits it.

The great advantage of the FDTD method is that, whereas the frequency-domain response method only calculates for one frequency at a time, the FDTD method can compute the response of the system to a spectrum of frequencies in a single simulation. This is done using the Fourier transform of the response to a short light pulse with a broad bandwidth. The method is therefore very efficient if you want to calculate the transmission spectra for a large range of frequencies. However, due to the uncertainty principle, the FDTD method requires a lot of time to calculate a spectrum for a very small range of frequencies. The FDTD method is also inefficient for calculating steady-states, as you have to wait for a very long time for the transient effects to die out. Also, frequency-domain methods might be better in cases where a highly non-uniform resolution is beneficial, since it allows exploitation of finite-element and boundary-element methods.

A nice quality of the time-domain methods is that they can be used to extract frequency eigenvalues. The method can therefore be used to find resonant

or leaky modes. However, since this method relies on identifying peaks in the response spectrum, some eigenfrequencies might be missed, or too many may be found. Frequency-domain eigensolvers, on the other hand, are both more reliable and faster at finding just a few eigenmodes.

3.1.1 MIT Electromagnetic Equation Propagation

This software, abbreviated Meep, is a free FDTD simulation tool [25]. The simulation space is split into a discrete grid, and discrete time steps are used to simulate the fields as a function of time and space. Light pulses with a given frequency width can enter the device, making it a time-efficient tool for calculating transmission spectra. It has therefore been used to create all such spectra in this project. However, this also means that the intensity of the source light is a function of frequency. Since Meep does not output this function directly, it has to be obtained by doing a reference simulation, for instance with a simple silicon strip waveguide. This reference waveguide was given the same width and height as the strip waveguides throughout this project, and well as the same length as the simulation space used for the photonic crystals. It was assumed that such a waveguide would have near perfect transmission, but this is not necessarily true. Instead, the transmission is dependent upon both the waveguide width, the waveguide length and the wavelength [26, 27]. Since the transmissions were calculated by dividing the results from the ordinary simulations on the transmissions from the reference runs, PhC transmissions of more than 100 % were sometimes obtained if the waveguide transmission became very low. This is of course impossible, and should be considered as nothing more than a simulation error.

A small grid and short time steps must be used to achieve a good result. It is also essential that the simulations are allowed to run for a sufficient amount of time. Stopping the simulations too soon might give too low intensities, as a significant fraction of the light might still be trapped inside the crystal. This is especially true for structures containing resonators, as these are capable of trapping the light for a long time, making the resonance intensity seem smaller than it should. A solution is to track the output at a given gate, in this case the forward drop gate, and stop the simulations when the output has reached a certain fraction of the maximum output through this gate. This fraction has been set to at least 1×10^{-3} for all simulations performed here. More precise simulations may use significantly smaller fractions, yielding a somewhat larger drop intensity at the resonance.

Meep is, in addition to being able to calculate transmission spectra, capable of calculating the resonance frequencies and quality factors of a resonator. This type of simulation is called a Harmonic Inversion of Time Signals by the Filter Diagonalization Method, or simply Harminv. Both the resonance frequencies and their quality factors can be obtained by analyzing the data found using the ordinary transmission mode mentioned before. However, Harminv mode is a lot faster, and requires very little data analysis. It can also give a more precise value for the quality factor, and is therefore used for all quality factor graphs in this project. As with the transmission mode, it has to run for a sufficient amount of time. All the simulations done here were run for 1000 Meep time units after the source was turned off, as this

seemed to give a fairly accurate result. Running the simulations for a shorter time would lead to inaccurate results, for instance by yielding too few resonances with too low quality factors. It is also important to use a narrow light pulse. According to Steven G. Johnson, who is one of the creators of Meep, this will limit the amount of resonances found by the software, and therefore the amount of noise corrupting the quality factor calculations [25, 28]. Negative quality factors are common symptoms of either too wide a light pulse, or too short a simulation time, and should never be given any physical meaning.

A tutorial on Meep can be found in Appendix A.

3.1.2 MIT Photonic Bands

MIT Photonic Bands (MPB) is a free simulation tool used for solving frequency-domain eigenproblems [29]. It allows for calculation of the band structure for any given unit cell, and can therefore be used both to calculate the band structure of a perfect PhC, and for more complex structures, such as PhC bends, as shown in subsection 4.3.1. However, while MPB is quite efficient for smaller unit cells, its efficiency decreases quickly with size. The simulation time will also increase when the number of photonic bands that are to be calculated increases.

A tutorial on MPB can be found in Appendix A of [2], Appendix C of [5], Appendix D of [30] and in the documentation pages for the software [31].

3.1.3 Effective index method

To obtain the most correct results, the simulations ought to be done in 3D. The simulation space would then include both the PhC slab, the surrounding air and the substrate. However, as this is very time demanding, the problem is often simplified to 2D using the effective index method. Instead of simulating the silicon with its actual refractive index, a weighted average of the index for silicon and its surrounding media is used. This weighting is determined based upon the amount of light concentrated within each layers, and the silicon will therefore be favored. The method has given quite good results for low-index contrast systems [32]. Unfortunately, the effective index will vary with the frequency used, especially if the system has high-index contrast, which is the case for silicon in air. This makes the method suitable for the system considered in this project if, and only if, the wavelength range is sufficiently small, typically smaller than 100 nm. It is often necessary to simulate transmission spectra with much larger wavelength ranges than that. However, the spectra are simply overviews to help find the most interesting normalized frequencies. In experimental work, a light source with an average wavelength of 1.55 µm and a bandwidth of approximately 100 nm will be used. The effective index has been calculated assuming this average wavelength, and the lattice constant can be calculated such that the wavelength range of the source will overlap with the normalized frequencies of interest. The effective index method is therefore valid.

3.2 Fabrication tools

3.2.1 Plasma cleaning

Plasma is a state of matter in the same way as solids, liquids and gases [33]. It can be induced by exposing certain gases to high-energy electric fields, as this will cause the molecules to split and create a high-energy collection of ionized molecules, neutral atoms and molecules, and free electrons. Unsurprisingly, such a collection is highly reactive and can, when interacting with a surface, form radical species, ionize neutral species, excite species and cause local heating of the surface. Plasma can also be quite useful during etching.

A sample surface can easily become contaminated, and must then be cleaned before the next processing step. A good way of doing this is through plasma cleaning. Since most of the contaminants are comprised of weak C – H bonds, they can be dissociated by mechanical bombardment of the sample surface using a plasma consisting of for instance oxygen [34]. The now dissociated contaminants are then free to react with the oxygen plasma, creating molecules such as H_2O, CO and CO_2. Due to the low pressure inside the reactor, these molecules will quickly evaporate, and can be evacuated from the chamber.

3.2.2 Plasma-enhanced chemical vapor deposition

Plasma-enhanced chemical vapor deposition (PECVD) takes advantage of a radio frequency (RF) induced plasma to enable chemical deposition at only a few hundred degrees Celsius [33]. This makes it possible to deposit on samples that would otherwise be ruined by the high temperatures created by other techniques. PECVD is also a fairly fast technique, has very good gap-filling properties for high aspect ratio gaps and can create a dense film with good adhesion to the wafer. Unfortunately, the deposited films are often neither stoichiometric nor crystalline.

The deposition must take place between two parallel conducting plates positioned inside a cold-wall vacuum chamber. The plates are typically separated by a variable gap of several cm in thickness. The bottom electrode is grounded and serves as a holder for the sample, while an RF power source is applied to the upper electrode. When the source gas enters the space between the two electrodes, the RF power causes the reactants to dissociate into radicals. These radicals start reacting with each other, and are absorbed on the top of the substrate, where a film is formed through diffusion and continued reactions. The bi-products are desorped and pumped out of the chamber through the periphery of the bottom electrode.

3.2.3 Electron-beam lithography

Lithography refers to the process of creating a patterned thin film on top of a sample. This thin-film, which is made out of and referred to as a resist, can later be used to protect certain areas during ion implants, lift off or etching, the latter of which will be discussed in more detail in the next section. There are several ways of creating the pattern once a uniform resist film has been deposited on the sample. Photolithography, which uses a light source and a quartz mask, is the most common

method in industry due to it being both fast and cheap. However, it has a fairly limited resolution and the production of the mask creates an extra fabrication step which makes it unsuitable for research. An alternative is therefore to use electron-beam lithography (EBL). Instead of using a physical mask to protect certain areas of the resist from a wide beam of light, the lithography pattern is input as a set of computer files. The EBL machine then uses a very thin electron beam which it scans across the areas that ought to be exposed. Additionally, EBL can achieve a resolution of less than 10 nm [35]. It is therefore widely used both for research and for photolithography mask production.

There are a total of 8 steps in the lithography method, but not all are mandatory, and the details of each are often resist dependent [33]:

1: Vapor prime

Step 1 prepares the wafer surface by cleaning, dehydrating and priming it, so as to achieve good adhesion between the wafer and the resist. The cleaning removes contaminants such as particles and native oxides. Afterwards, a dehydration may be done using a hot plate to remove moisture from the surface. The hot wafer must then be allowed to cool down before resist application, to avoid cracks caused by surface stress. Finally, the wafer may be primed with an adhesion promoter that serves to make the substrate and the resist chemically compatible.

2: Spin coat

Step 2 consists of covering the wafer with a resist suitable for EBL. A resist is a chemical that reacts in a certain way upon being exposed to a specific type of stimuli, in this case an electron beam. The chemical reactions may vary, but the result is always that the exposed resist either hardens or softens. In the first case the resist duplicates the pattern drawn by the electron beam in an inverse manner, and is therefore called negative, while in the latter the duplication is not inverse and the resist is considered positive [36]. Another resist characteristic is its sensitivity, i.e. the exposure dose needed per area for sufficient exposure, a value usually given in units of $\mu C/cm^2$.

The goal when applying the resist is to achieve a uniform layer of the correct thickness, while avoiding defects to form in the resist. A fairly easy way of getting sufficiently good results is to mount the wafer on a vacuum chuck, apply a good amount of resist and spin it for a given time and speed. These two parameters depend on the viscosity of the resist and the required resist layer thickness for future processing. Before moving on to the next step the sample should be cleaned underneath to remove resist residues.

3: Soft bake

The soft bake is done to deplete most of the solvent in the resist, making it solid. It also improves resist adhesion and uniformity, and is usually done with the help of a hot plate. Incorrect soft bake procedures can lead to stress in the resist and subsequent cracking, see subsection 5.2.2 for an example.

4: Exposure

During this step the electron beam scans and exposes the surface according to a set of computer files, called the mask. The files are made through a series of steps, the first one being to draw the lithography pattern. Several types of software are available for the task, for instance CleWin4. In addition, a series of exposure parameters are needed to finalize the exposure mask, and the rest of this subsection will therefore be devoted to explaining them.

The exposure dose is, as mentioned above, related to the sensitivity of the resist towards the electron beam. If the dose is too high, the resist will become over-exposed, increasing the significance of the proximity effect [2]. This effect describes how electrons, while entering at one spot on the resist surface, might scatter inside the resist and end up exposing at a neighboring spot instead. For example, if the goal is to create a positive resist film with a hole of radius r, even with the correct exposure dose, the final result might be a hole of radius $r + \delta r > r$. If the dose is larger than necessary, δr will become bigger, making the problem worse. If instead the dose is too small, the resist might not be fully removed from the hole, and upon subsequent etching it will protect the underlying sample and cause it to not be etched as much as it should, if it is etched at all.

It is often not optimal to use the same exposure dose on the entire pattern. Since many EBL patterns consist of both large, continuous areas and thin wires, the proximity effect might cause the large areas to be over-exposed, while the lack of proximity effect in the wires might cause them to be under-exposed. It is therefore often useful to use a proximity effect correction (PEC) tool. The PEC calculates the electron scattering using a Monte Carlo simulation and determines a dose factor for each spot that is to be exposed. The dose factor is then multiplied with the exposure dose, and, given that the exposure dose is optimal, the optimal exposure will be given for all parts of the pattern.

When increasing the beam current, the beam divergence increases as well due to a boost in the electrostatic repulsion between the electrons [35]. It therefore becomes possible to tune the beam size by varying the beam current. A small beam size gives the best resolution, and is a necessity for patterns containing very small structures. However, since a small beam size equals a very long exposure time, it should only be used when the pattern requires it. If a pattern consists of both large structures and small, critical details, it might be useful to use the Bulk and Sleeve (BAS) method. This is a software procedure where the geometry is split into its outer parts, called the sleeve, and the inner parts, called the bulk. An example is shown in Figure 3.1. Since the need for perfection is larger for the sleeve than for the bulk, a smaller current ought to be used for the sleeve, and the two parts of the pattern should therefore be exposed individually. However, the BAS method depends upon a change in current, which might cause the beam to drift if it is not given enough time to align after adjusting the current. While 45 min should be enough, this still adds quite a lot to the total exposure time, and alignment issues might still persist. It might help to create a small overlap between the bulk and sleeve, given that the alignment error is smaller than the overlap.

The EBL used in this project was permanently set to an acceleration voltage of 100 keV, and it was therefore considered futile to discuss the parameter in any

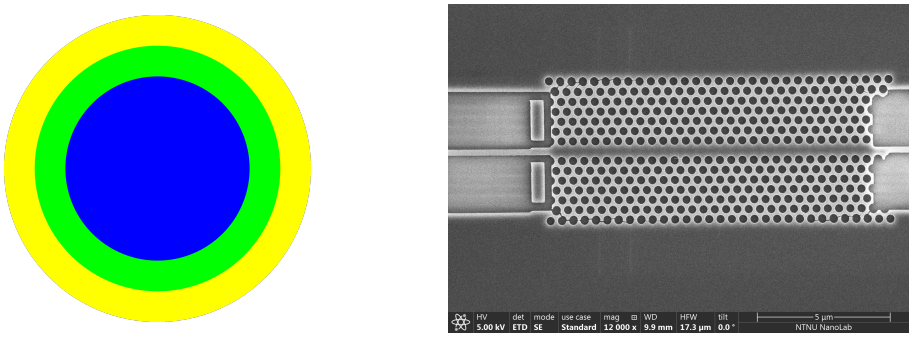

(a) (b)

Figure 3.1: Bulk and sleeve: (a) is a demonstration of the principle behind the bulk and sleeve method. The yellow areas represent the sleeve, while the blue areas are the bulk. The green areas are where the bulk and sleeve are made to overlap, to limit alignment errors. Typically, the sleeve is a couple of hundred nanometers wide. (b) is a SEM image of an etched SOI wafer. The two rectangular blocks of remaining silicon left of the PhC is a result of the sleeve being positioned approximately 600 nm too far to the right, and slightly too far up, relative to the bulk.

detail.

A write field is the area that can be exposed by simply deflecting the beam, without mechanically moving the stage. A typical write field size lies between 100 µm × 100 µm and 1 mm × 1 mm [2]. The benefit of having a large write field is less stitching errors, which are small alignments errors that inevitably occurs at the write field interface. However, a large write field also means that the beam must be deflected quite heavily to reach areas at the write field edge. Therefore, the greatest write fields can only be used with a smaller acceleration voltage. Alternatively, a smaller write field in combination with the multi-pass technique can be used. This technique involves exposing the pattern twice, with a small displacement of the write fields between the two exposures.

Each write field consists of an array of partially overlapping dots. An example would be a write field of 500 µm × 500 µm, with 1 000 000 × 1 000 000 dots and a resulting distance between each dot of 0.5 nm. It is important that this distance is smaller than the beam width to ensure overlap. However, not all dots are necessarily exposed. In fact, there is a limit to how little time can be used on each dot, in this case 10 ns/dot, before the machine starts to struggle. This limit can become a problem if the current is large relative to the exposure dose, and if the number of dots per area is large. Fortunately, it can be easily solved by skipping a few dots, as determined by the pitch. If the pitch is 1, every dot is exposed, but if it is 4, only every fourth dot is exposed.

5: Post-exposure bake

This step can be done to improve adhesion and reduce defects. It can also help catalyze the chemical reactions in the exposed regions for some types of resists.

6: Development

In this step, the resist is exposed to a liquid developer which causes the soluble parts of the resist to dissolve, leaving behind the pattern given by the mask. It is very important to control the development temperature and time, and to rinse properly afterwards to stop the development. If the development is done for too long or too short a time, the resist might get over- or underdeveloped, causing too much or too little resist to be dissolved, respectively.

7: Hard bake

The final baking process is done to evaporate the remaining resist solvent and to improve adhesion. Depending on the type of resist and what it will be used for, it is often an optional step.

8: Develop inspect

This final step consists of simply inspecting the resist pattern to see if the result is satisfactory. This can be done using for instance an optical microscope.

3.2.4 Inductively coupled plasma reactive ion etching

Dry etching is the preferred method for submicron etching due to its ability to achieve highly anisotropic, or vertical, sidewalls compared to wet etching techniques [33]. One such technique is the reactive ion etching (RIE), where an RF source induces a reactive plasma that is capable of providing both physical and chemical etching. The sample is positioned on a RF-powered electrode opposite a grounded electrode. A direct current (DC) self-bias occurs on the powered electrode as a result, giving rise to a large voltage difference relative to the plasma. This provides directionality for the ionized species moving towards the wafer, which is the reason why RIE is capable of obtaining anisotropic etching profiles.

While standard RIE uses the same RF source both to generate the plasma and to provide directionality to the ionized species, inductively coupled plasma RIE (ICP-RIE) uses two separate power sources. The reactor is split in two by a dielectric layer. In the upper half, a conductive spiral coil is responsible for inducing the plasma, while the sample is positioned in the lower half, on top of an RF-powered electrode. Having two power sources allows the ICP-RIE method to create plasma of much higher density than the standard RIE system. The reactor can therefore achieve anisotropic sidewall profiles even in high aspect ratio holes.

3.2.5 Scriber

A scriber is a tool used for cutting and breaking wafers along straight lines. It can be used to dice the wafer into samples, or simply to make a single cut with the goal of exposing some structure to the sample cross section. The cutting is done using a diamond tip. Unfortunately, this tip deteriorates over time, in a rate which depends upon the materials it is used to cut. Therefore, while the machine might be able to

make a very good cut when the diamond tip is new, an extremely poor result might be obtained when the tip has been used for some time. Note that the diamond does not cut all the way through the wafer. Instead, it makes a scratch, a weakness, on the wafer surface. A combination of an anvil on top of the wafer and a sharp impulse bar below it is then used for breaking the sample after the cutting has been performed. If the cut was sufficiently deep, the sample will break along the fracture line, as intended. However, if the diamond tip was old and the scratch shallow, the result might be a jagged scribe and a broken sample, or no break at all. Another challenge when using a scriber is that when breaking the sample, the anvil is in direct contact with the sample surface and can therefore damage it. A mylar sheet can be put between the wafer and the anvil to protect the sample surface, but this simple trick, while useful, is far from capable of solving the problem entirely. The wafer should therefore be cut such that the most vulnerable parts of the sample are sufficiently far from the cut, and thus the anvil. Unfortunately, this is not always possible.

3.3 The silicon-on-insulator system

Silicon-on-insulator, commonly abbreviated as SOI, has become a quite popular material for compact photonic devices. It consists of a silicon substrate covered first in a layer of silicon dioxide and then in a thinner layer of silicon. There are three main reasons for its popularity [37]. The first reason is that crystalline silicon has a very low absorption at wavelengths above 1200 nm. Secondly, the refractive index contrast (Δn) between Si ($n_{\mathrm{Si}} = 3.48$) and SiO_2 ($n_{\mathrm{SiO_2}} = 1.44$) is quite large, allowing for good light confinement even for sub-wavelength waveguide cross sections. The third reason for its popularity is its compatibility with the existing CMOS manufacturing processes, which allows for a quicker transition from research to mass-manufacturing.

The upper layer of silicon usually has a thickness of 220 nm [37]. This allows for single-mode behavior for each polarization at a wavelength of 1550 nm, which is the wavelength typically used in photonic crystal sensing. However, when etching away some of the silicon to make a waveguide, the width of the waveguide cannot be much larger than 520 nm if this single-mode behavior is to be kept. It is possible to obtain a single-mode behavior for thicker layers of silicon as well, but as a rule of thumb that will imply that the maximum waveguide width must be lowered.

Light passing through structures in the upper silicon layer will never be completely confined to the silicon. Instead, exponentially decaying tails extend into the underlaying oxide. If the oxide layer is too thin, the light might be able to leak into the silicon substrate, resulting in increased losses. The typical oxide layer thickness depends on the polarization of the light which will be used. In general, the TE polarization is better confined to the silicon layer, thereby allowing for a thinner oxide. A thickness of 1000 nm will typically work quite fine for the TE mode.

There are some disadvantages to using SOI in integrated photonic devices. First of all, since intrinsic silicon does not have a direct band gap, it is unsuitable for light generation. Secondly, while the large refractive index contrast is mainly a positive thing with regard to light confinement in the silicon layer, it also increases the

transmission scattering loss from interface imperfections [38]. Therefore, it becomes very important to limit any sidewall and interface roughness associated with the fabrication. Finally, it is very hard to grow high-quality crystalline silicon (c-Si) on top of an amorphous substrate such as thermally grown oxide [39], which is what was used in this work. A good solution to the last issue would be to use amorphous silicon (a-Si). While it mostly shares the characteristics of c-Si, it suffers from higher absorption losses in the wavelength range typically used in optical devices. However, the size of this loss depends upon the deposition conditions for the a-Si, and can be made quite low by using the PECVD method in combination with the right deposition conditions [39]. The PECVD method was explained in subsection 3.2.2.

The oxide layer can also be grown using PECVD. However, as shown in [2], the resulting film has a quite high degree of surface roughness compared to thermally grown oxide. Such an increase in roughness would greatly affect the transmission scattering losses and the PECVD method should therefore be avoided for the oxide layer. Pre-made silicon wafers covered with thermally grown silicon dioxide can be purchased and would be a better choice with regard to decreasing the surface roughness.

3.4 Fabrication methods

This section aims at describing the process used to fabricate the photonic crystals with sufficient detail for it to be reproducible. The tools used are listed in Table 3.1.

Instrument	Model	Manufacturer
Plasma cleaner	Femto	Diener Electronics
PECVD	PlasmaLab System 100-PECVD	Oxford Instruments
EBL	ELS-G100	Elionix
ICP-RIE	PlasmaLab System 100 ICP-RIE 180	Oxford Instruments
Scriber	DXIII	Dynatex

Table 3.1: Fabrication tools.

3.4.1 Thin film growth

Pre-made 4 inch silicon wafers covered with 1 µm of thermally grown SiO_2 were bought and cleaned using 2 min long sonication baths, first with acetone and then with ethanol. The sample was then rinsed using isopropanol (IPA) and dried with N_2 gas.

If a different chemistry had been used by the previous user of the PECVD, the chamber was preconditioned by depositing a-Si on a dummy wafer using the recipe given in Table 3.2, but with a longer growth time of 3 min. This was done to limit the amount of impurities in the deposited silicon layer. The wafer was then inserted into the PECVD, and a thin layer of a-Si was deposited using the parameters given in Table 3.2. After depositing the silicon layer, the wafer was scribed into square pieces, which will be referred to as samples from now on.

Parameter	Value
LF Power	200 W
Pressure	500 mTorr
Table Heater	300 °C
SiH_4	50 sccm
Ar	150 sccm
Growth time	273 s

Table 3.2: PECVD parameters. Note that the suggested growth time yields a silicon layer with a thickness of approximately 330 nm.

3.4.2 Resist patterning

Before patterning, the sample was cleaned again to remove dust from the scribing process. The cleaning was done similarly as in subsection 3.4.1, with 2 minutes long sonication baths in first acetone and then ethanol, followed by an IPA rinse. The sample was then dried using nitrogen gas and optically inspected for any remaining dust particles. Next, the sample was spin coated with a positive e-beam resist called AR-P 6200.13 (CSAR 62) for 60 seconds. By using a top speed of 3300 RPM and an acceleration of 500 RPM/s, a resist thickness of approximately 475 nm was obtained. After spin coating, the bottom of the sample was cleaned with acetone to remove any resist that might have deposited there. The resist layer was then inspected in an optical microscope to ensure that the amount of air bubbles and other imperfections was sufficiently small. If found satisfactory, the sample was baked on a hotplate for 180 s to evaporate solvents and harden the resist. The hot plate temperature had to be high enough to ensure that the resist reached a temperature of 150 °C, as shown in subsection 5.2.2. The sample was then put on a metal block to cool down before entering the EBL.

The sample would have to be scribed at the end of the fabrication to expose the beginning and end of the silicon structures to the cross sections and the incoming light. The fabricated structures could therefore not consist only of PhCs, since that would cause the sample to have a width of less than 50 µm given the lattice constants and the number of periods used in this project. Instead, strip waveguides were joined together with the PhCs at their inputs and outputs, and were a necessity to increase the size of the sample to something handleable. For an s period long photonic crystal with lattice constant a, the waveguides would have a length of $3\,\mathrm{mm} - sa/2$. While this made it much easier both to handle the sample and to scribe it, it also increased the total exposure time.

The resist pattern also included tapers, as shown in Figure 3.2. Subsection 3.5.2 explains how the laser light was coupled into the silicon structures from a tapered fiber by positioning the fiber in the plane of the sample and aiming it towards the silicon structures. Since the width of the strip waveguides would have to be less than 520 nm to fulfill the single-mode condition given the slab thicknesses used in this project, it would be quite hard to efficiently couple light into it. Instead, a taper was connected to the beginning of the input waveguide. The simplest taper design used in this project had, for its first 100 µm, a constant width of 5 µm, while

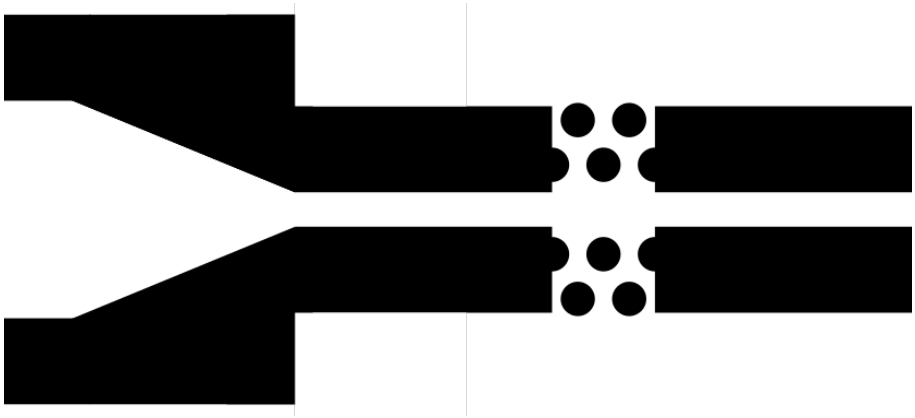

Figure 3.2: A simplified illustration of the mask design, including a taper, strip waveguides and a PhC. The black areas represent the margins and the PhC holes, and they will be exposed and subsequently etched. The figure is not to scale.

for its remaining 500 µm the width shrank linearly to match the width of the strip waveguides. While this taper could be easily made together with the rest of the silicon structures, its efficiency was limited due to it being tapered in only one dimension. An alternative would be the inverted taper. While it allows for 2D tapering, it also requires an extra lithography step. It was attempted used in this project, but was found both impractical and unnecessary, and was not used in any of the final works listed in chapter 4.

Since the CSAR 62 resist is a positive electron beam resist, the areas exposed to the beam are the ones without resist in the etching process, and thus the ones where the silicon will be removed. It would therefore not be efficient to remove all areas of silicon that did not partake in the photonic circuit. Instead, the strip waveguides and the tapers were made by removing a line of silicon on both sides. This margin would have to be both thick enough to avoid large amount of loss to the surrounding silicon, and thin enough to avoid extreme exposure times. A nice compromise would be 2 µm for the strip waveguides [3], while a wider margin of 8 µm was used for the tapers. The photonic crystal holes and margins were drawn in CleWin4, and then made into a mask using a software called Beamer [40]. Among other things, this software could be used to perform a PEC and a BAS, both methods which were explained in section 3.2.3. However, while the former method along with the multi-pass technique were used for all results listen in chapter 5, the latter, while attempted, was not used for any of them due it being both unnecessary and impractical.

As shown in [2], an area exposure dose of 350 µC/cm^2 was found to have a sufficiently large margin towards under-exposure, while still being small enough to avoid unnecessary proximity effects. It was therefore used throughout this project. The acceleration voltage was fixed by the machine to 100 kV, while the beam current varied between 100 pA and 5 nA: when using the BAS method, the bulk was exposed using a current of 5 nA, while the sleeve had a current of 100 pA. However, if this method was not used, a compromise of 1 nA was instead used for the entire structure, with a pitch of 5. The write fields had a size of 500 µm × 500 µm, and were split into 1 000 000 dots in each dimension.

After exposure, the resist was developed by placing the sample in the AR 600-546 developer for exactly 60 s. During this step, the sample was very gently moved around in the liquid to ensure uniform development. Quickly thereafter the sample was dipped in a beaker containing IPA to stop the developing process, before the sample was moved to another IPA beaker, where it was allowed to stay for 30 s. The sample was then either gently dried with nitrogen gas or allowed to air dry. The latter method was time-demanding, and were used only if the resist structure was very fragile. An example would be a structure consisting of thin lines of isolated resist that could easily be blown off by the nitrogen gas. The final resist pattern was inspected in an optical microscope. Sometimes, this inspection showed that the result was far from satisfactory, in which case the sample was stripped of resist and the process of adding a patterned resist was repeated.

3.4.3 Etching

Before etching, the sample was plasma cleaned for 1 min using 50 % oxygen and 50 % power. If the last user of the ICP-RIE had used a different chemistry, the chamber had to be preconditioned by etching a silicon dummy wafer for using the parameters given in Table 3.3, but with a longer etch time of 3 min. Afterwards the sample was placed on a carrier wafer and inserted into the ICP-RIE, where it was etched using the parameters listed in the table.

Parameter	Value
SF_6	7.5 sccm
CHF_3	50 sccm
Pressure	15 mTorr
CCP Power	40 W
ICP Power	600 W
Temperature	20 °C
Etch time	82 s

Table 3.3: ICP-RIE parameters. The etch time was suitable for a silicon layer thickness of approximately 330 nm.

3.4.4 Scribing and resist removal

The resist was removed by putting the sample in a beaker containing the AR 600-71 resist remover and doing an ultrasonic bath for 5 min. Afterwards, the sample was rinsed with IPA and dried with nitrogen gas. Alternatively, the sonication was skipped and the sample was instead put in the resist remover for 5 min, rinsed, air dried and then plasma cleaned for 3 min using 50 % oxygen and 50 % power. While the latter method was more time consuming, it could be necessary when making very thin strips of silicon, as the sonication might cause the silicon to fall off the oxide.

By using a combination of the scriber machine and a manual scriber the sample was cut at the ends and tapered beginnings of the waveguides, making it possible for light to both enter and exit the silicon structures. However, both the scribing by the diamond tip and the breaking by the anvil could damage the pattern. The former problem was solved by doing an edge-scribe, which involved only scribing a couple of millimeters into the sample, instead of scribing all across it, thus avoiding unnecessary scratching. The latter problem was partially solved by using a mylar sheet to cover the sample during breaking, and by having sufficiently long strip waveguides to avoid direct contact between the anvil and the photonic crystal.

3.5 Characterization

3.5.1 Scanning electron microscopy

The scanning electron microscope (SEM) is one of the most important measurement tools used in submicron manufacturing. It can achieve a maximum magnification of 100 000 to 300 000 times, and has a resolution on the order of 4 nm [33]. Where optical microscopes use photons to image the sample, a SEM uses electrons, making it important that the sample is conductive to avoid heating. However, given a conductive sample, little or no sample preparation is needed before imaging, and the sample is rarely damaged by the technique.

The entire process takes place inside a vacuum chamber at about 1×10^{-6} Torr. An electron gun produces a beam of electrons with adjustable energy, and the beam is then focused and directed using electrostatic-magnetic lenses and deflectors. The electron beam hits the sample within a small 2 to 6 nm spot, exciting secondary and backscattered electrons as well as other electrons, X-rays and photons. A SEM image is then made by scanning the sample and collecting and analyzing the secondary and backscattered electrons. While the former particle is best for achieving an optimal image resolution, the latter is mostly used to obtain contrast between different materials, since heavier elements scatter electrons more strongly. While the other emitted particles are ignored in this technique, they can play an essential role in other characterization tools often coupled to the SEM, such as energy-dispersive X-ray spectroscopy (EDX) and focused ion beam (FIB).

A dilemma when using a SEM is the choice of spot size. On one hand, a larger spot size implies a higher beam current, which is essential for achieving a large signal-to-noise ratio and a good contrast. However, a large spot size significantly limits the resolution that can be obtained by the SEM [41]. Therefore, if a high-resolution image is needed, contrast must be sacrificed.

3.5.2 Optical characterization setup

The goal of this section is to describe the optical characterization setup used during the project. It could be achieved easily by simply stating that light from a tunable laser source was sent through the sample and the output was detected using both a microscope and a photodetector. However, it would be interesting to give a more

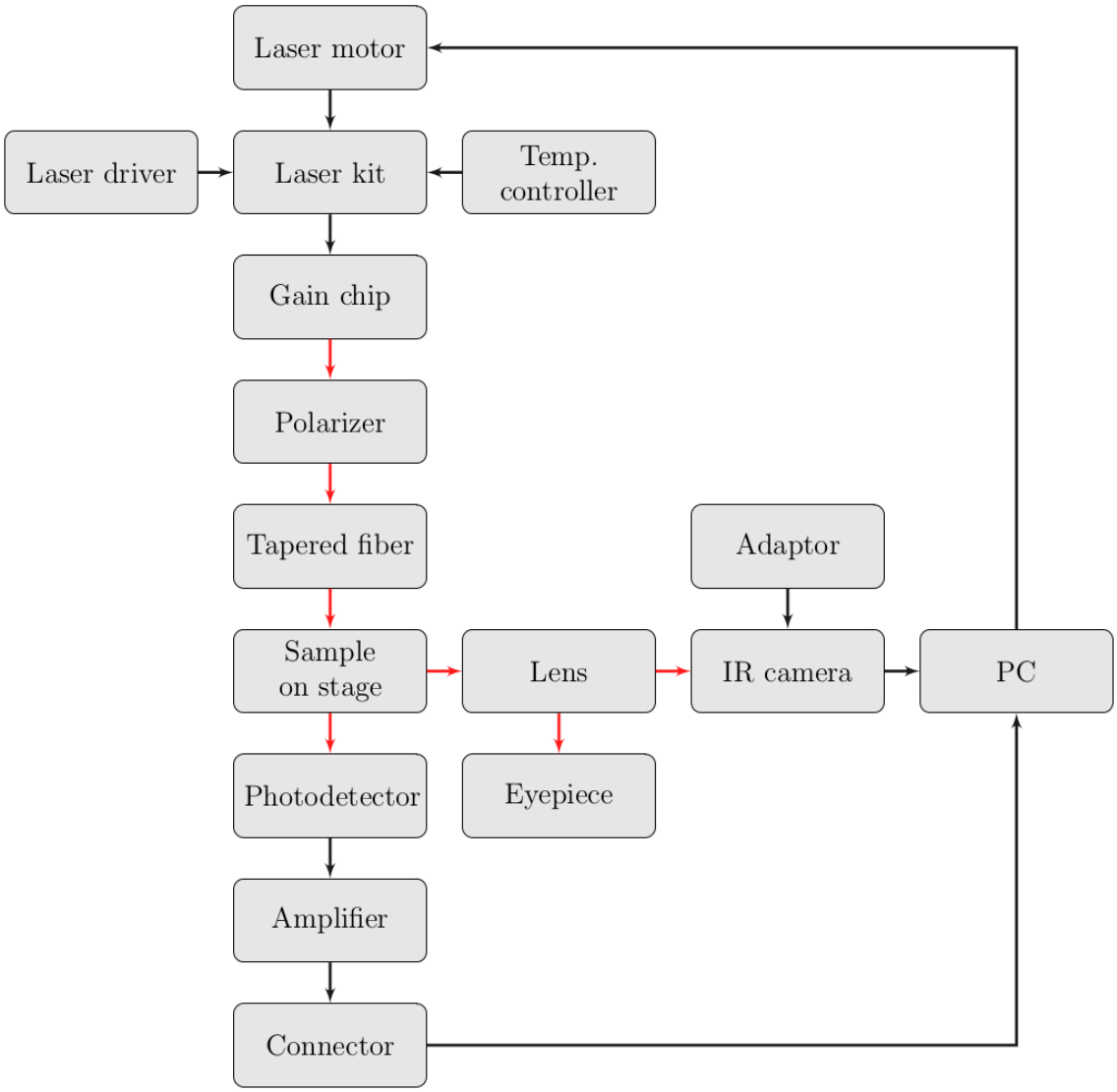

Figure 3.3: Flowchart describing the optical characterization setup. Red arrows symbolize light, while the black arrows symbolize the flow of everything else, for instance electric current.

detailed description, to clarify the challenges and uncertainties associated with this setup and the following results.

Figure 3.3 illustrates the many devices used in this setup and how they all were connected, while Table 3.4 lists the manufacturers and models. A computer controlled the output wavelength of the laser via a laser motor, thereby allowing for wavelength scans. The laser was also connected to a laser driver, which supplied it with current, and a temperature controller. The gain chip consisted of both the chip itself and a fiber, and this fiber was then connected to a fiber polarizer, which removed the TM polarized light from the fiber. The remaining TE polarized light then entered a single-mode tapered fiber, which, as the name implies, had a decreasing radius towards the end, making it capable of outputting a very thin ray of light. The tapered fiber was fastened onto the XYZ stage for better control, along with the sample and the output fiber. The sample was positioned such that

Component	Manufacturer and model
Camera adaptor	Sony DC-700
Connector	National Instruments CB-68LP
Eyepiece	Leitz Weizlar Periplan GW 8x M
Fiber polarizer	Thorlabs
IR camera	Hamamatsu InGaAs camera C14041-10U
IR photodetector	InGaAs PIN diode
Laser diode driver	Newport Model 505
Laser motor	Thorlabs apt-dc servo controller TDC001
Objective lenses	Olympus MPlan 5x, LMPlan N 10x, SLMPlan 20x
Photodiode amplifier	Thorlabs PDA200C
Mounted Single-Angled-Facet Gain Chip	Thorlabs SAF1550P2
Single-mode tapered fiber	Nanonics Imaging
Temperature controller	Newport Model 325
Tunable laser kit	Thorlabs TLK-L1550M
XYZ stage	Elliot Scientific Ltd. MDE881

Table 3.4: Manufacturer and model for the equipment used in the optical characterization setup. Unfortunately, the models were unknown for some of the components.

the cross section with the silicon tapers was facing towards the tapered fiber. The combination of tapering significantly simplified the process of coupling light into the fabricated silicon waveguide. However, a large fraction of the light was still lost.

The output fiber was not tapered, and was aligned such that a large fraction of the output light was capable of entering it. The light was then led towards a photodetector, and converted into an electrical signal. The signal was then amplified and led to the computer via a connector. By the help of the right software, this signal was interpreted, and could be used to create a transmission spectra. However, because of the varying losses in the coupling between the fibers and the sample, the intensities given in these spectra would always be more or less arbitrary. It was therefore not possible to compare the intensities between different waveguide designs in an exact manner.

A microscope was used to aid in the alignment of fibers and sample. While the eyepiece was used to only approximately align the fibers with the sample before turning on the laser, the IR camera was used to see the flow of light when the laser was on. If the coupling was done correctly, the strip silicon waveguides would light up slightly in the image, along with larger spots of light where the photonic crystals, the end of the strip waveguides and the tapered fiber tip were positioned. It was important to use this camera during alignment to ensure that the in-coupling was done correctly. Otherwise, a false positive could be given by light passing either above the sample or as plane waves through the silicon surrounding the waveguides.

The transmission data from the optical characterization could also become misleading in other ways. First of all, it was observed that large variations in the output power of the laser would occur sometimes. Some of this could be explained by the wavelength dependence of the laser power [42], but not all, since they would

sometimes occur when the laser wavelength was constant. Luckily, these fluctuations appeared rather smoothly, creating mostly linear decreases or increases in amplitude in the transmission data. They could therefore be easily spotted, and the scans could be retaken.

The second misleading result arose from whether or not the sample was scanned with increasing or decreasing wavelength. It is unclear what caused the mismatch in results between the scanning directions, but it could be quite significant. It was therefore essential to keep the scan direction constant for transmission graphs that were to be compared.

Chapter 4

Experimental procedure

A research result is useless if it cannot be reproduced, however fantastic it might be. The main focus of this chapter is therefore to convey the experiments in as much detail as necessary, as well as to explain why the experiments were needed in the first place. They will be categorized into three sections. First, the simulations will be addressed. Then the work done to ease the transition from the numerical to the practical approach will be considered. This will include both optimizations and simple validations of the physical properties of the fabricated devices. The third section will revolve around the creation of a functioning drop filter, as well as a small biosensing experiment. However, it is first necessary to justify the choice of parameters made during the project. The chapter will therefore start off by listing and explaining a few design guidelines. It will also repeat the main findings of my project thesis, as it formed the basis of all the other work performed here.

4.1 Design guidelines

The goal of this master thesis was to simulate and fabricate a photonic crystal drop filter for use in biosensing, similar to the one shown in Figure 2.7. Several limitations and requirements were given for the design, some of which have already been mentioned:

- The PhC should be periodic in two dimensions, as this greatly simplifies the fabrication compared to a 3D PhC.
- As shown in subsection 2.1.5, there are two types of photonic crystal slabs, namely rod slabs and hole slabs. While both in theory are suited for making drop filters, the rod slab is significantly more challenging to fabricate. It is simply quite difficult to make a lattice of tall, thin and homogeneous rods, while also keeping the structure stable. The hole slab was therefore chosen instead.
- It would be an advantage if the material of choice was compatible with the already available CMOS fabrication equipment, as this would significantly ease the transition from research to application. The structure was therefore fabricated using a silicon-on-insulator (SOI) structure.

- The drop filter must be designed in a way that allows for multiplexing of several different devices along one input waveguide.
- While it would be tempting to do several shifts to the lattice as seen in [43, 44], this poses a quite significant challenge when trying to combine several drop filters into one large, multiplexing device. For instance, by changing the width of a photonic crystal waveguide, it becomes a lot harder to combine this waveguide with a bend at a later point. It is therefore important to keep the integrity of the photonic crystal lattice. The only exception might be to permanently change the lattice constant as seen in [20, 45], as this can prove quite useful when designing a multiplexing device. It is also fine to displace only a couple of holes, as this will not break the integrity of the crystal as a whole.
- The drop filter should have a high sensitivity to changes in the surrounding refractive index, so as to lower the minimum change in concentration that can be measured.
- The resonance cavity should be designed in such a way as to obtain resonances with a high quality factor. This factor is a measure of the loss of the resonator and thus the sharpness of the resonance peak. A sharp peak generally increases the sensitivity of the device by making it easier to accurately pinpoint the frequency of the resonance. In general, losses to the substrate and the surrounding air are higher for higher frequencies due to the nature of the light line, and a low-frequency resonance mode is therefore preferred.
- Subsection 2.1.5 explained how the presence of a substrate under the PhC hole slab would significantly decrease the quality factor of the structure. It would therefore seem necessary to etch away the oxide under the drop filter, thereby making what is called an air-bridge structure. Etching of SiO_2 is usually performed using hydrofluoric (HF) acid due to its very high selectivity towards silicon [46, 47]. Unfortunately, HF is an extremely dangerous acid that requires strict safety precautions [48], and it would not be justifiable to use the chemical for such a short project. In addition, the etch parameters would have to be optimized, and this could quickly become quite time-demanding. The substrate was therefore not removed during the project.
- A certain minimum of light at the resonance frequencies ought to be dropped to the output waveguide to ensure that the resonance peaks can be detected over the noise in the system. Since the noise depends upon the optical setup, this minimum cannot be easily determined, but a few percent should be enough. Several simple steps can be, and were taken to ensure this for all drop filter designs. First of all, the reflectance at the interface between the strip waveguide and the PhC waveguide were limited by ensuring that the hole closest to the interface was split in half [1, 3, 4, 49]. Secondly, the drop waveguide was given only one exit instead of two [1].
- There should be a certain spectral distance between the different resonance peaks to avoid interference effects.

- When bends are included in the structure, it is essential that they are designed to support the modes that are to pass through them. For instance, if the PhC drop waveguide makes a bend, it is essential that the bend supports the resonance modes that should be emitted, or else the light will be reflected back into the crystal. Since the frequency of the resonance mode might vary slightly upon changing the surrounding medium or due to small imperfections in the fabrication, it is important that the bend has a sufficiently wide mode to support all the variations of the resonance. While this adds an extra design precaution, it allows for the bend to become an extra filter that removes unwanted frequencies from the drop spectra.

4.2 Earlier work

This project is in many ways a continuation of my project thesis, which revolved around optimizing a PhC drop filter using Meep and MPB in two and three dimensions [1]. Several aspect and parameters were considered, and the following list summarizes the main results:

- **The hole radius r:** An increase in radius caused the PBG center frequency and the PBG width to increase as well [18, 50]. While 2D simulations also indicated an increase in the quality factor, 3D simulations instead favored a medium sized radius.

- **The cavity length l:** An increase in the cavity length made the mode density grow. The resonances also became less localized, and 3D simulations indicated a small increase in the quality factor as a consequence [6, 19]. An increase in the sensitivity of the device was also expected [19], but this was not tested.

- **The separation d between the cavity and the waveguides:** A large separation caused the amplitude of the resonance peaks to become smaller, especially for strongly localized modes at the center of the band gap. If the separation was very short, light would couple directly between the two waveguides, and the quality factor of the resonances would decrease.

- **The horizontal displacement of the two holes closest to the cavity along the x-axis:** As the distance between the cavity center and the holes increased, so did the quality factor [51]. Meanwhile, the resonance frequency decreased.

- **The strip/PhC waveguide interface:** By letting the two holes closest to the waveguides be split in half by the end of the PhC, the reflectance at the interface was lowered [3, 4, 49].

- **The left output from the drop waveguide:** By removing the left exit the amplitude of the resonance peaks was approximately doubled, and a small increase in the quality factor was observed.

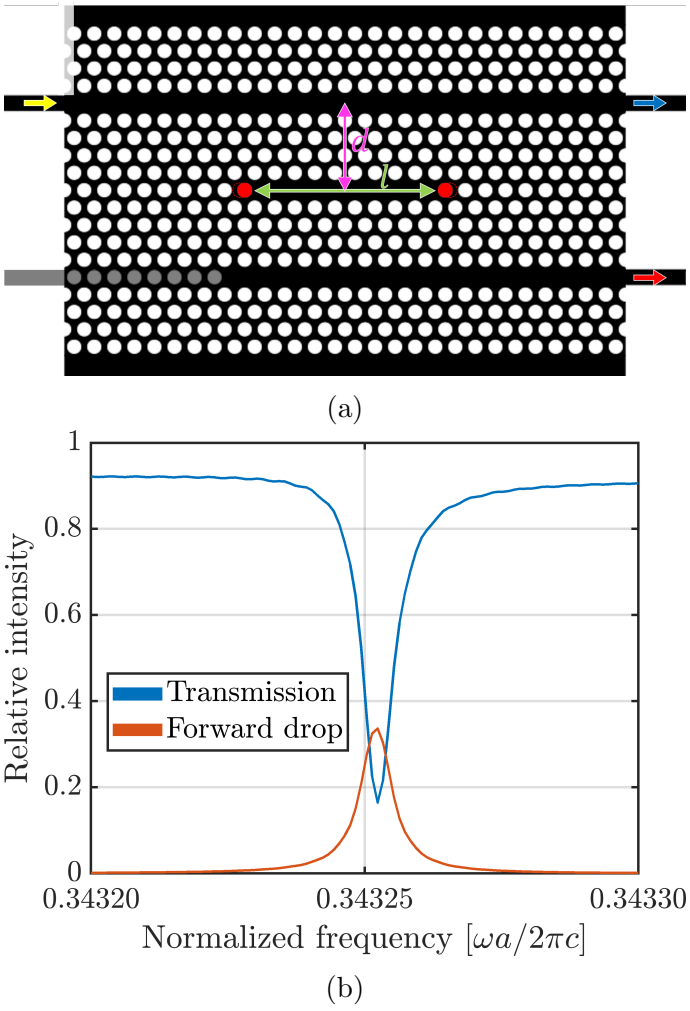

Figure 4.1: (a) The drop filter simulated during my project and master thesis. The x and y axes are defined to be in-plane, with the x axis parallel to the waveguides. The black area represents silicon, while the white areas are air. The lattice constant a is defined as the center-to-center distance between two neighboring holes, while $A = \sqrt{3}a/2$ is the distance between two neighboring rows. The different parameters tweaked during the project thesis are labeled. The hole radius is described by the parameter r. The green arrow represents the length l of the cavity, which in this case is given as $l = 9a$. The pink arrow represents the waveguide-to-cavity distance $d = 5A$. The filled red circles highlight the holes that were displaced by a given fraction of a, as shown by the dashed red circles. In the upper left, a part of the crystal has been grayed out to show how removing half a lattice constant on each side of the crystal could change the strip/photonic crystal interface. In the row that belongs to the lower waveguide, a series of holes has been given a slightly darker color and a rectangle of the same color has been added. This has been done to visualize that the drop waveguide can have either one or two exits, the latter causing the structure to be symmetric around both the x and the y axes. The input, transmitted and dropped light are symbolized by yellow, blue and red arrows, respectively. (b) The best result from my earlier work, measured in quality factor and dropped intensity [1]. Notice how the resonance frequency is measured in normalized units, to make the result easily transferable between structures of different lattice constants a. The intensity is given relative to the amount that enters the PhC.

The different optimization parameters are visualized in Figure 4.1, along with the best result obtained throughout my simulations. This result was obtained using a 2D simulation with a hole radius $r = 0.339a$, a cavity length $l = 9a$, a waveguide-to-cavity distance $d = 5A$ and an effective refractive index $n_{\text{Si,eff}} = 2.87$ for the silicon [1]. The holes had a refractive index $n_{\text{air}} = 1$ during all the simulations performed in the project and the master thesis, unless otherwise stated. The structure had no backward drop channel, and had a split hole at the strip/photonic crystal waveguide interface to limit its reflectance. Also, the holes closest to the cavity following the x-axis were displaced by $0.25a$ away from the center of the resonator, and the strip waveguides had a width $\omega = 0.82a$. The result was a dropped resonance peak with an intensity above 30 % and a quality factor of 59 000 according to the Harminv simulations. The parameters used in this simulation formed the basis for all choices of parameters taken during the master thesis. However, since these parameters belong to a 2D simulation, some adjustments were made before doing any 3D simulations or fabrications.

4.3 Simulation

4.3.1 Multiplexing

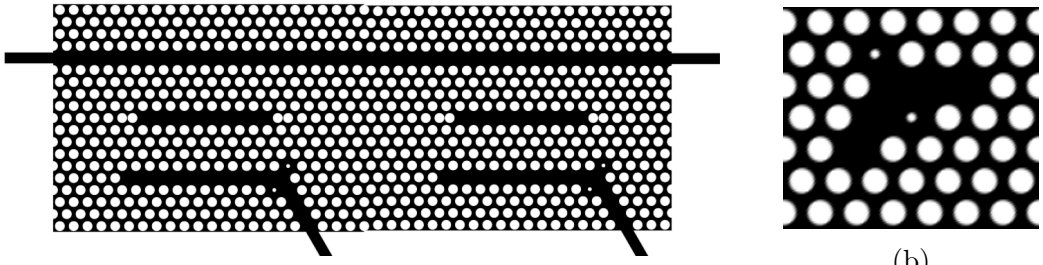

(a) (b)

Figure 4.2: (a) The multiplexing simulation geometry. Notice how the right half is identical to the left except for its lattice constant $a_2 = a_1/c$. Here, $a_1 = 1$ is the lattice constant for the left half, and c is the lattice constant ratio. The PhC drop waveguides have been made with a bend to separate the signals and clarify the source of each resonance during the optimization. However, the bends are also capable of filtering out unwanted drop peaks if designed and tuned correctly. Here, this has been done by giving the holes closest to the bends a radius $r_{\text{bend}} < r$. (b) An example of a 2D MPB simulation cell used to find the optimal bend radius r_{bend}.

The final lab-on-a-chip device should be capable of sensing several different substances at once using the same light source and detector for maximum efficiency and simplicity. A way of solving this is to place two or more PhC drop filters with different capture agents in series, so that the transmitted light from the first filter becomes the input light for the second, and so on. The different filters are given a slightly different lattice constant a, and therefore also a slightly different set of parameters, as seen in Figure 4.2(a). This will cause the resonance spectra of the filters

to be shifted slightly relative to each other [20], thereby avoiding any interference effects.

To investigate the possibility of multiplexing, Meep simulations of two such adjoined filters were run. By adding 60° bends to the PhC drop waveguides, the light was led to two separate detectors, which helped determine the source of each resonance during the simulations. However, if a bend is formed by simply positioning two waveguides with a 60° rotation relative to each other, the result will be a severe discontinuity in the waveguide, and it will introduce large reflections and excite higher order modes that might not be guided by the waveguides [52, 53]. Many alternative bend designs have been proposed. Their procedures include fusing some of the holes close to the bend [52], changing their hole radii [20], displacing them [54], adding extra holes inside the bend [53, 55] or deforming the lattice in and around the bend [56]. While creating bends that can support the resonance modes certainly adds to the work load, if tuned correctly they can also work as a second filter that removes noise from the output signal. It might therefore be unfortunate to remove them later on to join the two drop channels together for detection. An alternative could be to keep the bends and join the channels together at the strip waveguides.

The simulation parameters were chosen based on the result shown in section 4.2, and included a hole radius $r = 0.339a$, a waveguide-to-cavity distance $d = 5A$, a defect length $l = 9a$, a strip waveguide width $\omega = 0.82a$ and a hole displacement of $0.25a$ for the holes closest to the cavity along the x-axis. The lattice constant ratio $c = a_1/a_2 = 1.012$ was chosen based on the value used in [20]. The simulations were run in 2D, with an effective refractive index $n_{\text{Si,eff}} = 2.87$ for the silicon. Since the transmission spectra for these parameters had been found earlier, as shown in section 4.2, the best resonance had already been localized at a normalized frequency of 0.3433. A Harminv simulation of the frequency range of interest, which was set to be from 0.335 to 0.355, could therefore be done immediately to determine the quality factors and exact frequencies of the two resonances.

The bends were optimized using the hole radii approach, which meant that the two holes closest to the bends were given a radius $r_{\text{bend}} \neq r$ [20]. Different values of r_{bend} were tested in MPB using the simulation cell shown in Figure 4.2(b). Finally, a second and third Meep simulation were run to obtain the transmission spectra for the frequency range of interest. One of them used the optimized value for r_{bend}, while the other had $r_{\text{bend}} = r$, similar to the Harminv simulation. This was done to ascertain the results from the optimization, and to find the intensities of the resonance peaks. The Harminv simulations were run for 1000 Meep time units, while the transmission simulation was run until the drop output from the left side had been reduced below 1×10^{-4} of its maximum output.

4.3.2 Thickness optimization

The thickness of the PhC hole slab can strongly affect the properties of the final product. For instance, a decrease of the slab thickness will cause the bands to become less guided, thus increasing the loss of the system. On the other hand, an increase in the slab thickness can allow for higher order modes to occupy the band gap [6]. Additionally, to fulfill the single-mode condition, the height and width of a

silicon waveguide must be in the order of 300 to 400 nm [37]. If either the width or the height should be larger than this, the single-mode condition can only be met by making the other parameter smaller. Usually, the slab has a thickness of 220 nm, allowing for a maximum waveguide width of 520 nm.

In this section, several different values of the slab thickness h will be simulated, both to confirm the effects described above, and to help find the optimal choice of slab thickness relative to the lattice constant. All simulations were run in 3D, and the silicon slab ($n_{\text{Si}} = 3.48$) had air ($n_{\text{air}} = 1$) above and inside the crystal, and oxide ($n_{\text{oxide}} = 1.44$) below it. A hole radius $r = 0.3a$, a cavity length $l = 9a$, a strip waveguide width $\omega = 0.82a$ and a waveguide-to-cavity distance $d = 3A$ were used. Additionally, the holes closest to the cavity on both sides were displaced away from the crystal center by $0.25a$. Notice how the hole radius has been decreased relative to the radius used during the 2D simulations, as shown in section 4.2 and subsection 4.3.1. This is done to limit the light loss to the surrounding air, since a decreasing r causes a lowering of the center frequency of the band gap, and therefore a decrease in the overlap between the band gap and the light cone [1, 50], see Figure 5.9(b). Notice also the decrease in the waveguide-to-cavity distance d. This was deemed necessary to increase the amplitude of the resonance peaks, which decreased significantly when going from 2D to 3D simulations due to the increased loss to the surrounding medium.

4.3.3 Biosensing

The entire motivation behind making a drop filter is to use it for biosensing. The project would therefore not be complete without simulating such a sensing process. To do that, the capture agents and target molecules described in section 2.4 were modeled as a homogeneous layer with refractive index $n_{\text{bio}} = 1.45$. This biolayer was then given the same thickness t both on the hole walls and on top of the photonic crystal. The bottom of the holes were not covered due to practical reasons, but according to [14] this would not have a serious impact on the final result due to a limited sensitivity there. The rest of the holes and the area above the PhC were modeled as water, with $n_{\text{water}} = 1.32$ at [57, 58], as illustrated in Figure 4.3. All simulations were carried out in 3D, with a slab thickness of $0.8a$ and a supporting oxide layer. A hole radius $r = 0.3a$, a cavity length $l = 9a$ and a waveguide-to-cavity distance $d = 3A$ were used. Additionally, the holes closest to the cavity on both sides following the horizontal were displaced away from the crystal center by $0.25a$. Four transmission simulations were performed. First a ordinary simulation with neither water nor a biolayer, and then three simulations with $t = 0, 0.2r, 0.4r$, respectively. The simulations were then repeated using Harminv to obtain more exact values for the resonances and the quality factors and to confirm the results.

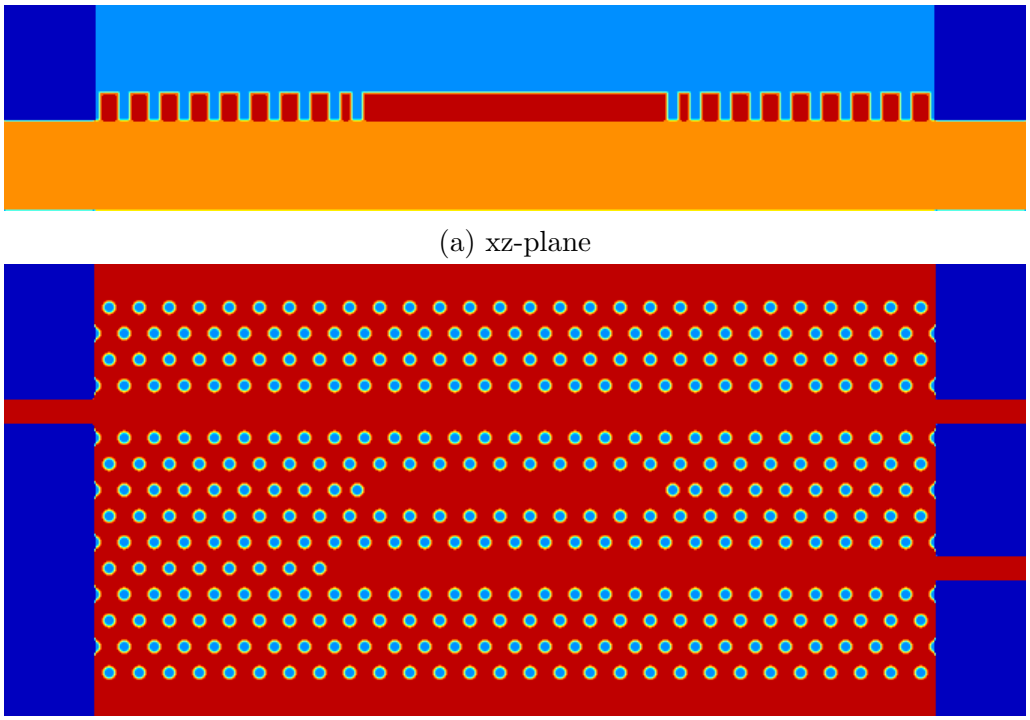

(a) xz-plane

(b) xy-plane

Figure 4.3: The simulation space used during a biosensing simulation, with $t = 0.4r$. Each color represents a certain refractive index: Dark blue for air ($n_{\text{air}} = 1$), light blue for water ($n_{\text{water}} = 1.32$), orange for oxide and bio ($n_{\text{oxide}} = 1.44$ and $n_{\text{bio}} = 1.45$), and red for silicon ($n_{\text{Si}} = 3.48$). The cross sections were taken through origo, which by definition is at the center of the silicon slab.

4.4 Transition to fabrication

4.4.1 Silicon film thickness

Before starting to fabricate the photonic crystals, it is important to determine the actual thickness h of the deposited silicon thin films, and ascertain that the etch time is long enough for the structures to be etched all the way through. Since high aspect ratio structures, such as the holes in a photonic crystal, suffer from a limited flow of both etching ions and etch by-products, the etch rate will become slower in the holes relative to the waveguides [33, 59]. Therefore, when testing if the etch time is sufficient, it might give a false positive to do the etching on a flat, resist-free surface. Instead, the silicon surface should be covered with a layer of resist patterned with holes similar to those used when making photonic crystals. The type of resist and its thickness should also be similar.

The difference in etching rates also means that the low aspect ratio structures, such as the waveguide margins, might become over-etched relative to the holes. Luckily, according to [2] the ICP-RIE etching selectivity of silicon towards SiO_2 and CSAR62 e-beam resist is 5.1:1 and 2.4:1, respectively, when etching on a flat surface. This means that the resist and the underlying oxide layer will etch quite slowly relative to the silicon. Since the resist layer has a thickness of approximately

475 nm, the consequences of etching a bit too much are marginal for these materials. However, the notching effect, which refers to how charging of the insulator layer may cause undercutting of the silicon, becomes worse when over-etching, making it important to etch for as short a time as possible [60].

In this section two samples will be made. Both are SOI samples with an etched hexagonal pattern of holes with lattice constant $a = 400\,\text{nm}$ and a mask design radius $r = 0.26a$. The only difference is the growth and etch times. The goal is to make one sample with $h = 220\,\text{nm}$, which is the standard thickness for photonic crystals, and another sample with $h = 400\,\text{nm}$. The latter sample thickness was chosen based on the results from subsection 5.1.2. Since the lattice constants used in the project ranged from 400 to 500 nm, a 400 nm thick silicon slab would give a relative thickness between $h = 0.8a$ and $h = 1.0a$.

Target thickness [nm]	Growth time [s]	Etch time [s]
220	150	45
400	273	82

Table 4.1: The choices of growth and etch times used to achieve two different film thicknesses.

Suitable growth and etch times for a 220 nm thick silicon thin film were found in [4] and are listed in Table 4.1. The times for a 400 nm thick Si layer was found by assuming that the growth and etch rates are constant as a function of time, i.e. by using the formula $t_{400} = 400t_{220}/220$. After fabrication, the samples were scribed across the hexagonal hole pattern, and the cross sections were imaged using SEM.

4.4.2 Resist cracking

Figure 4.4 demonstrates the consequences of cracks in the resist, as experienced for all samples at the beginning of the project. The cracks were generally concentrated around abrupt changes in the resist pattern, for instance at the beginning and end of the waveguides, and in the photonic crystals. Sometimes, the cracks would tear through the crystal, thereby breaking the symmetry. Figure 4.4 shows how the resist belonging to the crystal could move up to 1 to 2 µm relative to the rest of the resist, causing the corresponding strip waveguides to bend or simply snap off the crystal. Since it affected nearly all the PhCs on a sample, it was necessary to solve the problem before proceeding.

Seeing that the cracks were concentrated around the resist structures, it was clear that they arose after the exposure. At first, it was considered likely that the development process was the source of the error. The sample was moved more gently through the developer, and the nitrogen blow drying was done with more care. However, neither of these efforts had any success, ruling out the development process as a likely main cause. It followed that something must have been wrong with the resist before the exposure, for instance an underlying tension in the resist or a low adhesion to the substrate. According to [33], the soft bake is performed partly to relieve stresses in the resist and to increase the adhesion. It therefore

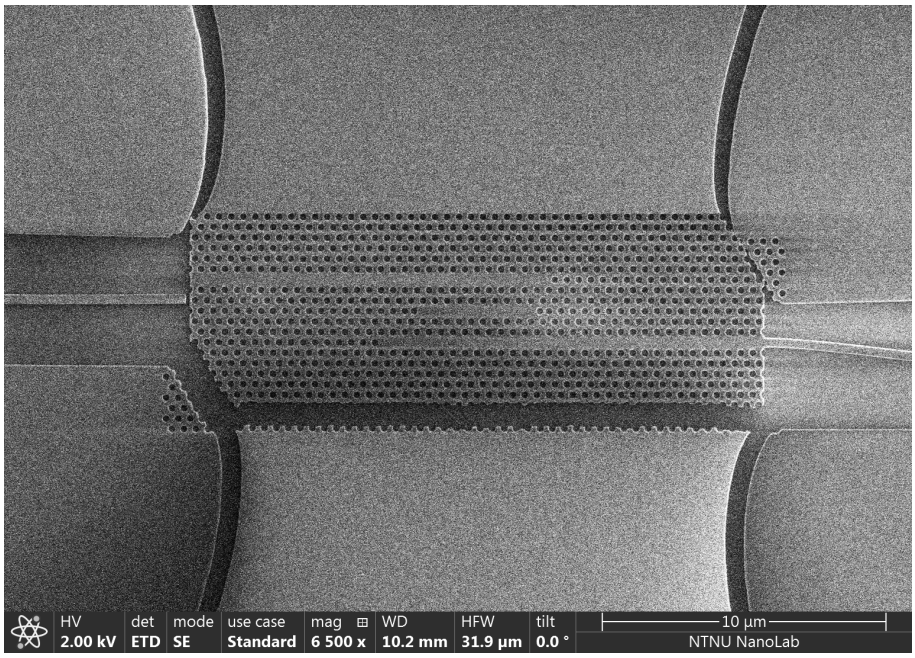

Figure 4.4: SEM image of a broken PhC due to a cracked resist. The sample was etched and stripped before imaging. However, the cracks were big enough that they could be seen by an optical microscope during the develop inspect.

seemed likely that an inadequate soft bake might be the source of the tension and the subsequent crack formation.

During the optimization of the soft bake, several parameters were considered. Along with time and temperature, the abrupt change in temperature experienced for the resist when moving on and off the hot plate, were examined. Other parameters involved in the processing, such as exposure and development, were held constant. The samples were etched and stripped for resist before a final imaging in SEM. To ensure optimal image quality, all of the 3 samples which were made used a simple silicon substrate for better imaging quality. The exposure pattern was designed to imitate the earlier exposures, having both ordinary waveguides and several different photonic crystals.

Sample 1: The first sample used the original soft bake method, where the sample was put on an old silicon wafer lying on a hot plate holding 150 °C for 1 min, before the sample was allowed to cool down on a cold metal slab. The temperature and time was chosen based on the information given in the resist data sheet [61]. Due to the simple standard of the equipment it seems likely that the hot plate temperature was not at any point constant, but instead was oscillating around the assigned value.

Sample 2: It was considered likely that bad contact between sample and wafer carrier, and carrier and hot plate, would cause the resist to reach a much lower temperature than the one measured on the hot plate. To avoid this, a brand new silicon wafer was used as a carrier and the hot plate temperature was increased until a laser thermometer found the resist to hold the assigned 150 °C. This was done for Sample 3 as well. The sample was also allowed to stay on the hotplate for a total of 3 min instead of 1 min. Notice that while several parameters were changed relative

to Sample 1, neither affected the total fabrication time or cost in any significant way.

Sample 3: The sample was put on top of the carrier and a hot plate holding 40 °C. Next, the hot plate temperature was ramped up to 100 °C, then 120 °C, 140 °C, 150 °C, 160 °C and finally 165 °C. At maximum temperature, the resist temperature was measured to be 150 °C, as needed. After every ramping step, the hot plate was allowed to stay there for a total of 30 s, except for the last one, which lasted for 3 min. Next, the hot plate was allowed to cool down to 100 °C, a slow and time consuming process due to the hot plate's lack of a built-in cooling mechanism. Finally, the sample was moved to the metal block.

4.4.3 Band gap position

It might seem strange that after so many simulations, there could still be doubts regarding the position of the PBG belonging to the fabricated photonic crystal. However, two important factors cause this to remain an issue. First of all, while the refractive index of amorphous silicon can be assumed to be quite close to the refractive index of crystalline silicon, it might still be different enough to affect the position of the band gap in the wavelength spectra. Secondly, the proximity effect native to the EBL causes the exposed regions to become slightly larger than planned according to the mask files. Since a positive e-beam resist was used throughout this project, that implied that the radius of the air holes would become too big, while the width of the strip waveguides would become too thin. Considering the hole radius, this enlargement could be in the scale of 10 to 30 nm, which is quite significant when the holes were supposed to have a radius of 120 to 150 nm. Of course, this can be solved somewhat by designing the holes smaller than needed, but a small deviation is still unavoidable. Therefore, since both the hole radius and the refractive index affects the properties of the band gap [1, 6], it can be hard to know exactly where to find it. This can actually become a problem, especially when trying to find a resonance peak, since the wavelength range of the light source used in the optical characterization is much smaller than the band gap.

The goal of this section was to find the difference between the hole radius r given by the mask and the final fabricated hole, as well as to estimate the refractive index n_{Si} for PECVD-grown a-Si. This would grant valuable knowledge for future comparison between simulations and fabrications. The procedure was split into three parts:

- **Band gap as a function of r and n_{Si}:** To illustrate the effect small variations in the hole radius and refractive index can have on the position of the band gap, two MPB simulations were run. For both of them, one variable was slowly varied while the other parameter was held constant at the ideal values $n_{\mathrm{Si},0} = 3.48$ and $r_0 = 0.3a$, respectively. The simulations were performed in 3D without an oxide layer and with a slab thickness of $h = 0.45$. Only the TE-like band gap was considered.

- **Fabricated PhC waveguides:** Next, two photonic crystal waveguides were fabricated with lattice constants $a = 430$ nm and $a = 480$ nm, respectively. To

account for the deviation in hole radius, 30 nm were subtracted from the target radius, giving a mask radius $r = 0.3a - 30\,\text{nm}$. Likewise, 40 nm was added to the strip waveguide width, giving a total mask width of $w = 0.82a + 40\,\text{nm}$. The PhC waveguides were made by simply removing a row of holes, and the crystal had 90 periods in the x-direction and 6.5 in the y-direction. The silicon thin film was grown and etched using $t_{\text{growth}} = 150\,\text{s}$ and $t_{\text{etch}} = 45\,\text{s}$. After fabrication, the waveguides were imaged using SEM, and the hole radius and strip waveguide width for both values of the lattice constant were found.

- **Simulated PhC waveguides and a comparison:** Using the measured values of r and w together with the slab width $h \approx 200\,\text{nm}$ found in subsection 5.2.1, the fabricated structures were replicated in MEEP, and simulated. By comparing the band gaps obtained in these simulations to the ones observed when coupling light into the fabricated waveguides, a simple estimate of the refractive index n_{Si} for PECVD-grown a-Si could be found.

4.5 Fabrication and characterization

4.5.1 Drop filter

With the help of the design optimizations in section 4.3 and the fabrication optimizations in section 4.4, a satisfactory sample was finally made containing 6 identical sets of drop filters. Each set consisted of 6 almost identical photonic crystal drop filters, except for the lattice constants being 400, 420, 440, 460, 480 and 500 nm, respectively. All of the drop filters were designed with the same relative hole radius $r = 0.26a$, strip waveguide width $\omega = 1.02a$, waveguide-to-cavity distance $d = 3A$, defect length $l = 9a$ and hole displacement of $0.25a$. The drop filters were made using the SOI system, with a silicon thin film growth time of 273 s and an etch time of 82 s. This resulted in a PhC slab thickness h of approximately 330 nm, as shown in subsection 5.2.1. The photonic crystals consisted of 48 and 9.5 periods in the x- and y-direction, respectively, and were connected with silicon strip waveguides at all outputs, as shown in Figure 4.5. The waveguides were made by removing 2 µm of silicon on both sides, and were connected to tapers at the input side of the sample. Each strip waveguide was $3\,\mu\text{m} - 24a$ long, and the total length of each integrated circuit was 6.6 mm. This gave a total taper length of 600 µm, but only 500 µm of these were actually tapered. The remaining 100 µm were positioned at the far left of the taper, as a buffer when scribing the sample. The taper core had a width ranging from 5 µm to $\omega = 1.02a$, and 8 µm of silicon was removed on both sides of the taper to create a margin towards the rest of the silicon. Since the drop filter had two quite closely spaced outputs, and since the output fiber had an inner core of several micrometers, it was necessary to create an S-shaped bend on the strip output waveguide for the transmitted light to avoid the signal from one output interfering with the other one.

Since the integrated waveguides made from the 330 nm thick silicon layer had proved delicate in the past, the resist could not be removed after etching by simply placing the sample in a beaker of resist remover and doing an ultrasonic bath for

(a) Taper

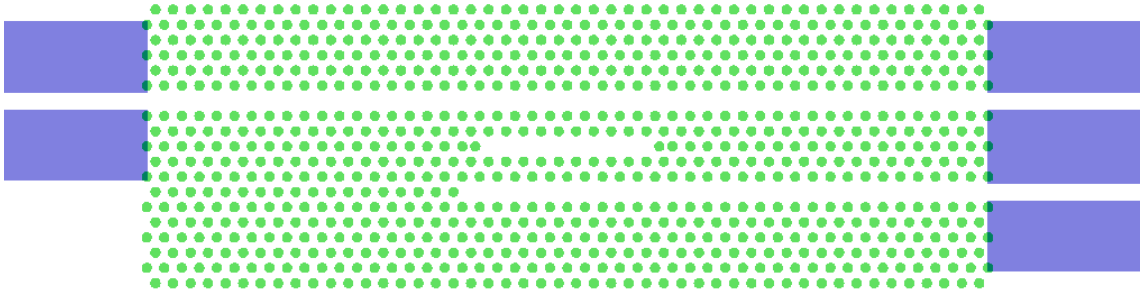

(b) PhC

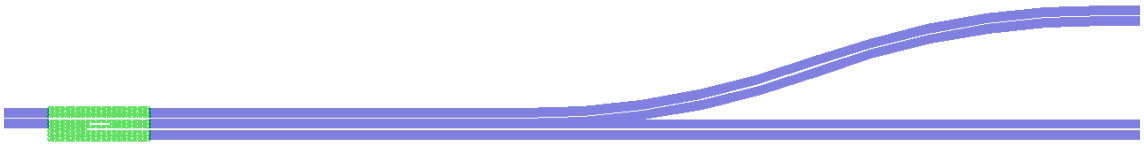

(c) Bend

Figure 4.5: CleWin drawings of the different parts of the integrated photonic circuit, with $a = 500\,\text{nm}$. The colored areas were exposed to the electron beam, and removed first from the resist, then from the silicon through etching. The colors represents the different file layers, and are irrelevant except for clarifying the interface between the different components. The three figures have different dimensions, but the x- and y-axis of the individual figures have been scaled proportionally. Light will enter the structures from the left-hand side, and the figures are listed in the sequential order of their position along the waveguide. Note that the low resolution seen in the figures is merely due to the qualities of the screenshot, and is not an indication of the actual resolution provided by the software.

5 min. Instead, the resist was removed first by putting the sample in a beaker of resist remover for 5 min, then rinsing it with IPA and allowing it to air dry, before the sample was finally plasma cleaned for 3 min using 50 % oxygen and 50 % power. The sample was also allowed to air dry after the development, instead of using nitrogen.

4.5.2 Biosensing

A simple way of testing the sensitivity of a biosensor is to deposit a drop of liquid on top of the sample, for instance water or ethanol, and then measuring the amount of light dropped to the drop waveguide as a function of the laser wavelength. As the refractive index of the liquid increases, so does the resonance wavelength, as seen in subsection 5.1.3. The decrease in contrast between the silicon and surrounding media will also give a smaller band gap, as explained in subsection 2.1.3, and it is likely to cause a decrease in the transmission, as seen for parts of the band gap in subsection 5.1.3.

While the goal of this section was to simply deposit a small drop of water on top of

the sample described in subsection 4.5.1, the extra cleaning steps performed before the biosensing experiment turned out to be a biosensing experiment themselves. First, the sample, which had not been cleaned since the resist removal and the subsequent scribing, was rinsed with IPA and allowed to air dry in the cleanroom. This was done to remove scribing dust that might affect the biosensing experiment. When measurements were performed on the sample afterwards, strange observations were made. It was thought that this could be caused by the lack of a plasma cleaning after the rinse, which had been performed during the resist removal. The sample was therefore cleaned again using IPA, air-dried and then plasma cleaned using 50 % oxygen and 50 % power. Light was then coupled through the sample and measurements were taken for all values of a.

The final biosensing experiment was performed using Milli-Q water, which is a brand of ultrapure water of Type 1 [62]. A syringe was used to deposit a small drop of this water on top of the sample such that it covered the PhC and parts of the strip waveguides. The silicon surface was quite hydrophilic after the recent plasma cleaning, and the layer of water became fairly thin as a result. However, subsection 5.1.3 demonstrated how the sensitivity of the light decreases quite rapidly as a function of the distance from the sample surface, and the thin layer of water was therefore considered quite sufficient. The sample was characterized as before.

Chapter 5

Results and discussion

This section focuses on presenting and explaining the final results found during the master's project. While the simulation and fabrication parameters were both visualized and given in more detail in the previous chapter, they will be quickly repeated along with each result to make it easier to read. The two chapters have been given the same sectioning to better clarify the correlation.

5.1 Simulation

5.1.1 Multiplexing

Cavity	Quality factor	Normalized resonance frequency
Single	58 854	0.3433
Left	62 753	0.3431
Right	55 501	0.3475

TABLE 5.1: The top entry shows the result obtained earlier, as presented in section 4.2, while the two other entries list the results from the Harminv simulations performed here. The Harminv simulations were run with hole radius $r = 0.339a$, bend hole radius $r_{\text{bend}} = r$, waveguide-to-cavity distance $d = 5A$, defect length $l = 9a$, lattice constant ratio $c = 1.012$ and a hole displacement of $0.25a$ for the holes closest to the cavity along the x-axis. The simulations were run in 2D, with an effective refractive index $n_{\text{Si,eff}} = 2.87$.

Table 5.1 presents the results from the Harminv simulation. Notice how the smaller lattice constant for the right half of the PhC causes its resonance to occur at a higher frequency, in agreement with the results found in [20]. This difference in a will also cause an increase in the spacing between the resonances of the right half relative to the left half. This means that the distance between the resonances belonging to the two halves will increase for increasing frequencies.

Notice also the small difference in resonance frequencies between the single and left cavity. Since they have the same lattice constant, it would seem likely that these two cavities would possess the same resonance frequency. However, it is possible that the surroundings of the left cavity, such as the right cavity, the interface between

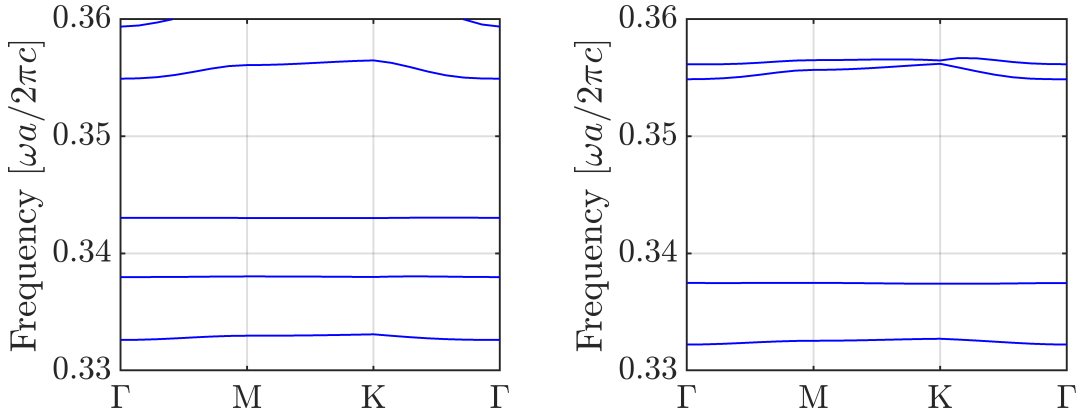

(a) $r_{\text{bend}} = 0.122a$ (b) $r_{\text{bend}} = r = 0.339a$

Figure 5.1: Optical modes for two 60° bends, as shown in Figure 4.2(b). Both results were obtained using a 2D MPB simulation, with a hole radius $r = 0.339a$ and an effective refractive index $n_{\text{Si,eff}} = 2.87$ for the silicon.

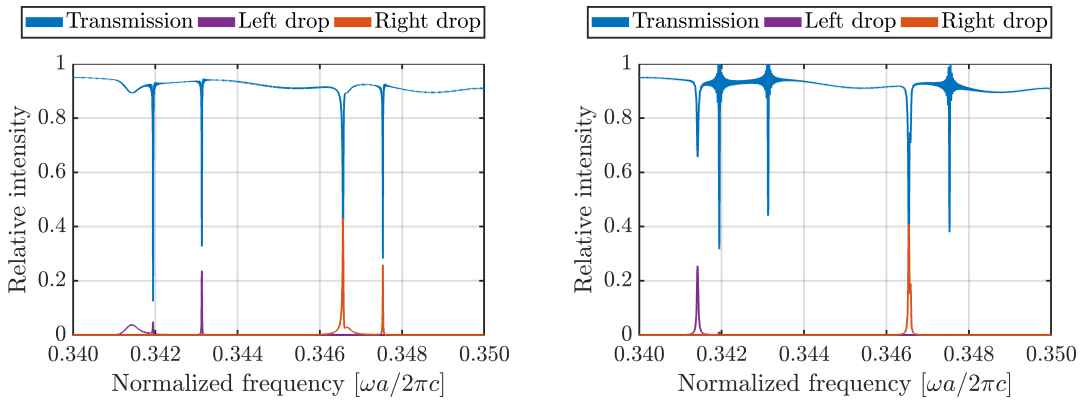

(a) $r_{\text{bend}} = 0.122a$ (b) $r_{\text{bend}} = r = 0.339a$

Figure 5.2: The transmission spectra of a double drop filter, as illustrated in Figure 4.2(a). Both simulations were run with hole radius $r = 0.339a$, waveguide-to-cavity distance $d = 5A$, defect length $l = 9a$, lattice constant ratio $c = 1.012$ and a hole displacement of $0.25a$ for the holes closest to the cavity along the x-axis. The simulations were run in 2D, with an effective refractive index $n_{\text{Si,eff}} = 2.87$.

the two values of a and the bend would affect the resonance frequency slightly. If so, they should also affect the quality factors, as confirmed by Table 5.1.

According to Table 5.1, the left bend must have a mode at 0.3431 to support the resonance. Figure 5.1 presents the TE modes belonging to two bends with different values for r_{bend}. When $r_{\text{bend}} = r$, there are no modes present close to the frequency of interest, and there is an obvious need for bend optimization. Luckily, a useful result was found for $r_{\text{bend}} = 0.122a$. By zooming in on the bands shown in Figure 5.1(a), it can be seen that a mode exists for normalized frequencies in the range of 0.3430 to 0.3431. To test the effect of the bend optimization, two transmission simulations were run, yielding the results shown in Figure 5.2.

Several important differences can be spotted between the two plots. First of all, while the decrease in transmission typical for a resonance can by clearly seen for both

plots at 0.3431 and 0.3475, no increase in either drop channel is visible when $r_{\text{bend}} = r$. Instead, two other large drop peaks are shown to the left of these frequencies, both with intensities of much more than 20 %. According to [1], these are not resonances, but standing waves surrounding the cavity, and their presence is unfortunate, as it can cause interference effects. Luckily, the result was much better for $r_{\text{bend}} = 0.122a$. The most important improvement is of course the fact that both resonances can be clearly seen as increases in the dropped light. According to graph analysis, and with the aid of Equation 2.1.19, it was concluded that the left peak has a quality factor of 27 600 and an intensity of 23.7 %, while the right peak has a quality factor of 26 900 and an intensity of 25.9 %. The intensities are therefore impeccable, and it is clear that the bend was the source of the disappearing drop peaks for $r_{\text{bend}} = r$. Also, while the quality factors observed here are significantly lower than indicated by the Harminv simulation, it is likely that both that and the intensity could have been improved by simply increasing the duration of the simulation. Another improvement when using $r_{\text{bend}} = 0.122a$ is the significant decrease in intensity for the non-resonant drop peak with center frequency of 0.3414, which seems to indicate that the bends are indeed working as second filters.

While the choice of r_{bend} in many ways can be seen as a success, there is room for several improvements. First of all, the bend mode is very narrow. While this can be an advantage, considering how the resonance is closely surrounded by other drop peaks that should be filtered out, it still makes the filter vulnerable for fabrication errors. A small deviation in the fabricated hole radius, for example, can significantly change the resonance frequency, which might make it incompatible with the bend. Also, it is likely that the bend mode and the resonance will have a different sensitivity, and they might therefore become incompatible when the surrounding medium is changed. Secondly, a large drop peak still remains at the normalized frequency of 0.3466. Hopefully, these problems might be solved by performing further optimizations of r_{bend}, or by choosing an alternative bend design entirely [52–56]. However, the results presented here are all obtained using 2D simulations, and are likely to deviate significantly from 3D simulations and the properties of fabricated filters. This section should therefore be understood more like a proof of concept than anything else, and further 2D optimizations are therefore meaningless. Instead, the optimizations should be performed in 3D and then verified through fabrication to achieve optimal results. Unfortunately, there was not enough time to achieve that during the master's thesis.

5.1.2 Thickness optimization

Figure 5.3 presents the transmission spectra obtained for 6 different values of the silicon thin film thickness h. First of all, notice how the normalized midgap frequency decreases for increasing thicknesses. This was also reported in [63], where it was considered a result of a decreasing photon momentum in the z direction. Since the overlap between the light cone and the band gap becomes smaller as the midgap frequency decreases, it would seem likely that a thicker slab would have a higher transmission and a better quality factor. This theory is supported by the increase in transmission seen both when going from $h = 0.4a$ to $h = 0.6a$, and from $h = 0.6a$

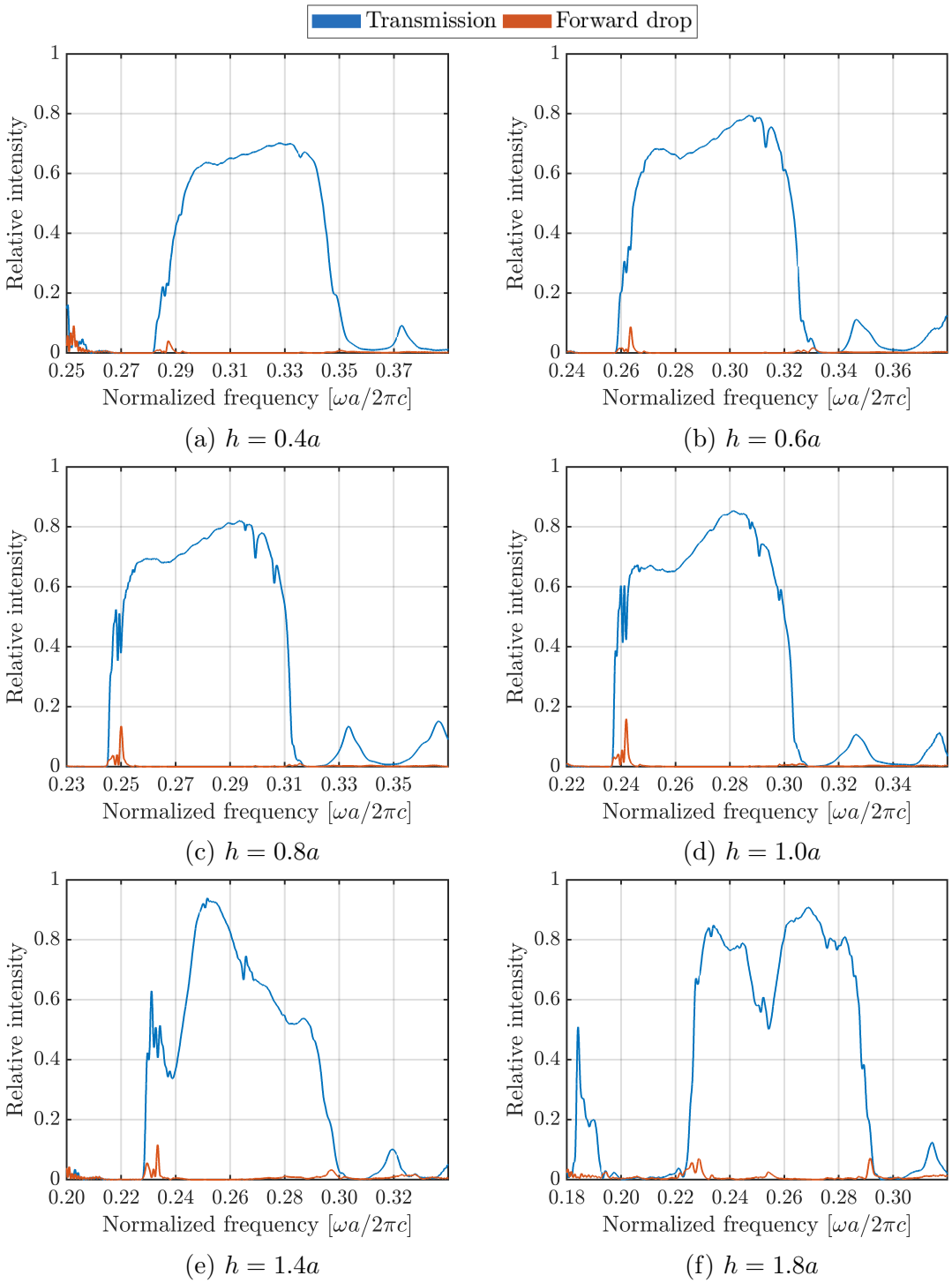

(a) $h = 0.4a$ (b) $h = 0.6a$

(c) $h = 0.8a$ (d) $h = 1.0a$

(e) $h = 1.4a$ (f) $h = 1.8a$

Figure 5.3: Transmission spectra for 6 different slab thicknesses. Notice that the frequency scales change from one graph to the next. The simulations were run in 3D with hole radius $r = 0.30a$, waveguide-to-cavity distance $d = 3A$, defect length $l = 9a$ and a hole displacement of $0.25a$ for the holes closest to the cavity along the x-axis. The slab was positioned upon a layer of silicon oxide.

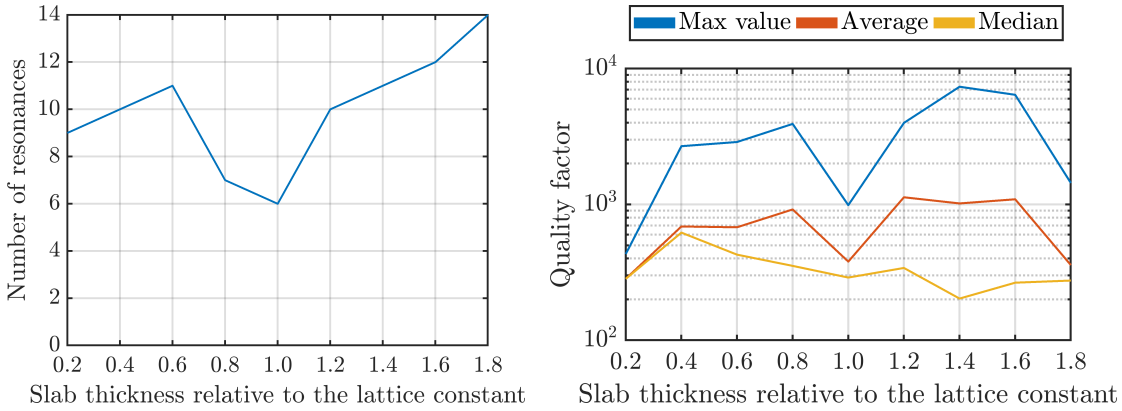

(a) Number of resonances.

(b) Quality factors.

Figure 5.4: Results from Harminv simulations with varying slab thicknesses. The simulations were run in 3D with hole radius $r = 0.30a$, waveguide-to-cavity distance $d = 3A$, defect length $l = 9a$ and a hole displacement of $0.25a$ for the holes closest to the cavity along the x-axis. The slab was positioned upon a layer of silicon oxide. The same Gaussian light source was used here as for the transmission plots, with a center frequency of $0.34 - 0.05h$ and a width of 0.14.

to $h = 0.8a$. However, no consistent increase can be seen when increasing the thickness further. Instead, the transmission increases for parts of the band gap, while it decreases for other parts. This can be explained by remembering that, as mentioned in subsection 4.3.2, a very thick layer of silicon will allow for higher order modes to populate the band gap, thereby lowering the transmission at certain parts of the PBG [6]. This is supported by Figure 5.4(a), which demonstrates a small increase in the number of modes when the slab thickness h increases. However, even though some parts of the band gap become less useful, the parts with high transmission can still be used if only a small range of frequencies are needed.

Since the results are obtained using simulations, they do not consider the entire situation. For example, as shown in [64], the surface roughness of an amorphous silicon thin film is likely to increase when the film thickness is increased beyond 100 nm. While surface roughness-induced loss is usually considered unimportant relative to other loss factors such as sidewall thickness, Zhu et al. [65] measured the propagation loss in PECVD-grown a-Si strip waveguides with a surface roughness of ∼2.58 nm to be as large as ∼5.2 dB/cm. Therefore, it seems likely that having a silicon layer as large as $1.0a$, where a is in the range of 400 to 500 nm, might give an undesirably large surface roughness-induced loss. The simulations do not consider the coupling efficiency, either. When coupling light from the tapered fiber into the tapered silicon waveguide, a lot of light is lost due to the difference in cross section between them. A thicker silicon layer will give a larger bullseye, and therefore help lower the coupling losses. This is essential when trying to detect a small resonance peak over the unavoidable noise of the system.

Another thing worth noticing when considering Figure 5.3 is the properties of the dropped resonance peaks. The most intense resonance peak can be observed in Figure 5.3(d), with a dropped intensity of 16 % and a quality factor of 229 at a normalized frequency of 0.242. The maximum resonance intensity then steadily

decreases both for increasing and decreasing thicknesses. The maximum quality factor belonging to any peak positioned inside the PBG and with an amplitude above 2 % is achieved for $h = 1.4a$, but is still no larger than 243. This is very low compared to the quality factor of 59 000 achieved earlier, as shown in section 4.2. However, there are several plausible explanations for this. First of all, this is a 3D simulation, where the slab is positioned on top of a silicon oxide layer, while the other was a 2D simulation. Since 3D cavities experience all the same in-plane losses as those seen for 2D cavities, while also having losses to air and the oxide below the crystal slab, it is no wonder that the quality factor becomes significantly smaller. The oxide layer is also responsible for breaking the $z = 0$ reflection symmetry. Since the structure of the drop filter itself ensures that the reflection symmetry is broken in the x- and y-direction, coupling between the TE- and TM-like modes will occur, as explained in subsection 2.1.5. Knowing that the TE- and TM-like modes often have different band gaps, it seems likely that this will increase the in-plane losses. Additionally, having a waveguide-to-cavity distance of only $d = 3A$ will both help increase the drop intensity and the cavity loss. Even so, according to the Harminv simulations, as seen in Figure 5.4(b), a maximum quality factor as large as 7367 should be achievable for $h = 1.4a$. This is unfortunately not confirmed by the transmission plots. A high quality factor is sometimes an indication that the resonance has a limited ability to couple to the waveguides, and the dropped intensity will therefore be extremely low. It is however possible that the intensity would increase if the simulation was prolonged.

To sum it up, it is clear that the silicon slab thickness should not be much larger than $1.0a$, since that would give a PhC with both a large amount of surface roughness-induced loss, as well as a PBG populated by higher order modes. However, it should not be much smaller either, since that would increase the coupling loss between the fibers and the waveguide, and decrease the intensity of the resonance peaks.

5.1.3 Biosensing

Figure 5.5 presents the results from the biosensing transmission simulation. The difference between the surrounding media is most easily seen in the graph of the transmitted light, especially between air and the other media. This is as expected, since moving from air to water gives a much larger refractive index change than moving from water to water/bio. It is clear that both the band gap width and the transmission is larger when the silicon slab is surrounded by air. The former is due to a larger refractive index contrast, which results in an increase in the PBG width [6], see Figure 2.1. The latter might be understood by considering the extremes: while a quite high transmission can be achieved when the surrounding medium has a small refractive index, such as air, only a very small transmission can be achieved if the surrounding media is made up of silicon. Then nothing would confine the light inside the slab, and a large amount of it would leak out into the surroundings and be lost to the perfectly matched layer.

The transmission for the dropped light is presented in Figure 5.5(b), and quantified for the rightmost resonances in Table 5.2. The results indicate a significant

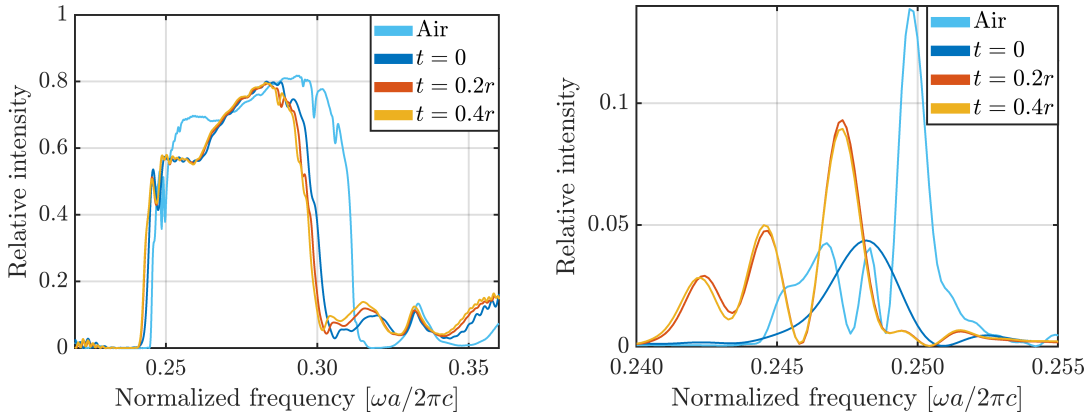

(a) Transmitted (b) Dropped

Figure 5.5: Transmission and drop output as a function of frequency. All four graphs belong to the same SOI drop filter, with hole radius $r = 0.3a$, cavity length $l = 9a$, a displacement of $0.25a$, waveguide-to-cavity distance $d = 3A$ and slab thickness $h = 0.8a$. The difference lies in the medium surrounding the 3D structures. Except for the air case, where both PhC and strip waveguides were surrounded by air, all drop filters were covered in a biolayer of thickness t both inside the holes and on top of the photonic crystal. The rest of the holes and the area above the PhC were covered in water. The refractive indexes used are as follows: $n_{\text{air}} = 1$, $n_{\text{water}} = 1.32$, $n_{\text{oxide}} = 1.44$, $n_{\text{bio}} = 1.45$ and $n_{\text{Si}} = 3.48$.

resonance shift both when going from air to $t = 0$, and from $t = 0$ to $t = 0.2r$. In normalized frequencies, these shifts are 1.51×10^{-3} and 1.28×10^{-3}, where the latter equals a sensitivity $S = \Delta\lambda/\Delta t = -0.348$ if one assumes a linear relationship, as was approximately the case in [14]. This paper obtained a calculated sensitivity $S = \Delta\lambda/\Delta t \approx -1.5$, which is more than 4 times the sensitivity obtained here, for their one-hole defect. Therefore, while the simulations performed here indicate that the sensor design indeed is working, it is not state of the art.

When going from $t = 0.2r$ to $t = 0.4r$, the resonance shift is only 3×10^{-5} according to Table 5.2. This seems to indicate that the relationship is nonlinear, in contrast to the assumptions made above and the results found in [14]. It also indicates that the sensitivity might be significantly higher than calculated above

Medium	Normalized frequency	Quality factor
Air	0.249 81	268
$t = 0$	0.248 30	280
$t = 0.2r$	0.247 02	260
$t = 0.4r$	0.246 99	272

Table 5.2: Changes in quality factors and normalized frequencies for a single resonance upon changing the medium inside the holes and above the PhC. All results are obtained using a 3D Harminv simulation, with hole radius $r = 0.3a$, cavity length $l = 9a$, a displacement of $0.25a$, waveguide-to-cavity distance $d = 3A$ and slab thickness $h = 0.8a$. The refractive indexes used are as follows: $n_{\text{air}} = 1$, $n_{\text{water}} = 1.32$, $n_{\text{oxide}} = 1.44$, $n_{\text{bio}} = 1.45$ and $n_{\text{Si}} = 3.48$.

for the first few nanometers of biolayer. Finally, it indicates that the field density decreases quite quickly outside of the silicon, making the filter rather insensitive to changes in the refractive index happening more than $0.2r = 0.06a$ away from the silicon surface. Successful efforts to increase the sensitivity of optical biosensors include using an extra target molecule with a high refractive index contrast that binds to the original target molecule [66]. It might prove a challenge to combine such a method with a biosensor whose sensitivity decreases quickly as a function of the distance from the silicon surface. It would be interesting to simulate the drop filter using more values of t to get a more detailed understanding of the relationship between the biolayer thickness and the redshift. Unfortunately, a very small biolayer thickness requires a very high resolution if the results are to be reliable [1], and an increase in resolution will inevitable prolong the simulations. The redshift as a function of t for very thin biolayers can therefore not be found without an upgrade of the computational hardware, or by swapping Meep with a simulation software that permits highly non-uniform resolutions.

Notice the large variation between the intensities of the different resonance peaks seen in Figure 5.5(b). While a lowering of the intensity is as expected when increasing the refractive index of the surrounding medium, as explained above, the decrease in intensity is surprisingly large for $t = 0$. Fortunately, it is quite possible that this is simply a consequence of a limited simulation time, as explained in subsection 3.1.1, and that much of the light is still trapped inside the PhC. This explanation is supported by the large drop in transmission at the resonance frequency for $t = 0$, which is at almost 15 %.

5.2 Transition to fabrication

5.2.1 Silicon film thickness

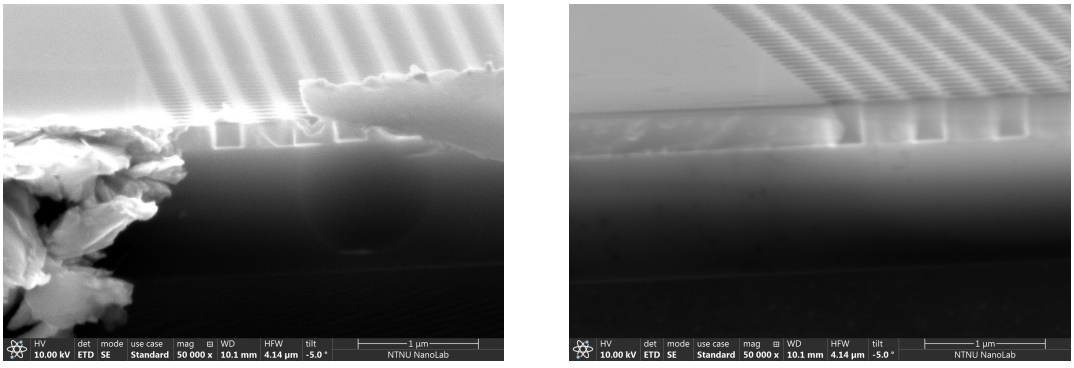

(a) $t_{\text{growth}} = 150\,\text{s}$ and $t_{\text{etch}} = 45\,\text{s}$ (b) $t_{\text{growth}} = 273\,\text{s}$ and $t_{\text{etch}} = 82\,\text{s}$

Figure 5.6: SEM images of the cross section of two SOI photonic crystals with different silicon thin film growth and etch times.

The cross section of two samples with different growth and etch times are shown in Figure 5.6. While both images seem to indicate that the films were etched all the way through, the target thickness was not obtained for either. Instead, Figure 5.6(a)

shows a film with $h \approx 200\,\text{nm}$, while the film shown in Figure 5.6(b) has a thickness $h \approx 330\,\text{nm}$. The deviation is clearly much larger for the thicker film, which seems to indicate that the growth rate varies as a function of time. However, the deviations were not large enough to require an optimization of the silicon growth and etch times, and the times used here were deemed adequate for future drop filters.

An alternative explanation is based on the fact that the deposition at the center and edge of a sample happen at different rates [67], an effect which can be clearly seen by observing the difference in color on a PECVD deposited silicon film. The change in film thickness is at its largest at the edge of the sample. Since the 220 nm sample was cut from the edge of a wafer after deposition, and the 400 nm sample was cut before deposition, both would experience some variations in the film thickness. It is therefore possible that the cross sections shown in Figure 5.6 are unrepresentative for the samples as a whole.

5.2.2 Resist cracking

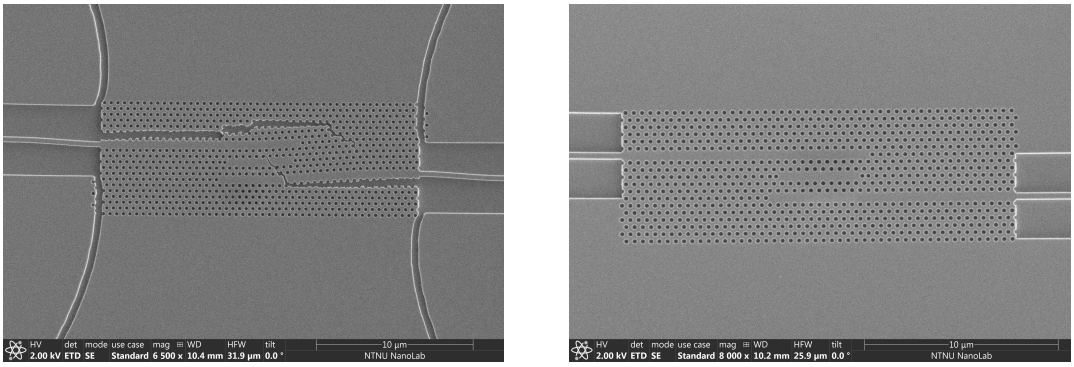

(a) (b)

Figure 5.7: SEM images showing the improvement obtained by optimizing the soft bake for a CSAR 62 resist on top of crystalline silicon. (a) Sample 1, which was hot baked for 1 min using an old, dirty silicon wafer as carrier at a hot plate temperature of 150 °C. (b) Sample 2, which was hot baked for 3 min using a new silicon wafer as carrier and a hot plate temperature of 165 °C, which, according to a laser thermometer, gave a resist temperature of 150 °C. Both samples were etched and stripped before the SEM imaging.

Figure 5.7 shows the effect of optimizing the soft bake process for a CSAR 62 resist on top of c-Si. Figure 5.7(a) presents a drop filter belonging to Sample 1, and is therefore a demonstration of the original problem. The resist is clearly cracked, and in such a manner as to strongly break the original symmetry of the crystal. Figure 5.7(b), on the other hand, shows a perfectly fracture-free photonic crystal. It belongs to Sample 2, and it was therefore unnecessary to further consider Sample 3. The soft bake procedures used on sample 2 were used throughout the rest of the project.

Both of the samples were made using a crystalline silicon wafer. These can of course not be used to make working waveguides and biosensors, and SOI samples with a top layer of a-Si were instead used for the rest of the project. It seems likely that the difference between c-Si and a-Si would affect the adhesion and material

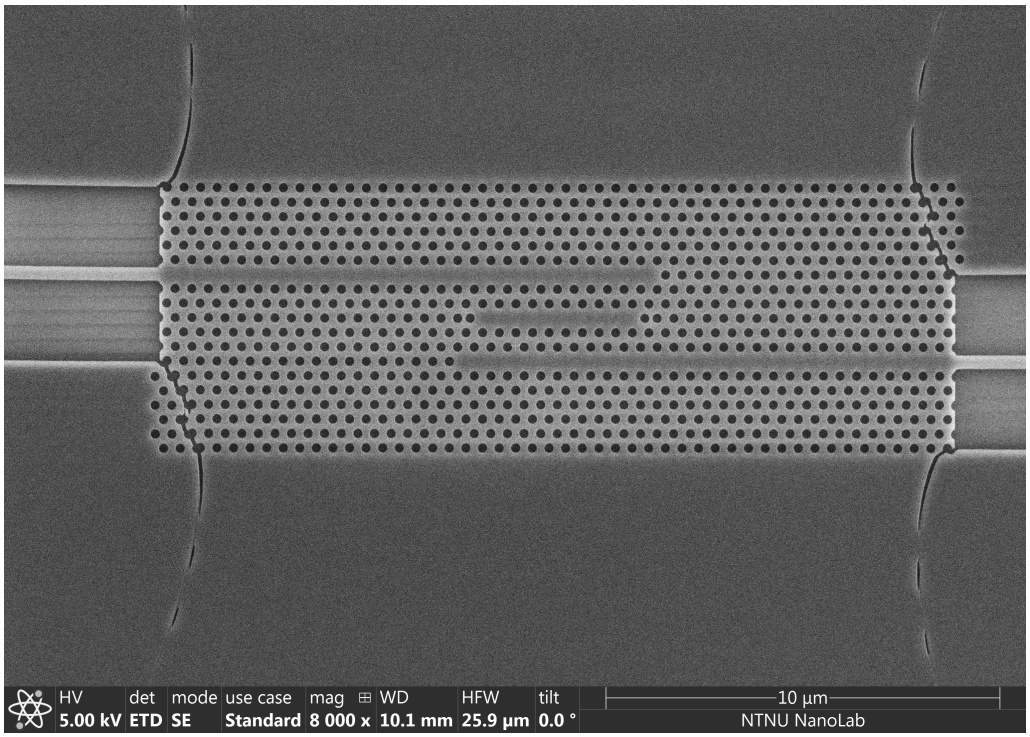

Figure 5.8: SEM image showing a drop filter belonging to an etched SOI sample. The sample was made using the same procedure as Sample 2, as shown in Figure 5.7(b), and was etched and stripped before the imaging.

tension in the resist. Therefore, when using the now optimized soft bake procedure on a SOI sample, it was interesting to image the final result in the SEM to consider the difference. This was done, and can be seen in Figure 5.8. It is clear that while the silicon is far less cracked than before, several fractures still remain. However, while the cracks in the silicon might be a result of resist cracking, it can also be a result from the ultrasonic bath used to remove the resist. The bath is likely to affect the SOI sample harder than the c-Si samples due to the much smaller adhesion between the amorphous silicon and the oxide. This is supported by Figure 5.14, which shows a SEM image of a working drop filter. Luckily, for all seven drop filters belonging to the sample shown in Figure 5.8, the cracks seemed to propagate away from the photonic crystals, and they therefore affected only the less sensitive areas of the filters. The images indicated that the sharp corners associated with the rectangular waveguide cladding was the source of the cracks. It therefore seems likely that the cracks could be avoided entirely by rounding off the corners slightly.

5.2.3 Band gap position

The goal of this section was to find the difference between the hole radius r given by the mask and the final fabricated hole, as well as to estimate the refractive index n_{Si} of PECVD-grown a-Si. The procedure was split into three parts.

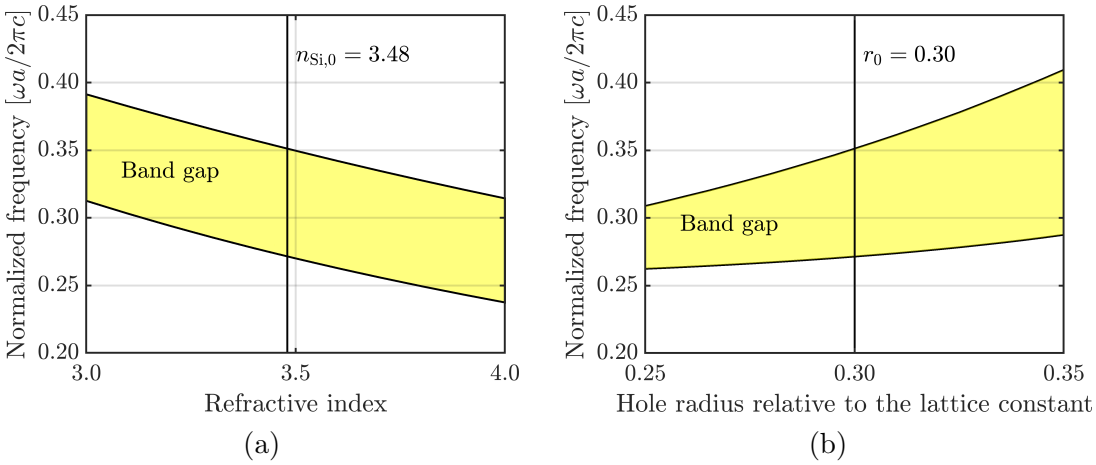

Figure 5.9: The figure illustrates how small deviations might affect the position of the band gap. The results were found using 3D MPB simulations without oxide and with $h = 0.45$. (a) used a constant hole radius $r_0 = 0.3a$, while (b) used a constant refractive index $n_{\mathrm{Si},0} = 3.48$.

Band gap as a function of r and n_{Si}

As explained in subsection 4.4.3, both r and n_{Si} may vary when moving from simulations to fabrication. This happens because the proximity effect ensures that the hole radius always becomes somewhat larger than designed, and because the exact value of n_{Si} for amorphous silicon is unknown. Figure 5.9 demonstrates that the position of the band gap changes quite a lot as a function of both n_{Si} and r, while the width of the band gap is seemingly only changing as a function of r. The latter result has wide support in literature, where it has been shown that the width of the PBG has a maxima at $r_{\max}$. However, the exact value of $r_{\max}$ depends upon the refractive index contrast between the materials composing the PhC [18, 50].

The band gap width is often described by the unitless gap-midgap ratio $\Delta\omega/\omega_m$, where ω_m is the frequency in the middle of the PBG. Since ω_m is clearly changing as a function of the refractive index n_{Si} while $\Delta\omega$ stays more or less constant, the gap-midgap ratio increases. The gap-midgap ratio also increases as a function of r, but in this case the relationship is more linear. The large changes in the properties of the PBG presented in Figure 5.9 support the assumption that the position of the band gap indeed can be hard to determine.

It is worth pointing out that the results presented in Figure 5.9 were found without the use of an oxide substrate. Since the refractive index of silicon oxide is somewhat larger than the refractive index of air, the result of removing the oxide is a small decrease in the effective refractive index. According to Figure 5.9(a), this will cause an increase in the midgap frequency. It is however unlikely that this increase will be very significant, since the effective refractive index is mostly determined by the silicon slab, see subsection 3.1.3.

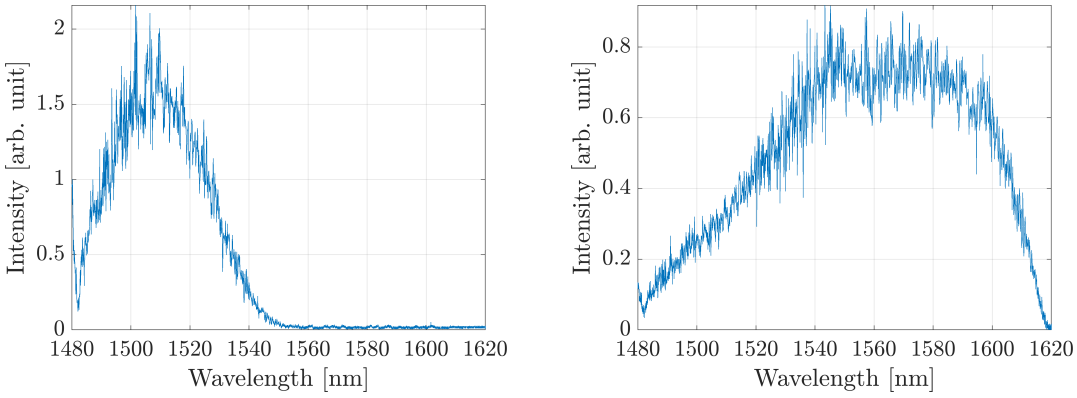

(a) $a = 430\,\text{nm}$ (b) $a = 480\,\text{nm}$

Figure 5.10: Transmission spectra for two PhC waveguides, with different lattice constants a. The intensity is given in arbitrary units and should not be compared. Both were designed with a hole radius of $r = 0.3a - 30\,\text{nm}$ and a strip waveguide width of $w = 0.82a - 40\,\text{nm}$. The slab had a thickness of $\sim$200 nm. The PhC waveguides were made by simply removing a row of holes, and the PhCs had 90 periods in the x-direction and 6.5 in the y-direction.

Method	a [nm]	Lower band gap edge	Upper band gap edge
MPB	-	0.272	0.351
Experimental	430	0.277	-
Experimental	480	-	-
Meep	430	0.269	0.315
Meep	480	0.280	0.332

Table 5.3: A list of the band gaps obtained by the different methods used in this section, as indicated by Figure 5.9, Figure 5.10 and Figure 5.11. The band gap edges are given in normalized frequency units, and the MPB band gap is given for $r = r_0 = 0.3a$ and $n_{\text{Si}} = n_{\text{Si},0} = 3.48$.

Fabricated PhC waveguides

Two PhC waveguides were fabricated with lattice constants $a = 430\,\text{nm}$ and $a = 480\,\text{nm}$, respectively, and their transmission spectra can be seen in Figure 5.10. In Figure 5.10(a), a large transmission peak can be seen for wavelengths in the range of 1480 to 1550 nm, whereas for larger wavelengths the transmission is almost constant at 0 except for small fluctuations that can be attributed to background noise. This makes it likely that the band gap starts at approximately 1550 nm, which is equivalent to $\omega a/2\pi c = a/\lambda = 430/1550 \approx 0.277$ in normalized units. That is approximately 5×10^{-3} higher than indicated by the MPB simulations, as shown in Figure 5.9 and Table 5.3. Unfortunately, neither of the graphs seem to show a similar low-intensity area at the lower range of wavelengths, making it hard to determine the location of the other band gap edge.

The PhCs were imaged using SEM, and Table 5.4 lists the hole radii and strip waveguide widths found for the two waveguides, along with the mask design values

Parameter	Mask design	Target	$a = 430\,\text{nm}$	$a = 480\,\text{nm}$
r	$0.3a - 30\,\text{nm}$	$0.3a$	$113\,\text{nm} \approx 0.263a$	$132\,\text{nm} \approx 0.275a$
ω	$0.82a - 40\,\text{nm}$	$0.82a$	$312\,\text{nm} \approx 0.726a$	$387\,\text{nm} \approx 0.806a$

Table 5.4: The two columns to the right list the measured hole radii and strip waveguide widths for the two waveguides. The two other columns list the mask design and goal values for both parameters for comparison.

and the target values. According to these data, the fabricated holes had an increase in radius relative to the mask design of 14 nm and 18 nm for $a = 430\,\text{nm}$ and $a = 480\,\text{nm}$, respectively, which is equivalent to a 14 % and 16 % increase. It is evident that in the effort to compensate for the widening of the holes caused by the proximity effect, the holes were designed too small to achieve the target values. Also, it appears that the increase in the hole radius might be slightly larger for a larger value of a.

According to Figure 5.9(b), the location of the lower edge of the band gap is quite insensitive to changes in the hole radius. Also, a lowering of hole radius would give a lowering of the band gap edges, not a heightening. The deviation in radius can therefore not be the reason for the high experimental value for the lower band gap edge relative to the MPB value, as shown in Table 5.3. Instead, it seems likely that the deviation is caused by a mismatch in the values for either n_{Si} or the slab thickness h.

Simulated PhC waveguides and a comparison

Figure 5.11 presents the results from the Meep simulation. First of all, notice how small the transmission is inside the band gap. It never becomes larger than 50 %, which is very low compared to the ones found during the thickness optimizations, as shown in subsection 5.1.2. This is likely due to the difference in length for the photonic crystal waveguides, which consisted of a total of 90 periods in this simulation, compared to only 28 during the thickness simulation. The structures also differ in other, less important aspects, for instance regarding the presence of a drop channel and the number of periods in the y-direction.

Notice also the difference in the shapes of the two band gaps. The waveguide with $a = 480\,\text{nm}$ clearly has both the widest band gap and the highest maximum band gap transmission, and the band gap is centered at a higher frequency. The width and band gap position difference can be partly explained by remembering the difference in hole radius between the two simulations, and comparing those to the data shown in Figure 5.9(b). Also, since the simulations were run with a slab thickness $h = 200\,\text{nm}$, in accordance with the measurements done in Figure 5.6, this will give a relatively thinner slab for a larger value of a. Since subsection 5.1.2 illustrated how a thinner slab equals a larger band gap center frequency, this can help explain the difference between the two graphs. However, subsection 5.1.2 also demonstrated that a thinner slab equals a smaller transmission for $h \leq 0.8a$, which makes the fact that the transmission is larger for $a = 480\,\text{nm}$ surprising.

Finally, lets compare the transmission data for the experimental and the numer-

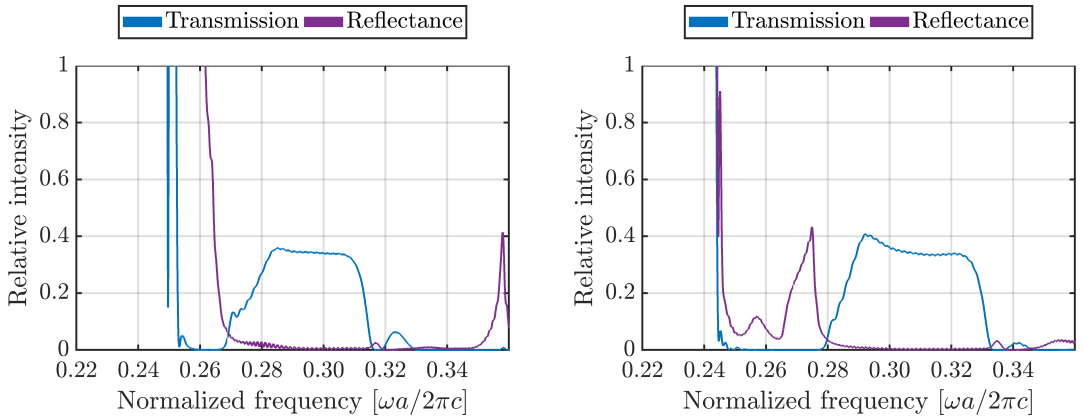

(a) $a = 430\,\text{nm}$ (b) $a = 480\,\text{nm}$

Figure 5.11: The result of two waveguide simulations performed in Meep, with different values for the lattice constant a. Both crystals were made to resemble the fabricated crystals as far as possible. This includes the number of periods, which were 90 periods in the x-direction and 6.5 in the y-direction. The values for r and ω were set according to the values found from the SEM images, i.e. $r_{430} \approx 0.26a$, $r_{480} \approx 0.28a$, $w_{430} \approx 0.73a$ and $w_{480} \approx 0.81a$. The simulations were run in 3D, with a slab thickness of 200 nm. The waveguides were made by removing the middle row of holes, and both simulations were run for a total of 900 Meep time units. According to the E-field output, this guaranteed that approximately all light had exited the simulation space before the simulations were terminated.

ical results. Table 5.3 shows how the normalized frequency of the lower band gap edge for $a = 430\,\text{nm}$ is $0.277 - 0.269 = 8 \times 10^{-3}$ lower according to Meep, than according to the experiments. There are two plausible reasons for this. First of all, even though the slab thickness was found to be 200 nm in Figure 5.6, and this value was used in the simulations, the uncertainty of the measured thickness is quite large due to limited image resolution. Even small differences in slab thickness can strongly affect the position of the band gap. There is also a similar uncertainty regarding the hole radius, but this will, according to Figure 5.9(b), not affect the lower band gap edge very much. Secondly, the refractive index used in the simulations might not be entirely correct. At $n_{\text{Si}} = 3.45$ the derivative of the lower band gap edge is approximately -0.076. If we ignore the other explanations, then the refractive index would have to be $8 \times 10^{-3}/0.076 \approx 0.11$ smaller than assumed. This yields an estimate of the refractive index of approximately $3.48 - 0.11 = 3.37$. While the estimate is probably highly inaccurate, it still gives a nice indication of what to expect in future simulations and fabrications.

5.3 Fabrication and characterization

5.3.1 Drop filter

Figure 5.12 presents the transmitted light from a drop filter for 6 different values of a and for a constant wavelength range from 1480 to 1620 nm. When the value

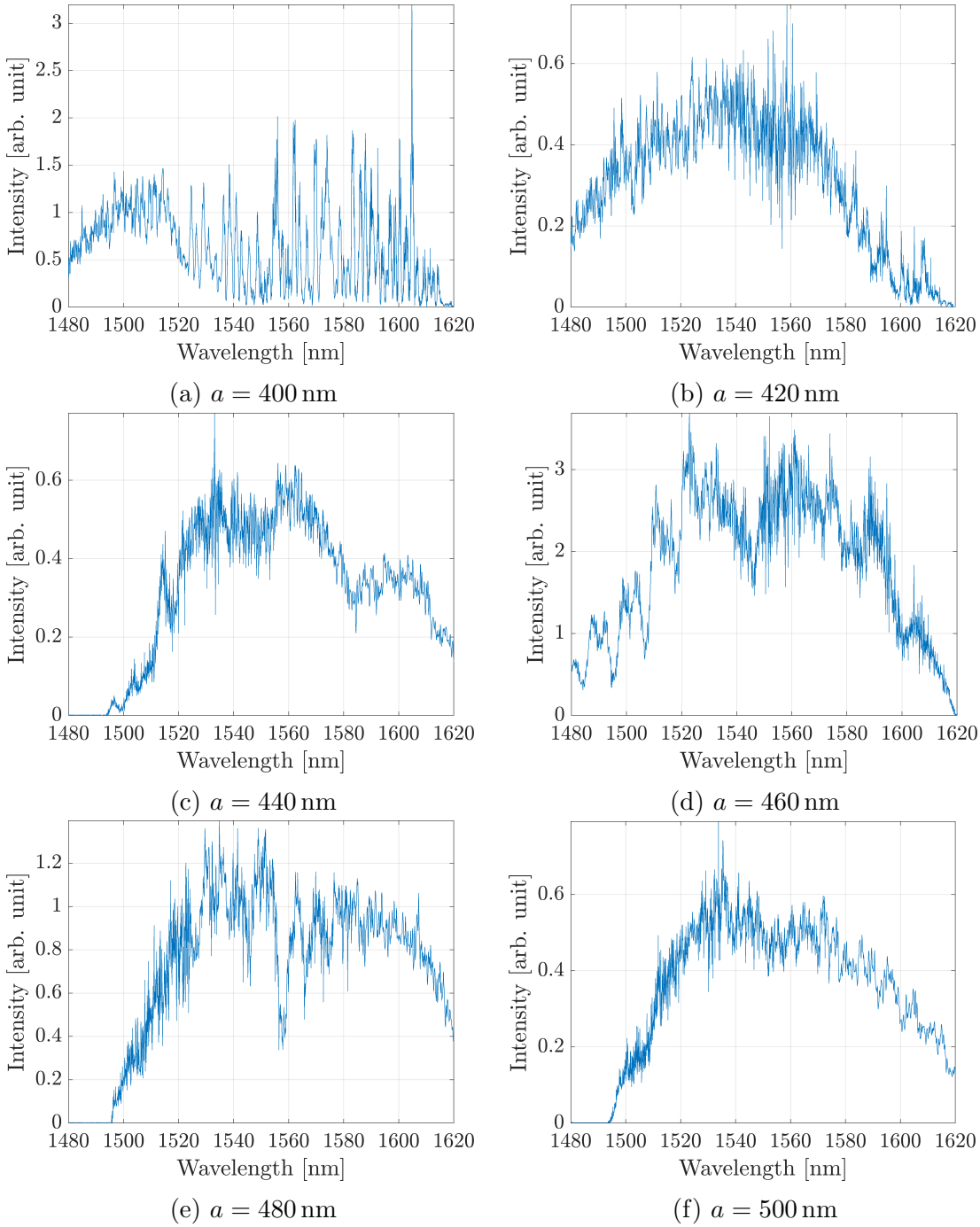

(a) $a = 400\,\text{nm}$ (b) $a = 420\,\text{nm}$

(c) $a = 440\,\text{nm}$ (d) $a = 460\,\text{nm}$

(e) $a = 480\,\text{nm}$ (f) $a = 500\,\text{nm}$

Figure 5.12: Transmitted light for 6 values of a. The intensity is given in arbitrary units and should not be compared. The photonic circuits were explained in subsection 4.5.1, and the PhC have a designed hole radius $r = 0.26a$, a strip waveguide width $\omega = 1.02a$, a waveguide-to-cavity distance $d = 3A$, a defect length $l = 9a$, a hole displacement of $0.25a$ and a silicon thin film thickness $h \approx 330\,\text{nm}$.

of a increases and the range of the laser wavelengths stays constant, the range of normalized frequencies under scrutiny will increase. The result of having 6 different values of a will therefore be a scan of a range of normalized frequencies, from $400/1620 = 0.247$ to $500/1480 = 0.338$. This might give the impression that a full graph of the band gap can be drawn from the findings. Unfortunately, another major change occurs when increasing the lattice constant: since the silicon thin film layer necessarily has the same thickness of approximately 330 nm for all values of a, the relative thickness will change from $h = 0.825a$ to $h = 0.660a$ for $a = 400$ nm and $a = 500$ nm, respectively. Increasing a will therefore give a smaller value of h, and thus a higher midgap frequency, as shown in subsection 5.1.2. Additionally, small variations of the actual radius of the holes will occur, and the 6 graphs seen in Figure 5.12 can therefore not be easily joined together to form a complete overview of the band gap.

It is also wise to remember that the transmission is determined not only by the photonic crystal, but by the other components on the sample, such as the waveguides and the tapers, as well as the optical setup. For instance, the output power of the laser will vary as a function of the wavelength [42], thereby explaining how almost all of the graphs in Figure 5.12 have a maximum transmission at approximately the same wavelength. In future work, this might be corrected for by using a look-up table. A change in the properties of the optical setup or the integrated waveguides and tapers might also explain the flattening of the transmission for wavelengths below 1495 nm for $a = 440$, 480 and 500 nm. These graphs were taken from another of the 6 sets of filters than the other three, and while the sets are supposed to be identical, small deviations are likely to occur. The flattening of the transmission might therefore be caused by some errors in that specific set, such as dirt, scratches or a bad scribe. However, a more probable explanation is based on the fact that the data for the two sets were obtained at different parts of the day. This implies a quite significant change in room temperature, and the properties of the laser might have changed as a result.

a [nm]	Wavelength [nm]	Normalized frequency	Amplitude	Quality factor
400	1528	0.262	13	~ 382
420	1595	0.263	56	~ 320
440	1517	0.290	52	~ 220
460	1553	0.296	29	~ 100

Table 5.5: Properties of the resonances shown in Figure 5.13. The amplitude was calculated by dividing the maximum intensity on the intensity of the noise.

The dropped light as a function of wavelength for the same 6 values of a as above can be seen in Figure 5.13. In each graph with $a \leq 460$ nm a clear resonance peak can be seen, while for the remaining two graphs several smaller peaks appear. While the latter is likely to be a result from noise, the former looks quite promising. The quality factors and amplitudes of the resonances seen for $a \leq 460$ nm were approximated and can be seen in Table 5.5 along with the resonance wavelengths and the normalized resonance frequencies. Notice how the normalized frequencies

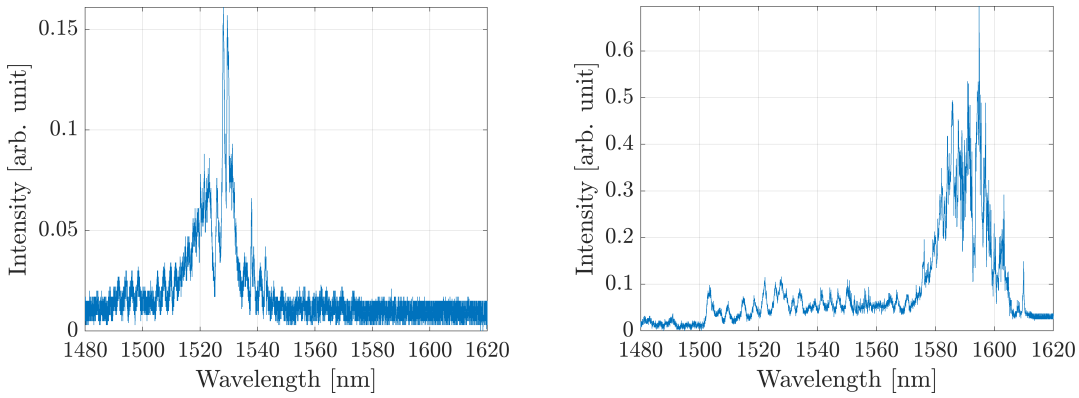

(a) $a = 400\,\text{nm}$

(b) $a = 420\,\text{nm}$

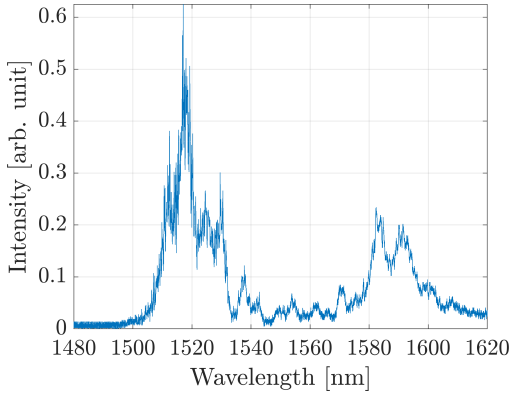

(c) $a = 440\,\text{nm}$

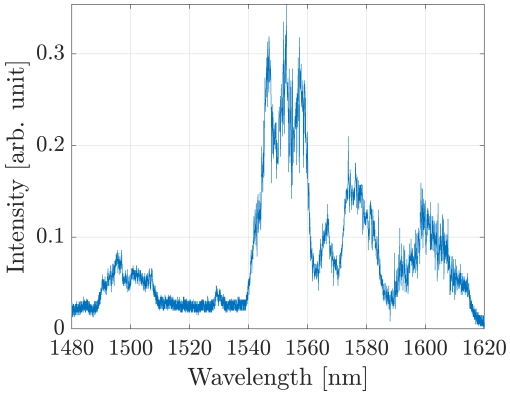

(d) $a = 460\,\text{nm}$

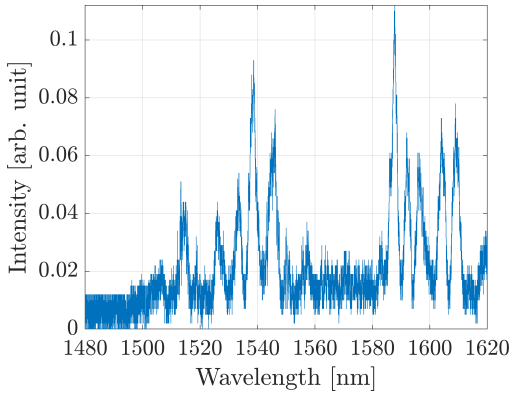

(e) $a = 480\,\text{nm}$

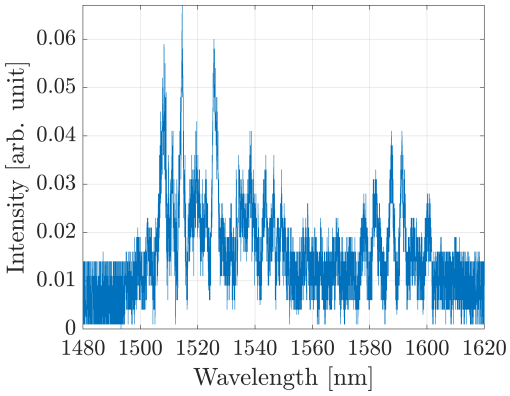

(f) $a = 500\,\text{nm}$

Figure 5.13: Dropped light for 6 values of a. The intensity is given in arbitrary units and should not be compared. The photonic circuits were explained in subsection 4.5.1, and the PhC have a designed hole radius $r = 0.26a$, a strip waveguide width $\omega = 1.02a$, a waveguide-to-cavity distance $d = 3A$, a defect length $l = 9a$, a hole displacement of $0.25a$ and a silicon thin film thickness $h \approx 330\,\text{nm}$.

of the resonance peaks for $a = 400$ and 420 nm are almost identical, as well as for $a = 440$ and 460 nm. This strongly indicates that pairs of the graphs in Figure 5.13 are actually showing more or less the same resonance, and that the small deviations in the normalized resonance frequencies are actually a result of the difference in the relative slab thickness h. One should therefore expect the other properties of the peaks to be similar as well, such as the amplitude and the quality factor. The latter value actually seems to be slightly similar for the members of the two pairs, though it is hard to tell due to the large uncertainty of the approximations. However, the amplitude deviates quite a lot. This is probably caused by defects in the strip waveguides or differences in the coupling efficiency between the sample and the fibers, and should not be stressed any further.

While the experimental results clearly indicate the presence of two resonance peaks at the normalized frequencies of approximately 0.26 and 0.29, no such resonances are indicated by the simulations, as shown in subsection 5.1.2. Instead, depending of the thickness, which for $400 \leq a \leq 460$ lies between $0.72a$ and $0.83a$, a resonance peak can be spotted at 0.263 for $h = 0.6a$, 0.250 for $h = 0.8a$ and 0.242 for $h = a$. The deviation in frequency between the simulations and the measurements can be explained partly by considering the hole radii for the 6 drop filters, as listed in Table 5.6. While the goal was to reach a hole radius of $0.3a$, as was the value used in the simulations, the real values are in fact quite a lot larger. An alternative explanation is based on the difference between the refractive index used in the simulations and the estimate found in subsection 5.2.3 for PECVD-grown a-Si. Both the decrease in refractive index and the increase in hole radius relative to the simulations will help shift the midgap and the resonances to higher frequencies, as shown in Figure 5.9. They might also open up for new resonances, and can therefore explain both the shift in the resonance observed for $a = 400$ and 420 nm, as well as the appearance of a resonance for $a = 440$ and 460 nm.

It is worth mentioning that before this sample was fabricated, an almost identical sample with a silicon thin film thickness of approximately 200 nm was made and characterized. While nice transmission signals were observed from its drop filters, neither of the filters showed any tendency to resonate. There are three aspects that in combination can explain this. First of all, a decrease in the coupling efficiency between the fibers and the sample was an inevitable consequence of a thinner silicon film, considering the equipment available. This would lead to less light passing

a [nm]	Radius [nm]	Normalized radius
400	132	0.331
420	139	0.332
440	141	0.320
460	149	0.324
480	157	0.327
500	163	0.327

Table 5.6: Hole radii obtained by measuring SEM images in ImageJ and calculating the average of seven holes.

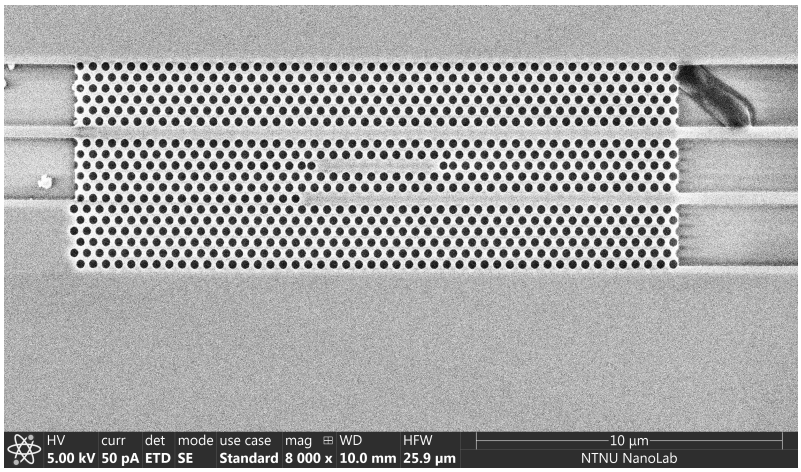

Figure 5.14: SEM image of a drop filter with $a = 420\,\text{nm}$. No cracks could be observed for any of the filters on the sample.

through the PhC, and therefore a lowering in the amount of dropped light at the resonance wavelength. Secondly, a film thickness of approximately 200 nm would mean a relative slab thickness h between $0.400a$ and $0.500a$ for a lattice constant in the range of 400 to 500 nm. In comparison, a film thickness of 330 nm would give a relative slab thickness between $0.660a$ and $0.825a$. According to subsection 5.1.2, the latter case would give a significantly larger amplitude for the resonance peak compared to the former case. It therefore seems possible that the resonance peak for such a thin silicon layer would be so small that is would simply drown in the noise of the system. Thirdly, there is a clear difference in the amounts of cracks observed in the SEM images for the two values of the silicon film thickness, as seen in Figure 5.14 and Figure 5.8 for $h = 330\,\text{nm}$ and $h = 200\,\text{nm}$, respectively. The disappearance of the cracks for the thicker film might be caused by a slightly different heat distribution in the resist during the soft bake, or by an improvement in the resist adhesion due to changes in the surface roughness. It might also be caused by the elimination of the ultrasonic bath as part of the resist removal process. Either way, it is possible, albeit unlikely, that these small imperfections observed for the thinner film have had some impact on the workings of the filter.

5.3.2 Biosensing

Figure 5.15 shows the result of the cleaning and the subsequent measurements using either air or water as a medium inside and on top of the PhC. Notice how, with each cleaning step, the resonance wavelength decreases. It seems likely that this change was caused by the presence of dirt and/or resist in the near vicinity of the photonic crystal, and that each cleaning step helped remove the contamination. This is particularly likely due to the lack of an ultrasonic bath in the resist removal. While microscope images indicated that the steps taken to remove the resist were sufficient, it is possible that small amounts of resist remained. Since the resist used in this work has a relative permittivity of 2.8 [61], it could have a significant effect on the effective refractive index, and thus the resonance wavelength.

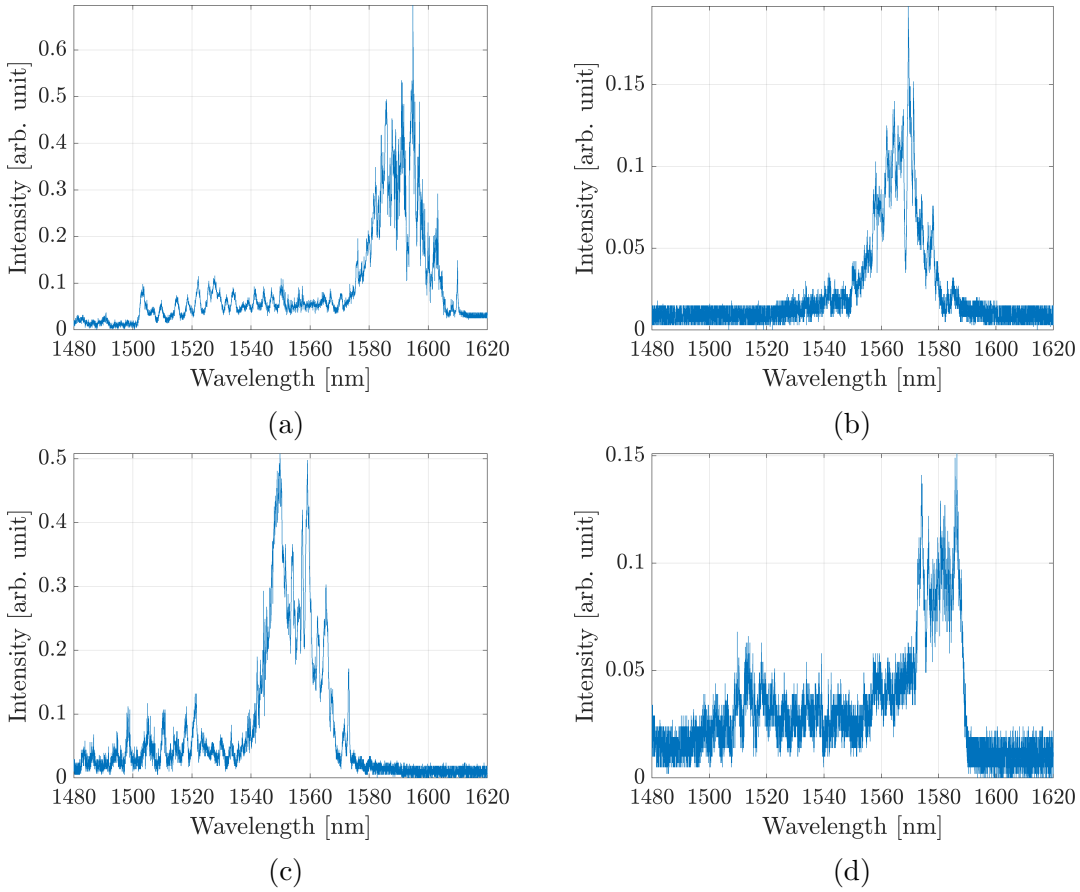

Figure 5.15: The dropped light for $a = 420\,\text{nm}$ as a function of wavelength. The measurements are taken on the same drop filter on the same sample as above, with the only difference being the cleaning of the sample before the measurements. While (a), as well as all the images shown in Figure 5.13, are taken directly after resist removal and sample scribing, the sample was cleaned with IPA and then allowed to air dry before the measurements seen in (b). The sample was then cleaned with IPA once more, air dried and then plasma cleaned for 3 min using 50 % oxygen and 50 % power before doing the measurements shown in (c). Finally, a drop of water was deposited on top of the sample, giving the results seen in (d).

To test this hypothesis, the sample was cleaned with IPA at the end of the experiment and imaged with a SEM, the result of which can be seen in Figure 5.16. While dirt can clearly be seen in Figure 5.16(a), no such particles are visible in Figure 5.16(b). The dirt seems to gather in the wide channels resulting from silicon etching, and the removal of the dust during cleaning can therefore be hindered by the relatively high channel walls. It is possible that air drying the sample using nitrogen might be enough to remove some of the dirt. However, while these dirt particles might lower the transmission, they are not capable of changing the resonance frequency, since they do not occupy the area above and inside the PhC drop filters. In fact, according to Figure 5.16(b) the dirt particles, if any, must be much smaller than the hole radius to ensure their invisibility on the SEM images. An alternative explanation might be that a continuous thin film of either IPA or resist remains inside the holes and on top of the PhC. This could both have a quite

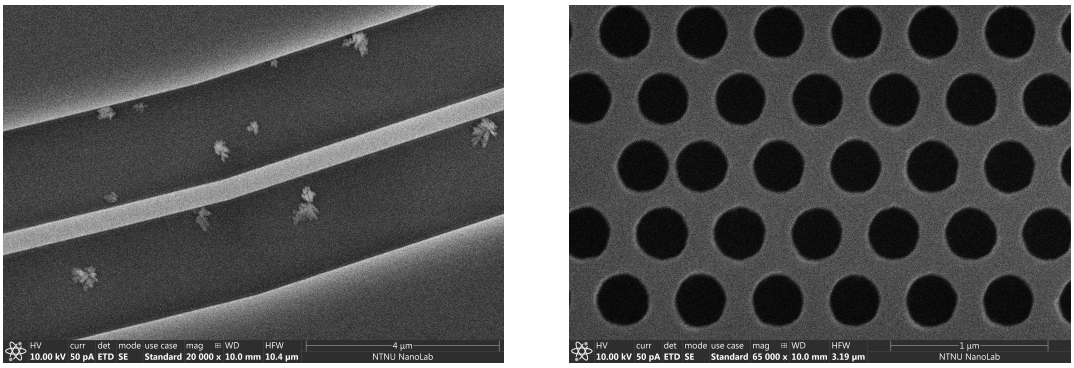

(a) (b)

Figure 5.16: SEM images of: (a) a waveguide bend and (b) a part of a PhC drop filter. While several dirt particles are visible in the strip waveguide margin, the PhC looks clean.

significant effect on the resonance wavelength, while also being hard to detect with a microscope.

Another surprising effect of the cleaning processes was the change in transmission for both output channels. While the transmissions both for the newly scribed sample and the sample that had been both cleaned and plasma cleaned were very high, the transmission for the sample that had only been rinsed with IPA was quite low. In fact, it was hard to get proper measurements for any of the filters. A theory is that the plasma cleaning caused an oxidization of the silicon surface, thus reclaiming some of the symmetry lost by having a substrate, and that cleaning the surface with IPA somehow ruined this effect. In that regard, it might be interesting to note that the wetting of the sample using Milli-Q water was much lower after the resist removal and the subsequent IPA rinse, then after the third IPA rinse and the following plasma cleaning. Since the resist removal was finished by plasma cleaning the sample, it seems likely that the IPA rinse somehow changed hydrophilicity of the silicon surface.

Whatever caused the shift in the resonance wavelength, it strongly indicates that the device is sensitive to changes in its surroundings. To further prove that, the last measurement was retaken after depositing a small drop of water on top of the sample. The result is shown in Figure 5.15(d), and both a shift in resonance wavelength and a lowering of the intensity can be seen. The shift is of approximately 25 nm, or 4.3×10^{-3} in normalized frequency units. This is slightly more than indicated by the Meep simulations, which demonstrated a shift of only 1.5×10^{-3} when changing the medium on top and inside the PhC from air to water. This might be explained by remembering that the etched holes ended up slightly larger than planned, as mentioned in subsection 5.3.1. Larger holes cause an increase in the interface between silicon and the hole medium, and it therefore seems likely that it will cause an increase in the sensitivity of the device.

Figure 5.17 presents the results from the biosensing experiment for the 3 remaining values of a that achieved a clear resonance, i.e. $a = 400$, 440 and 460 nm. A significant wavelength shift can be seen for all of them, and while its hard to determine the size of the shift for $a = 440$ and 460 nm, it was determined to be equal to 25 nm for $a = 400$ nm. It is therefore evident that the drop filter is indeed a

functioning biosensor.

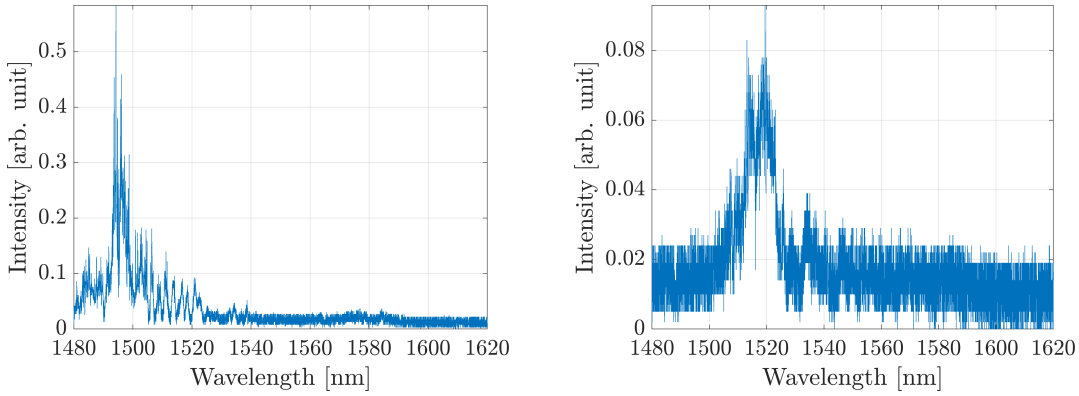

(a) Air and $a = 400\,\text{nm}$

(b) Water and $a = 400\,\text{nm}$

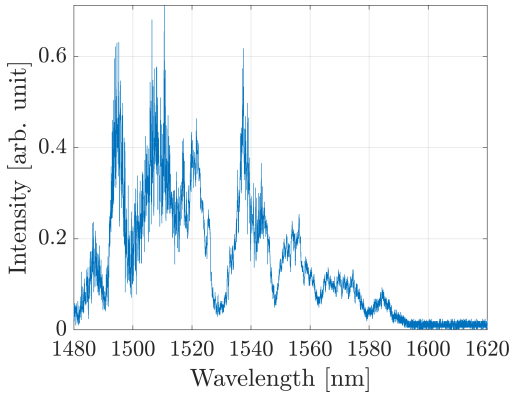

(c) Air and $a = 440\,\text{nm}$

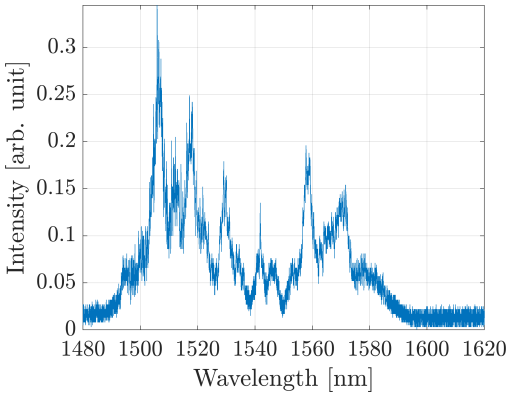

(d) Water and $a = 440\,\text{nm}$

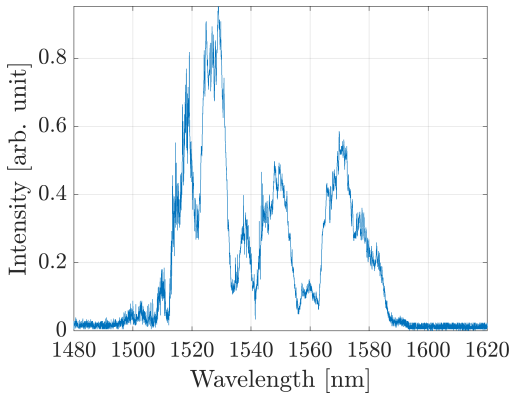

(e) Air and $a = 460\,\text{nm}$

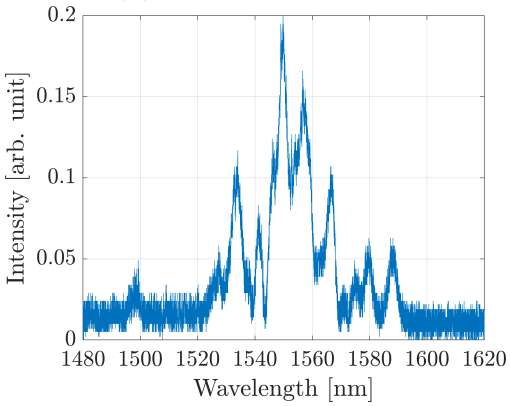

(f) Water and $a = 460\,\text{nm}$

Figure 5.17: Dropped light for 3 values of a, with either water or air on top and inside the PhC holes. The intensity is given in arbitrary units and should not be compared. The measurements are taken on the same sample as described in Figure 4.5. All filters were rinsed with IPA and plasma cleaned before the characterization.

Chapter 6

Summary and conclusion

Both the food and the health care industry have a large need for effective, cheap and portable biosensors that can be used with a minimal amount of training. Many approaches have been followed in the effort of achieving this, one of them being optical resonance filters. These devices will have a certain set of resonance frequencies depending upon the refractive index of the surrounding medium. The idea is to functionalize the resonance filter by attaching target-specific capture agents, for instance DNA or antibodies, to its surface. When a solution of different molecules, for instance blood or milk, is flushed over the device, the target molecules will attach themselves to the capture agents, and the refractive index near the surface of the filters will change according to the concentration of the targets. Now, while this method of biosensing has been achieved many times for different types of resonance filters, there is still much ongoing research to lower the amount of solution needed and to increase the sensitivity of the device. Several types of filters have been considered, including the photonic crystal drop filter that formed the core of this thesis. It consists of a silicon hole slab on SiO_2, and three linear defects, namely the two waveguides and a resonator in between them.

Simulations

The first part of the thesis involved simulating the photonic crystal drop filter using MIT Electromagnetic Equation Propagation (Meep) and MIT Photonic Bands (MPB). Most of the drop filter parameters had already been considered in my project thesis, including the hole radius, the resonator length and the distance between the resonator and the waveguides. The results from that work formed the basis for this thesis. However, the slab thickness h had been ignored until now, and the optimization concluded that a slab thickness of approximately $0.8a$ to $1.0a$, where a is the lattice constant, gave the highest and most consistent transmission, as well as the largest drop intensity for the resonances. In addition, the optical characterization method favored a thicker silicon layer, as that would increase the coupling efficiency between the fibers and the sample.

Simulations were also used to investigate the possibility of multiplexing the filters. This was done by placing two or more drop filters in series, so that the transmitted light from the first filter became the input light for the second, and so on. By giving them a slightly different lattice constant a, a small shift in their resonance

frequencies could be obtained, and interference effects were avoided. The idea was that by attaching different capture agents to each filter, the device would be able to detect several substances at once, using both the same detector and light source. During this thesis a multiplexing device consisting of two adjoined filters and with $a_2 = a_1/1.012$ was simulated in two dimensions using Meep. The result demonstrated a nice frequency shift between the two resonances. During the simulation, the dropped light of the two filters were led to separate detectors for clarity. This was done by adding 60° bends to the drop waveguides. Since the bends were likely to not support the resonance modes, and therefore force them to be reflected back into the filter, optimization was necessary. However, it was shown that even small optimizations of the bend design allowed it to not only support the resonances, but to reflect unwanted noise back into the filter.

Finally, simulations were used to approximate the sensitivity of the drop filters. Until this point, the medium inside the photonic crystal holes and above the crystal had been simulated as air, with refractive index $n_{\text{air}} = 1$. Now, however, it was replaced by a combination of a thin biolayer with $n_{\text{bio}} = 1.45$, and water with $n_{\text{water}} = 1.32$. The idea was that the biolayer would serve as a simple model of the capture agents and their targets, and that the sensitivity of the device could be approximated by simply increasing the width of the layer. The simulation results demonstrated a nice normalized frequency shift of 1.51×10^{-3} upon replacing air with water and a biolayer of zero thickness. Increasing the biolayer thickness t to $0.2r = 0.06a$, where r is the hole radius, gave an additional shift of 1.28×10^{-3}, which equals a sensitivity $S = \Delta\lambda/\Delta t = -0.348$. This demonstrates that the filters can successfully be utilized as biosensors.

Transition

The second part of the thesis focused on the transition from simulations to fabrications. Among other things, the deviation in the results from the fabrications and the simulations were studied. This deviation was mainly caused by two factors. Firstly, the hole radius of the fabricated devices always differed somewhat from the hole radius of the mask file due to the proximity effect. Secondly, while the refractive index of the silicon slab, which was amorphous and grown using PECVD, was assumed to be similar to the refractive index of crystalline silicon, i.e. $n_{\text{c-Si}} = 3.48$, during the simulations, this was not necessarily correct. A combination of simulations, fabrications and characterizations were therefore used to roughly approximate the refractive index of the silicon slab as $n_{\text{a-Si}} = 3.37$.

Two more aspects were considered in this part of the thesis. First, a test of two different sets of silicon growth and etch times were carried out by imaging the cross section of the fabricated photonic crystals. This then revealed both that the thicknesses of the silicon slabs were slightly smaller then expected for the given growth times, and that the etch times were sufficient to achieve fully etched holes. Secondly, the issue of resist cracking was addressed. It was found that this problem arose from a faulty soft bake procedure and subsequent resist tensions, and it was solved by increasing the baking time from 1 min to 3 min, improving the contact between hot plate and sample and increasing the hot plate temperature to ensure that the resist reached 150 °C.

Fabrication

The results from the subsequent work were finally used to create a functioning drop filter with a hole radius $r \approx 0.32a$, a center-to-center distance between the resonator and the waveguides $d = 3A = 3\sqrt{3}a/2$ and a resonator length equaling the absence of 9 holes. A small displacement of $0.25a$ for the holes at the beginning and end of the resonator had also been made. The results included resonances of sufficient intensity to be clearly discernible above the noise for $400\,\text{nm} \leq a \leq 460\,\text{nm}$ and $h = 330\,\text{nm}$. A similar drop filter had been attempted for $h = 220\,\text{nm}$, but it was unsuccessful.

Afterwards, the biosensing abilities of the drop filter were tested by depositing a small drop of purified water on top of the sample. This resulted in a shift of 25 nm, which equals a normalized frequency shift of 4.3×10^{-3}.

Future research

While several issues have already been addressed in this thesis or in past work by others in the research group, many more remain. Below follows a list of suggestions for future work:

- Improve the filter design to achieve a higher quality factor and sensitivity while also maintaining the high intensity of the resonance peaks. An effective way of achieving this might include the removal of the oxide substrate below the photonic crystals.
- Obtain increased knowledge of the fabrication parameters, such that demands for a certain slab thickness or hole radius can be met more easily.
- Take advantage of more advanced computational hardware during the simulations. Both Meep and MPB supports parallel computing [31, 68], so an increase in processing power and memory would be highly valuable and allow for an increase in both simulation durations and resolution.
- Fabricate a multiplexing device. While some effort was done on this during the thesis, there was not enough time available to overcome the challenges.
- Functionalize the surface of the filters with target-specific capture agents. This would allow for better measurements of the sensitivity.
- Achieve better control of the flow of the test fluid by taking advantage of microfluidics.
- Integrate the filters into a lab-on-a-chip.

Conclusion

The main goal of this master thesis was to design and fabricate a biosensor consisting of a 2D photonic crystal drop filter. After much effort, the sensor was successfully created. Its biosensing abilities were tested by changing the surrounding medium from air to purified water both inside the photonic crystal holes and above the

crystal. It resulted in a resonance shift of approximately 25 nm, which corresponded to a normalized frequency shift of 4.3×10^{-3}. While further research on the subject is still needed, there is no doubting the success of the project.

Bibliography

[1] I. Hellen. "Photonic crystal drop filter for lab-on-a-chip biosensor". Report from Specialization Project. NTNU, 2017.

[2] L. Holmen. "Simulation and Fabrication of a Photonic Crystal Mach-Zehnder Interferometer". Master thesis. Norwegian university of science and technology (NTNU), 2016.

[3] M. Stein. "Simulations of Photonic Crystal Waveguides and Process Optimization of Strip Waveguides". Report from Specialization Project. Norwegian university of science and technology (NTNU), 2017.

[4] M. O. Stein. "Simulations and Fabrication of Photonic Crystal Waveguides and a Computational Study of Two-Dimensional Photonic Crystal Cavity Resonators". Master thesis. NTNU, 2018.

[5] J. Høvik. "Simulation and Fabrication of a Photonic Crystal Mach-Zehnder Interferometer". Master thesis. Norwegian university of science and technology (NTNU), 2012.

[6] J. Joannopoulos et al. *Photonic Crystals: Molding the Flow of Light*. 2nd. 2008.

[7] B. Saleh and M. Teich. *Fundamentals of photonics*. 2nd ed. 2014.

[8] E. Yablonovitch. "Inhibited Spontaneous Emission in Solid-State Physics and Electronics". In: *Physical Review Letters* 58.20 (1987).

[9] S. John. "Strong Localization of Photons in Certain Disordered Dielectric Superlattices". In: *Physical Review Letters* 58.23 (1987).

[10] "Early lights". In: *Nature Materials* 11.12 (2012), p. 995. DOI: 10.1038/nmat3519.

[11] X. Fan et al. "Sensitive optical biosensors for unlabeled targets: A review". In: *Analytica chimica acta* 620 (2008), pp. 8–26. DOI: 10.1016/j.aca.2008.05.022.

[12] Y. Zhang, Y. Zhao, and R. Lv. "A review for optical sensors based on photonic crystal cavities". In: *Sensors and Actuators* 233 (2015), pp. 374–389. DOI: 10.1016/j.sna.2015.07.025.

[13] N. Skivesen, A. Têtu, and M. Kristensen. "Photonic-crystal waveguide biosensor". In: *Optics express* 15.6 (2007).

[14] M. Lee and P. Fauchet. "Two-dimensional silicon photonic crystal based biosensing platform for protein detection". In: *Optics Express* 15.8 (2007), pp. 4530–4535. DOI: 10.1364/OE.15.004530.

[15] D. Dorfner et al. "Photonic crystal nanostructures for optical biosensing applications". In: *Biosensors and Bioelectronics* 24 (2009), pp. 3688–3692. DOI: 10.1016/j.bios.2009.05.014.

[16] S. Pal et al. "Microcavities in Photonic Crystal Waveguides for Biosensor Applications". In: *Proc. of SPIE* 7553 (2010). DOI: 10.1117/12.848237.

[17] D. F. Dorfner et al. "Silicon photonic crystal nanostructures for refractive index sensing". In: *Applied Physics Letters* 93.18 (2008). DOI: 10.1063/1.3009203.

[18] L. Holmen. "Simulations of Photonic Crystal Mach-Zehnder Interferometers for Biosensing Applications". Report from Specialization Project. Norwegian university of science and technology (NTNU), 2015.

[19] W.-C. Lai et al. "Silicon nano-membrane based photonic crystal microcavities for high sensitivity bio-sensing". In: *Optics Letters* 37.7 (2012), pp. 1208–1210. DOI: 10.1364/OL.37.001208.

[20] H. Takano et al. "Highly efficient multi-channel drop filter in a two-dimensional hetero photonic crystal". In: *Optics Express* 14.8 (2006), pp. 3491–3496. DOI: 10.1364/OE.14.003491.

[21] H. Takano et al. "In-plane-type channel drop filter in a two-dimensional photonic crystal slab". In: *Applied Phiscs Letters* 84.13 (2004), pp. 2226–2228. DOI: 10.1063/1.1689742.

[22] M. Notomi et al. "Waveguides, resonators and their coupled elements in photonic crystal slabs". In: *Optics Express* 12.8 (2004), p. 1551. DOI: 10.1364/opex.12.001551.

[23] R. Renneberg. *Biotechnology for Beginners*. 2007.

[24] Y. Zou et al. "Cavity-Waveguide Coupling Engineered High Sensitivity Silicon Photonic Crystal Microcavity Biosensors With High Yield". In: *IEEE journal of selected topics in quantum electronics* 20.4 (2014).

[25] A. Oskooi et al. "MEEP: A flexible free-software package for electromagnetic simulations by the FDTD method". In: *Computer Physics Communications* 181 (2010), pp. 687–702.

[26] F. Grillot et al. "Propagation Loss in Single-Mode Ultrasmall Square Silicon-on-Insulator Optical Waveguides". In: *Journal of lightwave technology* 24.2 (2006).

[27] Y. A. Vlasov and S. J. McNab. "Losses in single-mode silicon-on-insulator strip waveguides and bends". In: *Optics Express* 12.8 (2004), p. 1622. DOI: 10.1364/opex.12.001622. URL: https://doi.org/10.1364/opex.12.001622.

[28] S. Johnson and C. Kreuzer. *Discussion: Negative Q and error bar in harminv*. June 7, 2018. URL: http://meep-discuss.ab-initio.mit.narkive.com/tGAnGr0O/negative-q-and-error-bar-in-harminv.

[29] S. Johnson and J. Joannopoulos. "Block-iterative frequency-domain methods for Maxwell's equations in a planewave basis". In: *Optics Express* 8.3 (2001), pp. 173–190.

[30] T. Bolstad. "Fabrication of a Silicon Photonic Crystal Biosensor". Master thesis. Norwegian university of science and technology (NTNU), 2014.

[31] *MPB documentation*. URL: http://mpb.readthedocs.io (visited on 11/10/2017).

[32] M. Qiu. "Effective index method for heterostructure-slab-waveguide-based two-dimensional photonic crystal". In: *Applied Physics Letters* 81 (2002), p. 1163. DOI: 10.1063/1.1500774.

[33] M. Quirk and J. Serda. *Semiconductor Manufactoring Technology*. 1st. 2001.

[34] J. H. W. S. of Engineering. *Plasma Cleaner: Physics of Plasma*. 2016. URL: https://engineering.jhu.edu/labs/wp-content/uploads/sites/76/2016/04/All-About-Plasma-Cleaning.pdf (visited on 01/17/2018).

[35] M. A. Mohammad et al. "Fundamentals of Electron Beam Exposure and Development". In: *Nanofabrication*. Ed. by M. Stepanova and S. Dew. Springer, 2012. Chap. 2, pp. 11–42.

[36] R. Egerton. *Physical Principles of Electron Microscopy - An Introduction to TEM, SEM, and AEM*. 1st. Springer, 2005.

[37] W. Bogaerts and S. Selvaraja. "Silicon-on-Insulator (SOI) Technology for Photonic Integrated Circuits (PICs)". In: *Silicon-on-Insulator (SOI) Technology - Manufacture and Applications*. Ed. by O. Kononchuk and B.-Y. Nguyen. Elsevier, 2014. Chap. 13.

[38] D. Sparacin, S. Spector, and L. Kimerling. "Silicon waveguide sidewall smoothing by wet chemical oxidation". In: *Journal of Lightwave Technology* 23.8 (2005), pp. 2455–2461. DOI: 10.1109/JLT.2005.851328.

[39] R. Takei. "Amorphous Silicon Photonics". In: *Crystalline and Non-crystalline Solids*. Ed. by P. Mandracci. InTech, 2016. Chap. 6.

[40] *Electron- and laser-beam lithography software*. GenISys. June 10, 2018. URL: https://www.genisys-gmbh.com/web/products/beamer.html.

[41] A. Nanakoudis. *Spot size in scanning electron microscopy (SEM): why it matters!* 2017. URL: http://blog.phenom-world.com/spot-size-scanning-electron-microscopy-sem (visited on 01/17/2018).

[42] *Tunable Laser Kit User Guide*. ThorLabs. Mar. 2014.

[43] B.-S. Song et al. "Ultra-high-Q photonic double-heterostructure nanocavity". In: *Nature Materials* 4 (2005). DOI: 10.1038/nmat1320.

[44] M. Notomi et al. "Structural tuning of guiding modes of line-defect waveguides of silicon-on-insulator photonic crystal slabs". In: *IEEE Journal of Quantum Electronics* 38.7 (2002), pp. 736–742. DOI: 10.1109/JQE.2002.1017583.

[45] B.-S. Song, T. Asano, and S. Noda. "Heterostructures in two-dimensional photonic-crystal slabs and their application to nanocavities". In: *Journal of Physics D: Applied Physics* 40.9 (2007), p. 2629. DOI: 10.1088/0022-3727/40/9/S03.

[46] M. Miyamoto. "Prevention of Microroughness Generation on the Silicon Wafer Surface in Buffered Hydrogen Fluoride by a Surfactant Addition". In: *Journal of The Electrochemical Society* 141.10 (1994), p. 2899. DOI: 10.1149/1.2059253. URL: https://doi.org/10.1149/1.2059253.

[47] *Wet etching of silicon dioxide*. URL: http://www.microtechweb.com/kb/sio_etch.htm (visited on 06/21/2018).

[48] *Working with hydrogen fluoride and related substances*. URL: https://innsida.ntnu.no/wiki/-/wiki/English/Working+with+hydrogen+fluoride+and+related+substances (visited on 06/21/2018).

[49] Y. Vlasov and S. McNab. "Coupling into the slow light mode in slab-type photonic crystal waveguide". In: *Optics Letters* 31.1 (2006), pp. 50–52.

[50] C. Jamois et al. "Silicon-based two-dimensional photonic crystal waveguide". In: *Photonics and Nanostructures - Fundamentals and Applications* 1 (2003), pp. 1–13. DOI: 10.1016/j.photonics.2003.10.001.

[51] T. Nakamura et al. "Improvement in the quality factors for photonic crystal nanocavities via visualization of the leaky components". In: *Optics express* 24.9 (2016). DOI: 10.1364/OE.24.009541.

[52] L. H. Frandsen et al. "Broadband photonic crystal waveguide 60° bend obtained utilizing topology optimization". In: *Optics Express* 12.24 (2004), p. 5916. DOI: 10.1364/opex.12.005916. URL: https://doi.org/10.1364/opex.12.005916.

[53] A. Chutinan, M. Okano, and S. Noda. "Wider bandwidth with high transmission through waveguide bends in two-dimensional photonic crystal slabs". In: *Applied Physics Letters* 80.10 (Mar. 2002), pp. 1698–1700. DOI: 10.1063/1.1458529. URL: https://doi.org/10.1063/1.1458529.

[54] P. Xing et al. "Optimization of bandwidth in 60° photonic crystal waveguide bends". In: *Optics Communications* 248.1-3 (Apr. 2005), pp. 179–184. DOI: 10.1016/j.optcom.2004.12.003. URL: https://doi.org/10.1016/j.optcom.2004.12.003.

[55] Z. Hu and Y. Y. Lu. "Improved bends for two-dimensional photonic crystal waveguides". In: *Optics Communications* 284.12 (June 2011), pp. 2812–2816. DOI: 10.1016/j.optcom.2011.01.067. URL: https://doi.org/10.1016/j.optcom.2011.01.067.

[56] I. Ntakis, P. Pottier, and R. M. D. L. Rue. "Optimization of transmission properties of two-dimensional photonic crystal channel waveguide bends through local lattice deformation". In: *Journal of Applied Physics* 96.1 (July 2004), pp. 12–18. DOI: 10.1063/1.1753084. URL: https://doi.org/10.1063/1.1753084.

[57] *Refractive index database*. URL: https://refractiveindex.info/?shelf=main&book=H2O&page=Kedenburg (visited on 11/30/2017).

[58] S. Kedenburg et al. "Linear refractive index and absorption measurements of nonlinear optical liquids in the visible and near-infrared spectral region". In: *Optical Materials Express* 2.11 (2012), pp. 1588–1611. DOI: 10.1364/ome.2.001588.

[59] S. Lai, D. Johnson, and R. Westerman. "Aspect ratio dependent etching lag reduction in deep silicon etch processes". In: *Journal of Vacuum Science & Technology A: Vacuum, Surfaces, and Films* 24.4 (2006), pp. 1283–1288. DOI: doi.org/10.1116/1.2172944.

[60] J. Li et al. "Technique for preventing stiction and notching effect on silicon-on-insulator microstructure". In: *Journal of Vacuum Science & Technology B: Microelectronics and Nanometer Structures* 21.6 (2003), p. 2530. DOI: 10.1116/1.1623509.

[61] *Positive E-Beam Resists AR-P 6200 (CSAR 62)*. Allresist GmbH. 2017.

[62] *What is Milli Q Water*. URL: https://www.apswater.com/article.asp?id=335&title=What+is+Milli-Q+Water (visited on 06/18/2018).

[63] O. Painter, J. Vučkovič, and A. Scherer. "Defect modes of a two-dimensional photonic crystal in an optically thin dielectric slab". In: *Journal of the Optical Society of America B* 16.2 (Feb. 1999), p. 275. DOI: 10.1364/josab.16.000275. URL: https://doi.org/10.1364/josab.16.000275.

[64] Y. Kryukov et al. "Experimental and theoretical study of the evolution of surface roughness in amorphous silicon films grown by low-temperature plasma-enhanced chemical vapor deposition". In: *Physical review B* 80.8 (2009). DOI: 10.1103/physrevb.80.085403.

[65] S. Zhu, G. Q. Lo, and D. L. Kwong. "Low-loss amorphous silicon wire waveguide for integrated photonics: effect of fabrication process and the thermal stability". In: *Optics Express* 18.24 (2010), pp. 25283–25291. DOI: 10.1364/oe.18.025283.

[66] J. T. Kindt and R. C. Bailey. "Chaperone Probes and Bead-Based Enhancement To Improve the Direct Detection of mRNA Using Silicon Photonic Sensor Arrays". In: *Analytical Chemistry* 84.18 (2012), pp. 8067–8074. DOI: 10.1021/ac3019813.

[67] M. Metzler and R. Patel. "Plasma Enhanced Chemical Vapor Deposition (PECVD) of Silicon Dioxide (SiO2) Using Oxford Instruments System 100 PECVD". In: *Scholarly Commons* (2017).

[68] *MEEP documentation*. URL: https://meep.readthedocs.io (visited on 09/28/2017).

Appendices

Appendix A

Meep tutorial

Meep is a finite-difference time-domain (FDTD) simulation language [25]. It has been used thoroughly in this work, and a short tutorial based on my own code will be presented. However, Meep will not be discussed in detail, and for a proper guiding through the workings of Meep, [68] is recommended. It includes several basic tutorials and an installation guide, which could come in handy. There is also a tutorial similar to this one in appendix A of [3], and a great deal of my code is based on that tutorial. However, the code shown there simply creates a photonic crystal waveguide, not a drop filter, and it will, due to some errors, not compile straight away.

The tutorial does, among other things, define the simulation geometry, which consists of a set of discrete objects with a certain size, position and permittivity. However, if the simulation was run with this exact geometry, then the output would be discrete as well. To avoid that, Meep uses subpixel averaging to smooth out the interfaces between different object [25]. However, outputs of the final dielectric function indicated that it may not always work correctly when several layers of a material are put on top of one another. In fact, it was observed that if a small bulk of material A was used to cover over a larger bulk of material A next to its interface with material B, then the pixels at the interface where the small bulk had been added, would be of a different color then where it had not. While this seemed to have little importance on the final result, it might be wise to output the final dielectric function sometimes to verify that it looks alright.

In general, it is easier to run Meep on a Linux computer, but other operating systems can work as well. Meep is run from the terminal by using a few short commands. When making a transmission spectrum these demands are as follows:

```
meep ref_run=true data.ctl | tee ref.out
meep data.ctl | tee data.out
#These two lines runs a Meep script, as the one shown below.
#The first line runs a reference run.
#The runtime events and results are written both to terminal
# and the .out file

#The results from the .out file is collected and put into
# a .dat file:
```

```
grep flux1: data.out > data.dat
grep flux1: ref.out > ref.dat
```

Since a Meep source outputs light with a different amplitude for different frequencies, it is necessary to divide the transmission results for each frequency on the source amplitude for that frequency. However, because the source amplitude is not stored anywhere, a reference run has to be made. The reference geometry consists of a simple silicon waveguide in air, as shown in the Meep code below. Since such a waveguide can be considered almost perfect, we can measure the source output for each frequency by measuring the waveguide transmission. Also, the reference run creates a data-refl-flux file, which is loaded during the main run to shorten down the processing time. Fortunately, a reference run is not necessary when running a Harminv simulation.

When you run this script, make sure to use a sufficiently small value of decay_until. Meep calculates the maximum output intensity through a given port during the run. It will then compare the output at all later times at the same port, and when the fraction becomes less than decay_until, it completes the run. If the value is too large, a significant amount of light might still be trapped in the crystal, for instance in the cavity, and the result might be misleading. However, it will of course take a lot more time to run the simulations if decay_until is very small. A good starting point is to set decay_until=1e−3, and then lower the value for more important simulations until it stops making a difference in the result. If you run the script in harminv mode, the same can be said about the harminv_decay_until variable. A good starting point would be to set it equal to a thousand. According to Steven G. Johnson, who is one of the creators of Meep, it is also important to use as small a light pulse width as possible, as this will give more accurate results for the quality factor and help avoid invalid negative results [25, 28].

```
reset-meep

; the type of simulation is defined
(define-param ref_run false); reference run
(define-param 3D false); 2D or 3D simulation
(define-param bottom_oxide false); air-bridge slab or SOI slab.
(define-param displaced false); displacements of holes close to the
    cavity
(define-param movie false); if true, the efield in y-direction is
    outputed at even intervals
(define-param trans_exit false); if true, the top waveguide outputs at
    both ends
(define-param biosensing false); if true, air is replaced by a liquid
    in the pc.
(define-param resonance false); if true, a harminv simulation is run.
    If false, a transmission spectrum is made instead
(define-param nfreq 4000); number of frequencies for computing flux

; constants regarding the geometry are defined
(define A (/ (sqrt 3) 2)); distance between rows in Gamma-M (y)
```

```
    direction
(define-param r 0.339); hole radius, important that 2r<wg_width
(define-param r2 0); radius of holes in cavity
(define-param bio_thickness 0.1717); multiplied with r, this is the
    thickness of the biolayer
(define lbio (* r bio_thickness)); thickness of biolayer
(define rbio (- r lbio)); the radius of the inner circle of the holes,
    which will be filled with water if biosensing=true
(define wg_width 0.82); width of strip waveguide
(define wg_length 2); length of strip waveguides
(define pml_t 1); thickness of PML layer
(define flux_sep 0.5); distance from right flux plane to PML layer
(define source_sep 0.25); distance from source plane to PML
(define-param wg_dist_int 5); wg_dist_int-1 is the number of holes
    separating waveguide from cavity
(define numx (- 29 (remainder wg_dist_int 2))); number of periods along
    the waveguide
(define numy (+ 11 (* (+ wg_dist_int -1) 2))); (odd) number of periods in
    the y-direction
(define sx (+ numx (* 2 wg_length) (* 2 pml_t))); size of the domain in
    x-direction
(define sy (+ (* numy A) (* 2 pml_t))); size of domain in y-direction
(define flux_pos_x (- (/ sx 2) (+ pml_t flux_sep))); position of the flux
    plane for transmission
(define source_pos_x (- (/ sx 2) (+ pml_t source_sep))); position of the
    source plane
(define-param h 0.55); thickness of the slab
(define zmargin 2); margin between slab and pml layer in the z
    direction
(define sz (+ (* 2 pml_t) h (* 2 zmargin))); size of the domain in the
    z-direction
(define wg_dist (* A wg_dist_int)); distance between the center and the
    waveguides
(define-param defect_length 9); the length of the defect, ie how many
    holes are missing
(define-param decay_until 1e-3); the program will run until the output
     at a selected gate has decayed to this share of its max value
(define-param harminv_decay_until 1000); the run time for a harminv
    simulation
(define-param displace_dist_1 0.25); inner displacement value if
    displaced=true
(define-param displace_dist_2 0); outer displacement value if displaced=
    true, 0.15 is best
(define pc_wg_length (+ (/ sx 2) (/ defect_length 2) (/ (remainder wg_dist_int 2)
    2) 1)); length of the pc waveguide if trans_exit=false
(define-param video_interval 10); time interval between each e-field
```

```
    output if movie=true
(define-param res 20)

; defining the source properties
(define-param fcen 0.32); pulse center frequency
(define-param dff 0.14); pulse width in frequency

; defining the simulation domain
(set! geometry-lattice
  (make lattice
    (size sx sy
      (if 3D sz no-size))))

; defining dielectric constants and materials
; for 2D simulations, the effective dielectric constant is used
(define eps_silicon (if 3D 12.11 8.23))
(define eps_oxide 2.07)
(define eps_bio (if 3D 2.10 1.34))
(define eps_water (if 3D 1.73 1.33)); water at 20C and 1.55 um light.
(define si (make dielectric (epsilon eps_silicon)))
(define oxide (make dielectric (epsilon eps_oxide)))
(define bio (make dielectric (epsilon eps_bio)))
(define water (make dielectric (epsilon eps_water)))

(if
  (not ref_run)
    (if biosensing
      (if 3D
        (set! default-material water))))


; starting to define the simulation geometry:
; 1: defining a waveguide across the entire cell if reference run or
    a slab of length num if not, with bio on both sides if biosensing
(set! geometry
  (list
    (if ref_run
      (make block
        (center 0 wg_dist 0)
        (material si)
        (size infinity wg_width
          (if 3D h infinity)))
      (make block
        (center 0 0 0)
        (material si)
        (size numx infinity
```

```
          (if 3D h infinity))))))

(if (not ref_run)
  (if biosensing
    (if 3D
      (set! geometry
        (append geometry
          (list
            (make block
              (center 0 0 (* (+ lbio h) 0.5))
              (material bio)
              (size numx infinity lbio))
            (make block
              (center 0 0 (* (+ lbio h) -0.5))
              (material bio)
              (size numx infinity lbio)))))))))

; 2: creating air holes. It makes a diagonal row of holes that is
   copied along its normal. If biosensing is on, air is replaced by
   a biolayer and water
(if (not ref_run)
  (set! geometry
    (append geometry
      (geometric-objects-duplicates
        (vector3 0.5 A 0)
        (- (+ numx))
        (+ numx 1)
        (geometric-object-duplicates (vector3 0.5 (* A -1) 0)
          (- (+ numx 1))
          (+ numx 1)
          (make cylinder
            (center 0 0 0)
            (radius r)
            (height (if 3D (+ h lbio lbio) infinity))
            (material (if biosensing bio air))))))))

(if biosensing
  (if (not ref_run)
    (set! geometry
      (append geometry
        (geometric-objects-duplicates
          (vector3 0.5 A 0)
          (- (+ numx))
          (+ numx 1)
          (geometric-object-duplicates (vector3 0.5 (* A -1) 0)
            (- (+ numx 1))
```

```
            (+ numx 1)
            (make cylinder
              (center 0 0 0)
              (radius rbio)
              (height (if 3D (+ h lbio lbio) infinity))
              (material water))))))))

; 3: changing the radius of the air holes of the linear defect by
   first filling in the existing holes and then make new ones. If
   displaced=true, the holes near the cavity is filled in and moved
(if (not ref_run)
  (if biosensing
    (if 3D
      (if displaced
        (set! geometry
          (append geometry
            (list
              (make block
                (center 0 0 0)
                (material bio)
                (size
                  (+ defect_length 6)
                  (* 2 r)
                  (+ h lbio lbio))))))
        (set! geometry
          (append geometry
            (list
              (make block
                (center 0 0 0)
                (material bio)
                (size
                  defect_length
                  (* 2 r)
                  (+ h lbio lbio)))))))))))


(if (not ref_run)
  (if displaced
    (begin
      (set! geometry
        (append geometry
          (list
            (make block
              (center 0 0 0)
              (material si)
              (size
```

```
            (+ defect_length 6)
            (* 2 r)
            (if 3D h infinity)))
        (make cylinder
          (center (* (+ (/ (- defect_length 1) 2) 1 displace_dist_1) -1) 0 0)
          (radius r)
          (height (if 3D (+ h lbio lbio) infinity))
          (material (if biosensing bio air)))
        (make cylinder
          (center (* (+ (/ (- defect_length 1) 2) 2) -1) 0 0)
          (radius r)
          (height (if 3D (+ h lbio lbio) infinity))
          (material (if biosensing bio air)))
        (make cylinder
          (center (* (+ (/ (- defect_length 1) 2) 3 displace_dist_2) -1) 0 0)
          (radius r)
          (height (if 3D (+ h lbio lbio) infinity))
          (material (if biosensing bio air)))
        (make cylinder
          (center (+ (/ (- defect_length 1) 2) 1 displace_dist_1) 0 0)
          (radius r)
          (height (if 3D (+ h lbio lbio) infinity))
          (material (if biosensing bio air)))
        (make cylinder
          (center (+ (/ (- defect_length 1) 2) 2) 0 0)
          (radius r)
          (height (if 3D (+ h lbio lbio) infinity))
          (material (if biosensing bio air)))
        (make cylinder
          (center (+ (/ (- defect_length 1) 2) 3 displace_dist_2) 0 0)
          (radius r)
          (height (if 3D (+ h lbio lbio) infinity))
          (material (if biosensing bio air))))))
  (if biosensing
    (set! geometry
      (append geometry
        (list
          (make cylinder
            (center (* (+ (/ (- defect_length 1) 2) 1 displace_dist_1) -1) 0
                0)
            (radius rbio)
            (height (if 3D (+ h lbio lbio) infinity))
            (material water))
          (make cylinder
            (center (* (+ (/ (- defect_length 1) 2) 2) -1) 0 0)
            (radius rbio)
```

```
                (height (if 3D (+ h lbio lbio) infinity))
                (material water))
              (make cylinder
                (center (* (+ (/ (- defect_length 1) 2) 3 displace_dist_2) -1) 0
                    0)
                (radius rbio)
                (height (if 3D (+ h lbio lbio) infinity))
                (material water))
              (make cylinder
                (center (+ (/ (- defect_length 1) 2) 1 displace_dist_1) 0 0)
                (radius rbio)
                (height (if 3D (+ h lbio lbio) infinity))
                (material water))
              (make cylinder
                (center (+ (/ (- defect_length 1) 2) 2) 0 0)
                (radius rbio)
                (height (if 3D (+ h lbio lbio) infinity))
                (material water))
              (make cylinder
                (center (+ (/ (- defect_length 1) 2) 3 displace_dist_2) 0 0)
                (radius rbio)
                (height (if 3D (+ h lbio lbio) infinity))
                (material water)))))))
  (set! geometry
    (append geometry
      (list
        (make block
          (center 0 0 0)
          (material si)
          (size
            defect_length
            (* 2 r)
            (if 3D h infinity)))))))

; Holes are made inside the cavity with a radius r2. Often, r2=0, and
    no holes are made
(if (not ref_run)
  (set! geometry
    (append geometry
      (geometric-object-duplicates
        (vector3 1 0 0)
        (/ (- defect_length 1) -2)
        (/ (- defect_length 1) 2)
        (make cylinder
          (center 0 0 0)
          (radius r2)
```

```
          (height (if 3D (+ h lbio lbio) infinity))
          (material (if biosensing bio air)))))))

(if biosensing
  (if (not ref_run)
    (set! geometry
      (append geometry
        (geometric-object-duplicates
          (vector3 1 0 0)
          (/ (- defect_length 1) -2)
          (/ (- defect_length 1) 2)
          (make cylinder
            (center 0 0 0)
            (radius (* r2 (+ bio_thickness -1) -1))
            (height (if 3D (+ h lbio lbio) infinity))
            (material water)))))))


; 4: adding silicon holes to cover the center row and defining
   incoupling and outcoupling waveguides. Top and bottom holes are
   covered, to make pml area. The upper waveguide has either one or
   two exits
(if (not ref_run)
  (if biosensing
    (if 3D
      (set! geometry
        (append geometry
          (list
            (make block ;horizontal si edge stripes
              (center 0 (/ sy 2) 0)
              (material bio)
              (size numx (* 2 pml_t) (+ h lbio lbio)))
            (make block
              (center 0 (/ sy -2) 0)
              (material bio)
              (size numx (* 2 pml_t) (+ h lbio lbio)))
            (make block ;lower waveguide
              (center (- (/ sx 2) (/ pc_wg_length 2)) (* wg_dist -1) 0)
              (material bio)
              (size
                pc_wg_length
                (* 2 r)
                (+ h lbio lbio)))
            (make block ;upper waveguide
              (center
                (if trans_exit
```

```
                0
                (* (- (/ sx 2) (/ pc_wg_length 2)) -1))
              wg_dist
              0)
            (material bio)
            (size
              (if trans_exit
                infinity
                pc_wg_length)
              (* 2 r)
              (+ h lbio lbio)))))))))

(if (not ref_run)
  (begin
    (set! geometry
      (append geometry
        (list
          (make block ;vertical air edge stripes
            (center (/ (+ pml_t wg_length numx) -2) 0 0)
            (material air)
            (size (+ pml_t wg_length) infinity infinity))
          (make block
            (center (/ (+ pml_t wg_length numx) 2) 0 0)
            (material air)
            (size (+ pml_t wg_length) infinity infinity))
          (make block
            (center 0 (/ sy 2) 0)
            (material si)
            (size numx (* 2 pml_t) (if 3D h infinity)))
          (make block
            (center 0 (/ sy -2) 0)
            (material si)
            (size numx (* 2 pml_t) (if 3D h infinity)))
          (make block ;strip waveguides
            (center (/ (+ pml_t wg_length numx) -2) wg_dist 0)
            (material si)
            (size
              (+ pml_t wg_length)
              wg_width
              (if 3D h infinity)))
          (make block
            (center (/ (+ pml_t wg_length numx) 2) (* wg_dist -1) 0)
            (material si)
            (size
              (+ pml_t wg_length)
              wg_width
```

```
            (if 3D h infinity)))
          (make block ;lower waveguide
            (center (- (/ sx 2) (/ pc_wg_length 2)) (* wg_dist -1) 0)
            (material si)
            (size
              pc_wg_length
              (* 2 r)
              (if 3D h infinity)))
          (make block ;upper waveguide
              (center (/ (+ pml_t wg_length numx) 2) wg_dist 0)
              (material si)
              (size
                (+ pml_t wg_length)
                wg_width
                (if 3D h infinity)))
          (make block
              (center
                (if trans_exit
                  0
                  (* (- (/ sx 2) (/ pc_wg_length 2)) -1))
                wg_dist
                0)
              (material si)
              (size
                (if trans_exit
                  infinity
                  pc_wg_length)
                (* 2 r)
                (if 3D h infinity)))))))


; 5: adding the silicon dioxide substrate if the structure is not an
    air-bridge. Water is added above the crystal if biosensing=true
    and bio_thickness=0
(if 3D
  (if bottom_oxide
    (set! geometry
      (append geometry
        (list
          (make block
            (center 0 0 (+ (/ sz -4) (/ h -4)))
            (material oxide)
            (size infinity infinity (- (/ sz 2) (/ h 2)))))))))

(if 3D
```

```
  (if biosensing
    (if (equal? bio_thickness 0)
      (set! geometry
        (append geometry
          (list
            (make block
              (center 0 0 (+ (/ sz 4) (/ h 4)))
              (material water)
              (size numx infinity (- (/ sz 2) (/ h 2)))))))))


; defining the resolution, PML layer and mirror symmetries
(set-param! resolution res); the default resolution is 10
(set! pml-layers (list (make pml (thickness pml_t))))

(if 3D
  (if (not bottom_oxide)
    (set! symmetries
      (list
        (make mirror-sym
          (direction Z))))))

; one of the two types of simulations is run. The TE polarization is
    studied.
(if resonance
  (begin
    ; defining the excitation current source
    (set! sources
      (list
                  (make source
          (src
            (make gaussian-src
              (frequency fcen)
              (fwidth dff)))
          (component Ey)
          (center 0 0)
          (size 0 (* 2 r) (if 3D h infinity)))))

    ; running the simulation
    (run-sources+ harminv_decay_until
      (at-beginning output-epsilon)
      (after-sources
        (harminv Ey (vector3 0) fcen dff))))
  (begin
    ; defining the excitation current source
    (set! sources
```

```
    (list
      (make source
        (src
          (make gaussian-src
            (frequency fcen)
            (fwidth dff)))
        (component Ey)
        (center (* source_pos_x -1) wg_dist 0)
        (size 0 wg_width (if 3D h infinity)))))

; defining the flux plane at the output waveguide for
    transmission plots, and at the input waveguide for reflection
    plots and so on
(let
  ((trans
    (add-flux fcen dff nfreq
      (make flux-region
        (center flux_pos_x wg_dist 0)
        (size 0 (* wg_width 2) (if 3D (* h 2) infinity)))))
  (refl
    (add-flux fcen dff nfreq
      (make flux-region
        (center (* (- source_pos_x 0.5) -1) wg_dist 0)
        (size 0 (* wg_width 2) (if 3D (* h 2) infinity)))))

  (fd
    (add-flux fcen dff nfreq
      (make flux-region
        (center flux_pos_x (* wg_dist -1) 0)
        (size 0 (* wg_width 2) (if 3D (* h 2) infinity)))))
  (bd
    (add-flux fcen dff nfreq
      (make flux-region
        (center (* (- source_pos_x 0.5) -1) (* wg_dist -1) 0)
        (size 0 (* wg_width 2) (if 3D (* h 2) infinity))))))

  ; running the simulation
  (if (not ref_run) (load-minus-flux "refl-flux" refl))
  (if ref_run
    (run-sources+
      (stop-when-fields-decayed 50 Ey (vector3 flux_pos_x wg_dist 0)
          decay_until)
      (at-beginning output-epsilon))
    (if movie
      (run-sources+
        (stop-when-fields-decayed 50 Ey (vector3 flux_pos_x (*
```

```
            wg_dist -1) 0) decay_until)
        (at-beginning output-epsilon)
        (to-appended "ey" (at-every video_interval output-efield-y)));(
            after-sources (harminv Ey (vector3 (* (- source_pos_x
            0.5) -1) 0) fcen dff))
      (run-sources+
        (stop-when-fields-decayed 50 Ey (vector3 flux_pos_x (*
            wg_dist -1) 0) decay_until)
        (at-beginning output-epsilon))))
  (if ref_run (save-flux "refl-flux" refl))

  ; print the accumulated fluxes in the output file
  (display-fluxes trans refl fd bd))))
```